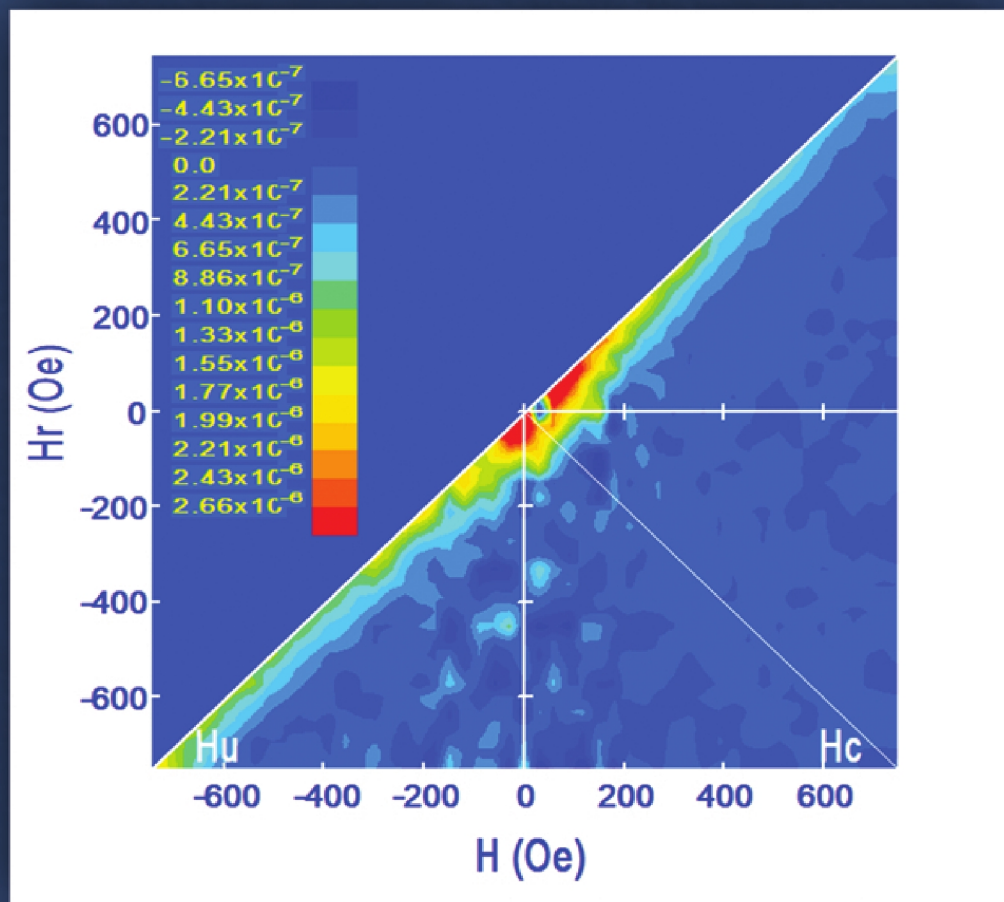


Advanced Ceramics Progress



Materials and Energy
Research Center



Iranian Ceramic Society

In The name of God

Advanced Ceramics Progress

DIRECTOR-IN-CHARGE

H. Omidvar

EDITOR-IN-CHIEF

M. R. Rahimipour

EXECUTIVE MANAGER

M. Razavi

EDITORIAL BOARD

- | | | | |
|-------|---|-------|--|
| A. R. | Aghaei, Materials and Energy Research Center | H. | Omidvar, Amirkabir University of Technology |
| P. | Alizadeh, Tarbiat Modares University | M. R. | Rahimipour, Materials and Energy Research Center |
| T. | Ebadzadeh, Materials and Energy Research Center | M. | Razavi, Materials and Energy Research Center |
| M. A. | Faghihi Sani, Sharif University of Technology | E. | Salahi, Materials and Energy Research Center |
| M. | Ghassemi Kakroudi, University of Tabriz | M. | Salehi, Isfahan University of Technology |
| A. R. | Khavandi, Iran University of Science and Technology | Ş. | Ţălu, Technical University of Cluj-Napoca |
| M. M. | Mohebi, Imam Khomeini University | | |

EDITORIAL ADVISORY BOARD

P. Feng, F.S. Torknik

ENGLISH LANGUAGE EDITOR

M. Sabzevari

TECHNICAL STAFF

E. Pouladi, V. Hajabdolali, R. Chaluei

DISCLAIMER

The publication of articles in *Advanced Ceramics Progress* does not imply that the editorial board, editorial advisory board, reviewers or the publisher accept, approve or endorse the data and conclusions of authors.

Advanced Ceramics Progress (ISSN 2423-7477) (e-ISSN 2423-7485)

Web Site: www.acerp.ir, E-mail: office@acerp.ir

Tel: +98 (0) 26 36280040-7 ext.: 382, Fax: +98 (0) 26 36201888

Tel: +98 (0) 21 88771626-7 ext.: 8931, Fax: +98 (0) 21 88773352

Materials and Energy Research Center (MERC); Iranian Ceramic Society (ICERS)

CONTENTS

Ali Shanaghi Ali Reza Souri Wrya Forghani	Comparative Study of Anodized Titanium Surfaces: The Effect of Low Voltage on the Morphology, Performance, and Corrosion Resistance of the Double Layer	1-7
Mohammad Reza Akbarpour Solmaz Moniri Javadhesari	Characterization of Flowability and Compaction Behavior of Biomedical Ti-Cu Intermetallic Alloy Synthesized by Mechanical Alloying Method	8-15
Leila Rezazadeh Susan Hasheminia Zahra Khakpour	The Effect of Temperature and Al as an Additive on the Synthesis, Structure, Densification, and Conductivity of Garnet-Type $\text{Li}_7\text{La}_3\text{Zr}_2\text{O}_{12}$	16-23
Sana Seifollahpour Afshin Ashofteh Amir Hossein Shahdadi Mahmoud Mosavi Mashhadi	Nanoindentation-Based Mechanical Properties Evaluation of Nano-Structure and Composite Plasma Spray Formed Ceramic Nozzles	24-35
Kaveh Kolahgar Azari Amir Hossein Sayadi Kelemi Ali Alizadeh Hamid Omidvar	Investigating the Phenomenon of Flutter as well as the Mechanical and Microstructural Properties of Layered Composite of Aluminum Sheet with An Epoxy Matrix Reinforced with Carbon Fibers	36-44
Kamran Heydaryan Mohammad Almasi Kashi	Characterization and magnetic properties of CoFe_2O_4 nanoparticles synthesized under gas atmosphere: Effect of ferrofluid concentration on hyperthermia properties	45-52



Materials and Energy Research Center

MERC

Contents lists available at [ACERP](#)

Advanced Ceramics Progress

Journal Homepage: www.acerp.ir

Advanced Ceramics Progress

Original Research Article

Comparative Study of Anodized Titanium Surfaces: The Effect of Low Voltage on the Morphology, Performance, and Corrosion Resistance of the Double Layer

Ali Shanaghi ^{a,*}, Ali Reza Souri ^{b,*}, Wrya Forghani ^c^a Associate Professor, Department of Materials Engineering, Faculty of Engineering, Malayer University, Malayer, Iran, P.O. Box 65719-95863^b Assistant Professor, Department of Materials Engineering, Faculty of Engineering, Malayer University, Malayer, Iran, P.O. Box 65719-95863^c MSc, Department of Materials Engineering, Faculty of Engineering, Malayer University, Malayer, Iran, P.O. Box 65719-95863* Corresponding Authors' Emails: a.shanaghi@malayeru.ac.ir (A. Shanaghi); arsouri@gmail.com (A. R. Souri)URL: https://www.acerp.ir/article_169260.html

ARTICLE INFO

A B S T R A C T

Article History:

Received 31 January 2023
Received in revised form 27 February 2023
Accepted 5 April 2023

Keywords:

Anodizing
Low Voltage
Ti Alloy
Simulated Body Fluid Solution
Corrosion Behavior
Double Layer

The anodizing process of titanium (Ti) implants and their alloys improves their corrosion resistance and life service by naturally increasing the thickness of the passive oxide layer formed on the surface. Among the parameters that affect the properties of the anodized layer, voltage is a significant one due to the kinetic and thermodynamic processes. In this paper, commercial pure titanium (cp-Ti) coupons with the dimensions of $20 \times 10 \times 1 \text{ mm}^3$ were used as the anode in 1 M sulfuric acid solution at different voltages of 3, 6, and 9 V, current intensity of 3 A, electrolyte temperature of 60 °C, and duration time of 30 s. The phase composition analysis, morphology, and corrosion behavior of the anodized Ti were examined by Grazing-Incidence X-Ray Diffraction (GIXRD), Field-Emission Scanning Electron Microscopy (FESEM), and electrochemical impedance, respectively, in Simulated Body Fluid (SBF) at 37 °C. The results confirmed the formation of titanium oxide coating with a hexagonal structure. A smoother surface was obtained upon increasing the voltage up to 6 V. However, the surface became rougher with further voltage increase up to 9 V. The highest charge transfer resistance (37354 and 58127 ohm.cm^{-2}) was achieved at 6 V after 1 and 24 hours of immersion in the SBF solution, representing 84 % and 2440 % increase, respectively, compared to the cp-Ti sample. The double layer helps prevent the formation of localized corrosion sites, such as pitting and crevice corrosion, which can be particularly damaging to Ti alloy as an implant in the human body. Although rising the voltage from 3 to 6 V resulted in a more hydrophobic surface (as shown by an increase in the contact angle from 63.8° to 74.1°), further voltage increase up to 9 V made the surface more hydrophilic than before.

<https://doi.org/10.30501/acp.2023.383589.1116>

1. INTRODUCTION

Affected by rapid improvement in the living standards and progress in the societies in general, human beings have been more exposed to social pressures imposed by the spread of different types of diseases limiting human

life expectancy. Microsurgery and use of biological materials like antibacterial agents and antibiotics are some of the most effective ways to preserve and extend human lives [1]. Despite its benefits, it can also be costly due to the financial burden it puts on the patient's insurance services [2]. Biological materials, however,

Please cite this article as: Shanaghi, A., Souri, A. R., Forghani, W., "Comparative Study of Anodized Titanium Surfaces: The Effect of Low Voltage on the Morphology, Performance, and Corrosion Resistance of the Double Layer", *Advanced Ceramics Progress*, Vol. 9, No. 2, (2023), 1-7. <https://doi.org/10.30501/acp.2023.383589.1116>

2423-7485/© 2023 The Author(s). Published by MERC.

This is an open access article under the CC BY license (<https://creativecommons.org/licenses/by/4.0/>).

can cause mechanical failure, infection, and reactions in relation to racial immunity. In this regard, there have been considerable research efforts to improve these materials in order to continue physiological processes and vital functions for survival [3]. One of the most popular metal materials for medical applications is titanium alloys. Ti-6Al-4V has been widely used in biomedical applications for a long time. However, it has been found to have potential toxic effects caused by the release of vanadium and aluminum ions [4]. This has encouraged the researchers to focus on commercial pure titanium (cp-Ti), the best biocompatible metallic material owing to its surface properties that spontaneously produce a neutral and stable oxide layer. Several of its characteristics such as low electron conductivity, stable thermodynamic state at the body pH values, and low tendency to take form in aqueous media make it an ideal choice for medical applications [4]. Additionally, its surface can be further enhanced through anodizing processes that results in the formation of a thicker, more corrosion-resistant layer. Therefore, titanium is a preferable choice for medical implants due to its better biocompatibility and strength [5-7].

Anodizing is one of the surface improvement processes that can lead to the formation of a thick oxide layer on a metal substrate. Aluminium, Titanium, Tantalum, Niobium, Vanadium, Hafnium, and Tungsten are known as the valve metals since they are quickly covered with a thin homogenous oxide layer when exposed to oxygen-rich environments [8-9]. This protective oxide layer helps slow down the reaction rate on the metal surface; therefore, these metals are widely used to protect metals from corrosion [9-10].

Despite extensive studies on the strength and biocompatibility of titanium implants, few studies have been conducted to compare the growth of the anodic oxide on the valve metal surfaces [11-12]. The thickness of the titanium oxide layer depends on the electrolyte solution, pH value, applied voltage, current density, and anodizing time. As a result, these factors can lead to the formation of thicker and porous oxide layers among which, voltage is more remarkable than the other environmental ones since the valence state of the cations within the passive film is highly dependent on the passive potential. This valence state can then affect the doping density, flat band potential and ultimately, corrosion protection [13]. Moreover, the composition and structure of the passive film will determine the corrosion protection, and different compounds and structures can cause different protective effects. In the anodizing process, different electrolytes, sulfuric acid [14-16], phosphoric acid [17-18], and oxalic acid [19-21] are used. In general, sulfuric acid is the most commonly used electrolyte solution due to its lower price and high rate of oxide layer formation [14-16].

Anil Kumar found that the anodic current density increased upon increasing the applied voltage and

temperature of the electrolyte, and the incremental change in the anodizing voltage leads to changes in the deposition rate of the oxide layer as well as the pore diameter [22], color of the oxide layers, slope between the applied current density, and anodization time. However, they did not report the relation between the porous properties of titanium oxide and voltage of the anodizing process. In this regard, we conducted a systematic study of the anodization conditions of cp-Ti substrate in 1 M sulfuric acid solution at different low voltages and then investigated the phase, structural and morphological properties as well as the corrosion behavior of the samples through electrochemical tests and electrochemical impedance in Simulated Body Fluid (SBF) at 37 °C.

2. MATERIALS AND METHODS

The commercial Ti foils (Ti, 99.33 %) with elemental analyses (Table 1) were annealed according to ASTM B265-10 and cut into 20×10 mm² pieces that were 2 mm thick. The pieces were then polished with sandpaper ranging in grit from 800 to 3,000 and alumina slurry solution of 0.5 μm in diameter. After polishing, the samples were degreased and ultrasonically rinsed for 10 min in acetone (99.5 %, Merck), ethanol (97 %, Merck), and deionized water. The cleaned Ti specimens were then electropolished in a mixture of hydrofluoric acid (HF, 40 %, Merck) and nitric acid (HNO₃, 65 %, Merck) (volume ratio = 1:8) for 90-120 s and rinsed with deionized water and dried in air. All chemicals were used as received without further purification.

The anodizing process [11,14-16] was then conducted in an electrochemical two electrode cell containing 200 ml 1 M sulfuric acid (H₂SO₄, 95-97 %, Merck) solution at 60 °C for 30 seconds with three different low voltages (3, 6, and 9 V) at the constant current of 3 A.

The phase, structure, and morphology of the coatings were determined using Grazing- Incidence X- Ray Diffraction (GIXRD; Philips PW- 1730 X- ray diffractometer; Cu Kα, λ = 0.154056 nm) and Field-Emission Scanning Electron Microscopy (FE-SEM; MIRA3 TESCAN). The thickness of the coatings was determined by the FE-SEM cross section. The water contact angles were measured on the contact angle goniometer (model 200-00-115, Ramé-Hart Instrument Co.), and the surface energy was calculated by the DROP image standard software (harmonic mode) and Owens–Wendt method [23-24].

The corrosion test was done in a the SBF solution containing 7.996 g of NaCl, 0.35 g of NaHCO₃, 0.224 g of KCl, 0.228 g of K₂HPO₄.3H₂O, 0.305 g of MgCl₂.6H₂O, 40 mL of 1 M HCl, 0.278 g of CaCl₂, 0.071 g of Na₂SO₄, and 6.057 g of (CH₂OH)₃CNH₂ at 37 °C while the pH was adjusted at 7.25 with 1 M HCl. Electrochemical Impedance Spectroscopy (EIS) and

potentiodynamic polarization tests were carried out on the electrochemical workstation (IviumSTAT, Netherlands). The corrosion characteristics were evaluated in a cell composed of the anodized sample as a working, Ag/AgCl as a reference, and platinum mesh as an auxiliary electrode in 250 ml SBF. The surface area was about 1 cm². The EIS was performed from 10⁻¹ to 10⁵ Hz by applying 10 mV as the amplitude and frequency of 20 mHz in the sweeping mode. To investigate the corrosion mechanism of the coatings, the impedance tests were done at 1 and 24 h, and the corroded surfaces of the anodized samples after 24 h were investigated by the FE-SEM image.

TABLE 1. The Elemental analysis of cp-Ti determined by optical emission spectrometer

Element	Ti	C	N	H	O	Fe
(wt. %)	99.33	0.08	0.03	0.01	0.25	0.30

3. RESULTS AND DISCUSSION

The anodizing process improves the microstructural properties, shape, and corrosion resistance of titanium oxide by thickening the natural titanium oxide layer on its surface. The anodizing voltage of the process has a huge impact on the oxidation reaction in terms of speed, shape, and microstructure of titanium oxide. In this paper, the anodizing process was carried out using 3, 6, and 9 volts on the cp-Ti substrate.

Figure 1 shows the GIXRD curve of the anodized sample. According to the standard card Titanium oxide, the main peaks at different angles from the anatase TiO₂ (JCPDS 01-072-1807) are 39.39°, 37.93°, and 34.95° related to the crystal plates (-1-12), (004), and (110), respectively, and the 53.01°, 63°, 70.7°, and 76.2° related to the (222), (213), (322), and (231), respectively, appeared from the Ti substrate (JCPDS 21-1272). These peaks are indicative of the hexagonal crystal structure of titanium oxide [6,11].

Upon increasing the voltage from 3 volts to 9 volts, the FE-SEM images of the anodized titanium samples at 3, 6, and 9 (Figure 2) show an improvement in the uniformity and homogeneity of the anodized cp-Ti. However, according to the literature [9,11,22], increasing the anodizing voltage at a high value would increase the deposition rate of the oxide layer or thickness as well as the pore diameter.

The surface wettability, which is related to the surface energy of a body, is one of the surface characteristics that affects its biological capabilities. Generally, hydrophilic surfaces improve the adhesion, proliferation, cell division, and bone mineralization [11,22]. The results of water contact angle measurements are summarized in Table 2. as observed, the lower the water contact angle, the higher the wettability.

According to the literature, hydrophilicity increased by increasing the surface roughness; however, the surface could become either superhydrophilic or superhydrophobic when it was very smooth. The obtained

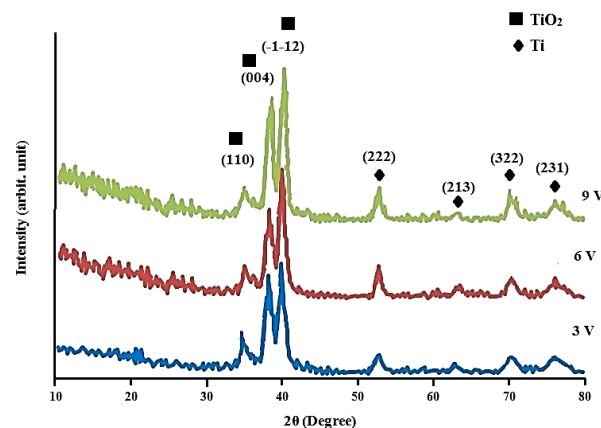
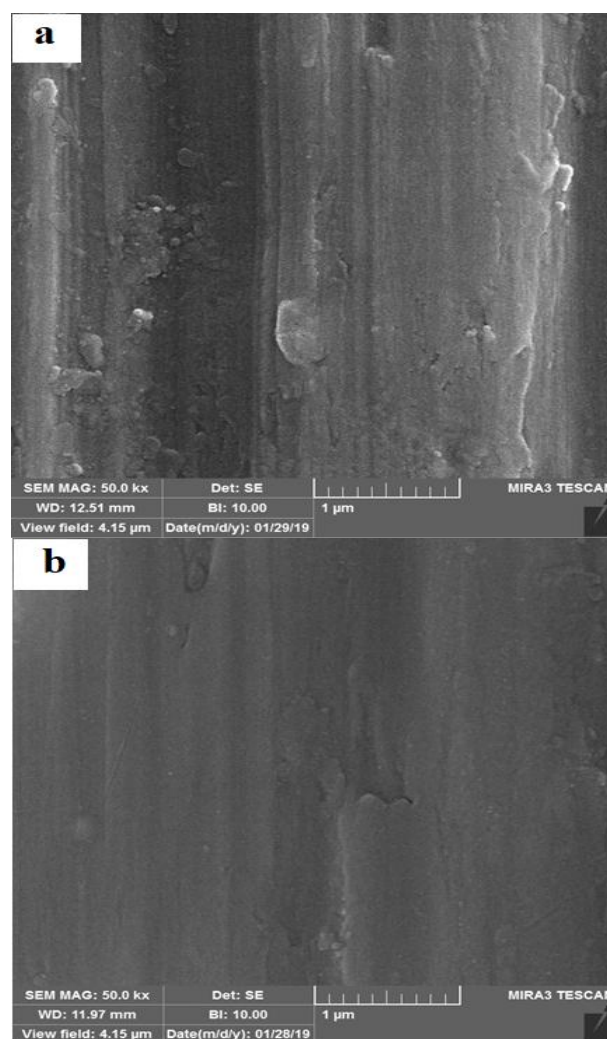


Figure 1. GIXRD curve of anodized titanium sample at low voltages such as 3, 6, and 9 volts at an incidence angle 1°



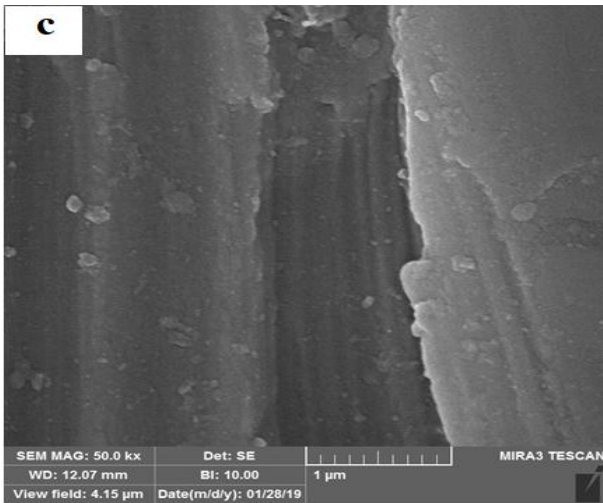


Figure 2. FE-SEM image of anodized titanium at different low voltages, a) 3 volts, b) 6 volts, and c) 9 volts

TABLE 2. Water contact angle of cp- Ti substrate and anodized cp-Ti at low voltages 3, 6, and 9 V

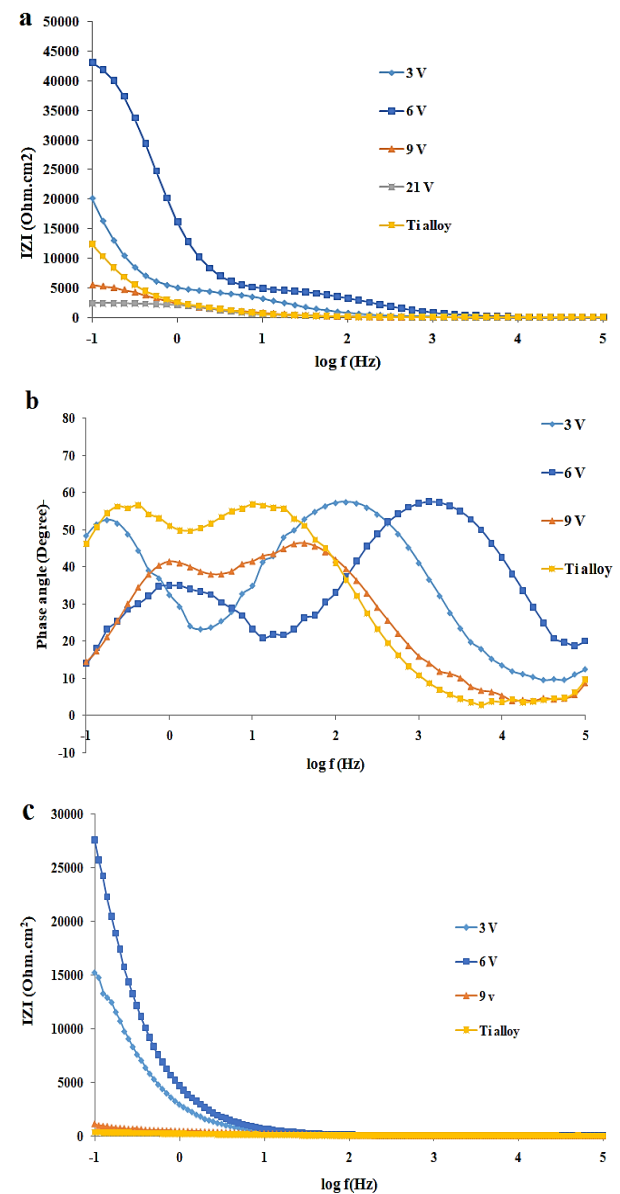
Specimen	Contact angle (Degree)
cp-Ti	103.7
Anodized cp-Ti at 3 V	63.8
Anodized cp-Ti at 6 V	74.1
Anodized cp-Ti at 9 V	57.2

results showed that anodizing the titanium substrate would increase its hydrophilicity by creating titanium oxide on the surface and increasing its surface roughness (confirmed by FE-SEM images in Figure 2). Increasing the voltage from 3 to 6 volts increased the contact angle from 63.8° to 74.1°, thus making the surface more hydrophobic. However, increasing the voltage from 6 to 9 volts increased the hydrophilicity of the surface, and water droplets spread rapidly on the surface under the capillary effect [11,25].

According to the bode and bode-phase plots, applying the anodizing voltage of 6 V resulted in a more capacitive behavior at higher frequencies than that at other voltages, and the diffusion of water from surface defects of anodized cp-Ti sample at 3 and 9 V caused resistance behavior at a high frequency. In addition, the presence of two-time constants in the bode-phase curve is indicative of the presence of oxide layers and obstacles in the path of electrons between the SBF solution and titanium substrate as well as the formation of a double layer at their interface. However, upon increasing the immersion time (Figure 3a), As a result of the penetration of water ions into the anodizing oxide layer and presence of soluble ions on the layer, especially for 6 V sample, a decrease in the corrosion resistance was observed with a reduction in the phase angle at high frequencies. The existence of a wide time constant for 3 and 6 V confirms the formation of homogeneous and uniform corrosion

products on the anodized cp-Ti sample at 24 h in the SBF solution compared to other samples (Figure 3c). This corrosion behavior at low voltages can be attributed to the formation of the corrosion products on the anodized surface, compared to the non-anodized sample [6-7], as well as the homogeneity, uniformity, and defect-free corrosion of the products on the surface of the anodized samples at low voltages of 3 and 6 V, all more than those at 9 V.

In order to accurately evaluate the corrosion behavior, electrochemical systems were simulated as an electrical circuit containing a resistor and a capacitor. This circuit is related to the capacity of the dual layer which has two plates with an arrangement of opposite charges, and the resistance of this layer is referred to as the dual layer resistance or charge transfer resistance. Double layer



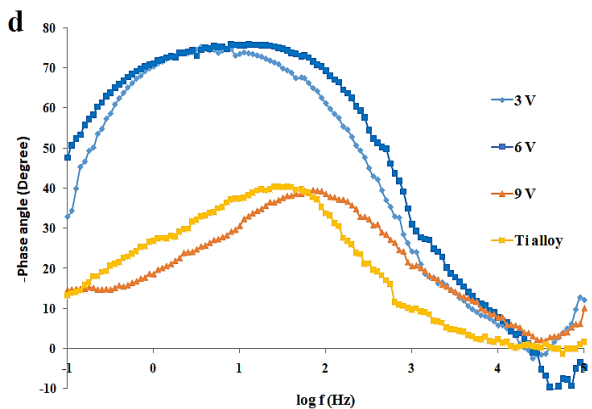


Figure 3. Bode and bode-phase plots of cp-Ti alloy, and anodized cp-Ti at low voltage, 3 V, 6 V, and 9 V, at two immersion times a-b) 1 h and c-d) 24 h

refers to the electrochemical structure that develops at the interface between a metal surface and an electrolyte solution. The double layer consists of two layers of charge, known as the Helmholtz and diffuse layers. The Helmholtz layer is a compact layer of adsorbed ions and water molecules that are directly attached to the metal surface while the diffuse layer is a less ordered layer of ions that surround the Helmholtz layer. The performance of the double layer on the corrosion behavior of anodized titanium is an important factor to consider. The double layer formed at the interface between the anodized titanium surface and electrolyte plays a crucial role in the corrosion behavior of the material. The protective oxide layer formed during anodization acts as a barrier to limit the access of the corrosive species to the underlying metal surface while the double layer helps repel the charged species that could cause corrosion [6-7]. The proposed equivalent circuit is demonstrated in Figure 4 for the cp-Ti and anodized cp-Ti at low voltages of 3, 6, and 9 volts, and the results are shown in Table 3. R_{ct} is associated with the charge transfer resistance of the dual layer, and CPE_{dl} to the dual layer capacitance.

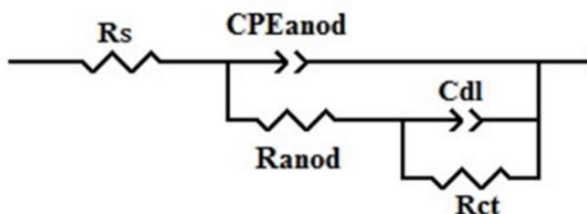


Figure 4. Equivalent circuit of cp-Ti substrate and anodized cp-Ti specimens at low voltages of 3, 6, and 9 volts

The charge transfer resistance (R_{ct} ; $\Omega \cdot \text{cm}^2$) and n of the cp-Ti substrate and anodized cp-Ti specimen at 3, 6, and 9 volts after an hour in the SBF solution (Table 3) show

the higher resistance along with the enhanced homogeneity and uniformity of the coating surface while increasing n for the anodized cp-Ti specimens at 6 V, compared to the other voltages. Generally, anodizing causes an increase in the heterogeneity and roughness, which was clear for the anodized samples at 3 and 9 V, thus leading to a decrease in the corrosion resistance due to the increased surface imperfections and intensity of the local corrosion reactions, compared to 6 V. Results of Table 3 denoted that prolonging the immersion time from 1 to 24 hours intensifies the corrosion reactions and enhances the charge transfer resistance between the SBF solution and sample surface. In fact, the anodization process results in the formation of a porous oxide layer on the titanium surface, which increases the surface area and facilitates the formation of a more robust double layer. The thickness and properties of the oxide layer can be controlled by adjusting the anodization parameters such as the voltage, current density, and electrolyte composition. Studies have shown that compared to the non-anodized titanium surface, the anodized titanium surface with a well-formed double layer exhibited significantly improved corrosion resistance.

TABLE 3. Parameters obtained from the equivalent circuit of cp-Ti substrate and anodized cp-Ti specimens at low voltages of 3, 6, and 9 volts

Time period (h)	Sample	CPE_{dl} ($\mu\text{F} \cdot \text{cm}^{-2} \cdot \text{s}^{-n}$)	R_{ct} ($\Omega \cdot \text{cm}^2$)	n_{dl}	Chi-squared
1	Ti alloy	59.91	20235	0	0.00189
	TiA3	71.17	36179	0	0.00335
	TiA6	9.839	37354	0	0.01135
	TiA9	69.28	4127	0	0.00142
24	Ti alloy	2523.27	2287	0.65	0.00195
	TiA3	24.79	20995	0.86	0.00454
	TiA6	34.62	58127	0.81	0.00668
	TiA9	1586.42	6391	0.85	0.00546

In summary, the significant increase in the surface heterogeneity (n) of the cp-Ti sample and anodized cp-Ti samples at low voltage of 6 V, compared to 3 and 9 V, after 24 hours that was confirmed by FE-SEM images (Figure 5) obtained from the EIS study at 24 hours in the SBF solution. The double layer helps prevent the formation of localized corrosion sites such as pitting and crevice corrosion, which can be particularly damaging to titanium. Overall, the performance of the double layer and its effect on the corrosion behavior of the anodized titanium is of significance while maintaining the material's corrosion resistance properties. The anodization process can be used to form a protective oxide layer on the titanium surface, which enhances the double layer and improves the corrosion resistance of the material [6-7,9-10].

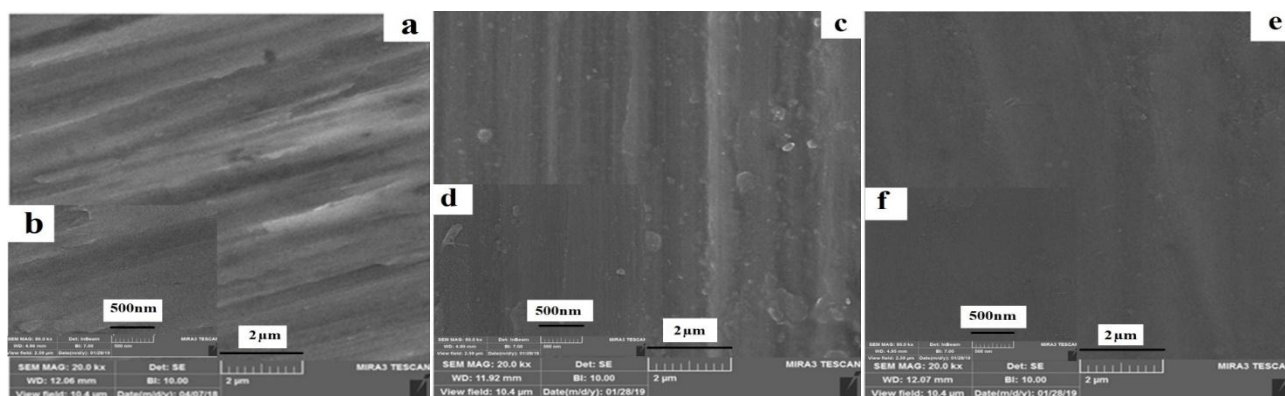


Figure 5. FE-SEM images of anodized cp-Ti at low voltage, a-b) 3 V, c-d) 6 V, and e-f) 9 V after 24 h of immersion in SBF solution

4. CONCLUSION

The studies on the effect of low anodizing voltage on the corrosion behavior of cp-Ti specimens revealed that 6 volts could be an optimal voltage for titanium oxide formation with hexagonal structure that also ensured higher corrosion resistance than that of other anodized samples at 3 and 9 volts. Upon further increasing the voltage above 6 volts, both surface imperfections and roughness were enhanced that led to the intensity of local reactions due to the penetration of water and corrosive ions, thus resulting in the reduced corrosion resistance of the anodized sample at 9 V. Of note, the double layer prevented the formation of localized corrosion sites, such as pitting and crevice corrosion, which can be particularly damaging to titanium alloy as an implant in the human body. Further, increasing the voltage from 3 to 6 V increased the contact angle from 63.8° to 74.1°, indicating more hydrophobicity. However, rising voltage from 6 to 9 V caused an increase in the hydrophilicity properties.

ACKNOWLEDGEMENTS

The work was financially supported by Malayer University Research Grant No. 1400.

REFERENCES

1. Arsiwala, A., Desai, P., Patravale, V., "Recent advances in micro/nanoscale biomedical implants", *Journal of Controlled Release*, Vol. 189, (2014), 25-45. <https://doi.org/10.1016/j.jconrel.2014.06.021>
2. Bebell, L. M., Muiru, A. N., "Antibiotic Use and Emerging Resistance: how can resource-limited countries turn the tide?", *Global Heart*, Vol. 9, No. 3, (2014), 347-358. <https://doi.org/10.1016/j.gheart.2014.08.009>
3. Park, J., Lakes, R. S., *Biomaterials: An Introduction*, 3rd Ed., Springer Science & Business Media, (2007). <https://books.google.com/books/about/Biomaterials.html?id=bb6>

8wb0R_EAC

4. Elias, C. N., Lima, J. H. C., Valiev, R., Meyers, M. A., "Biomedical applications of titanium and its alloys", *Journal of the Minerals, Metals & Materials Society*, Vol. 60, No. 3, (2008), 46-49. <https://doi.org/10.1007/S11837-008-0031-1>
5. Gotman, I., Gutmanas, E. Y., "Titanium nitride-based coatings on implantable medical devices", *Advanced Biomaterials and Devices in Medicine*, Vol. 1, No. 1, (2014), 53-73. http://abiodem.com/download/files/abiodem_2014_no1_p53_gotman.pdf
6. Shanaghi, A., Mehrjou, B., Ahmadian, Z., Souri, A. R., Chu, P. K., "Enhanced corrosion resistance, antibacterial properties, and biocompatibility by hierarchical hydroxyapatite/ciprofloxacin-calcium phosphate coating on nitrided NiTi alloy", *Materials Science and Engineering: C*, Vol. 118, (2021), 111524. <https://doi.org/10.1016/j.msec.2020.111524>
7. Mehrjou, B., Dehghan-Baniani, D., Shi, M., Shanaghi, A., Wang, G., Liu, L., Qasim, A. M., Chu, P. K., "Nanopatterned silk-coated AZ31 magnesium alloy with enhanced antibacterial and corrosion properties", *Materials Science and Engineering: C*, Vol. 116, (2020), 111173. <https://doi.org/10.1016/j.msec.2020.111173>
8. Schultze, J. W., Lohrengel, M. M., "Stability, reactivity and breakdown of passive films. Problems of recent and future research", *Electrochimica Acta*, Vol. 45, No. 15-16, (2000), 2499-2513. [https://doi.org/10.1016/S0013-4686\(00\)00347-9](https://doi.org/10.1016/S0013-4686(00)00347-9)
9. Xiang, G. X., Li, S. Y., Song, H., Nan, Y. G., "Fabrication of modifier-free superhydrophobic surfaces with anti-icing and self-cleaning properties on Ti substrate by anodization method", *Microelectronic Engineering*, Vol. 233, (2020), 111430. <https://doi.org/10.1016/j.mee.2020.111430>
10. Kumar, G., Narayan, B., "Osseointegrated titanium implants: Requirements for ensuring a long-lasting, direct bone-to-implant anchorage in man", In Banaszkiwicz, P., Kader, D. (eds.), *Classic Papers in Orthopaedics*, London, Springer, (2014), 507-509. https://doi.org/10.1007/978-1-4471-5451-8_133
11. Masahashi, N., Mori, Y., Tanaka, H., Kogure, A., Inoue, H., Ohmura, K., Kodama, Y., Nishijima, M., Itoi, E., Hanada, S., "Bioactive TiNbSn alloy prepared by anodization in sulfuric acid electrolytes", *Materials Science and Engineering: C*, Vol. 98 (2019), 753-763. <https://doi.org/10.1016/j.msec.2019.01.033>
12. Beranek, R., Hildebrand, H., Schmuki, P., "Self-Organized Porous Titanium Oxide Prepared in H₂SO₄/HF Electrolytes", *Electrochemical and solid-state letters*, Vol. 6, No. 3, (2003), B12. <https://doi.org/10.1149/1.1545192>
13. Long, Y., Li, D. G., Chen, D. R., "Influence of Square Wave Anodization on the Electronic Properties and Structures of the Passive Films on Ti in Sulfuric Acid Solution", *Applied Surface Science*, Vol. 425, (2017), 83-94. <https://doi.org/10.1016/j.apsusc.2017.06.319>

14. Mohitfar, S. H., Mahdavi, S., Etminanfar, M., Khalil-Allafi, J., "Characteristics and tribological behavior of the hard anodized 6061-T6 Al alloy", *Journal of Alloys and Compounds*, Vol. 842, (2020), 155988. <https://doi.org/10.1016/j.jallcom.2020.155988>
15. Cheng, T. C., Chou, C. C., "The electrical and mechanical properties of porous anodic 6061-T6 aluminum alloy oxide film", *Journal of Nanomaterials*, Vol. 2015, (2015), 371405. <https://doi.org/10.1155/2015/371405>
16. Shih, T. S., Wei, P. S., Huang, Y. S., "Optical properties of anodic aluminum oxide films on Al1050 alloys", *Surface and Coatings Technology*, Vol. 202, No. 14, (2008), 3298-3305. <https://doi.org/10.1016/j.surfcoat.2007.12.002>
17. Masuda, H., Yada, K., Osaka, A., "Self-ordering of cell configuration of anodic porous alumina with large-size pores in phosphoric acid solution", *Japanese Journal of Applied Physics*, Vol. 37, No. 11A, (1998), L1340. <https://doi.org/10.1143/JJAP.37.L1340>
18. Zhang, J., Kielbasa, J. E., Carroll, D. L., "Controllable fabrication of porous alumina templates for nanostructures synthesis", *Materials Chemistry and Physics*, Vol. 122, No. 1, (2010), 295-300. <https://doi.org/10.1143/JJAP.37.L1340>
19. Wang, J., Wang, C. W., Li, Y., Liu, W. M., "Optical constants of anodic aluminum oxide films formed in oxalic acid solution", *Thin Solid Films*, Vol. 516, No. 21, (2008), 7689-7694. <https://doi.org/10.1016/j.tsf.2008.03.023>
20. Ghaforyan, H., Ebrahimzadeh, M., "Self-organized formation of hexagonal pore arrays in anodic alumina fabrication", *Journal of Materials Science and Engineering. B*, Vol. 1, No. 1B, (2011), 82-85. https://www.researchgate.net/profile/Hossein-Ghaforyan/publication/267773291_Self-Organized_Formation_of_Hexagonal_Pore_Arrays_in_Anodic_Alumina_Fabrication/links/56fa4b0508ae38d710a38580/Self-Organized-Formation-of-Hexagonal-Pore-Arrays-in-Anodic-Alumina-Fabrication.pdf
21. Chung, C. K., Liu, T. Y., Chang, W. T., "Effect of oxalic acid concentration on the formation of anodic aluminum oxide using pulse anodization at room temperature", *Microsystem Technologies*, Vol. 16, No. 8-9, (2010), 1451-1456. <https://doi.org/10.1007/s00542-009-0944-9>
22. Kumar, A., "Anodization of Titanium Alloy (Grade 5) to Obtain Nanoporous Surface Using Sulfuric Acid Electrolyte", *IETE Journal of Research*, Vol. 68, No. 5, (2020), 3855-3861. <https://doi.org/10.1080/03772063.2020.1780958>
23. Mehrjou, B.; Mo, S.; Dehghan-Baniani, D.; Wang, G.; Qasim, A. M., Chu, P. K., "Antibacterial and Cytocompatible Nanoengineered Silk-Based Materials for Orthopedic Implants and Tissue Engineering", *ACS Applied Materials & Interfaces*, Vol. 11, No. 35, (2019), 31605-31614. <https://doi.org/10.1021/acsami.9b09066>
24. Owens, D. K.; Wendt, R. C., "Estimation of the Surface Free Energy of Polymers", *Journal of Applied Polymer Science*, Vol. 13, No. 8, (1969), 1741-1747. <http://doi.org/10.1002/app.1969.070130815>
25. Zhou, X., Wu, F., Ouyang, C., "Electroless Ni-P alloys on nanoporous ATO surface of Ti substrate", *Journal of Materials Science*, Vol. 53, No. 4, (2018), 2812-2829. <https://doi.org/10.1007/s10853-017-1686-1>



Materials and Energy Research Center
MERC

Contents lists available at [ACERP](#)

Advanced Ceramics Progress

Journal Homepage: www.acerp.ir



Original Research Article

Characterization of Flowability and Compaction Behavior of Biomedical Ti-Cu Intermetallic Alloy Synthesized by Mechanical Alloying Method

Mohammad Reza Akbarpour ^{a,*}, Solmaz Moniri Javadhesari ^b

^a Professor, Department of Materials Engineering, Faculty of Engineering, University of Maragheh, Maragheh, P.O. Box 83111-55181, Iran

^b Assistant Professor, Department of Biology, Faculty of Basic Sciences, Azarbaijan Shahid Madani University, Tabriz, Iran

* Corresponding Author Email: akbarpour@maragheh.ac.ir (M. R. Akbarpour)

URL: https://www.acerp.ir/article_169262.html

ARTICLE INFO

Article History:

Received 25 February 2023
Received in revised form 27 March 2023
Accepted 5 April 2023

Keywords:

Mechanical Alloying
Flowability
Compressibility
Ti-Cu Alloy

ABSTRACT

This study investigated the flowability and compactability of the milled Ti-Cu alloys as a new version of biomedical alloys used for fabrication via Additive Manufacturing. In this study, Ti-50 at. % Cu powder was first milled for different durations, and the morphology, microhardness, size, flowability, and compactability of the powder were assessed. The results indicated that while flowability increased with prolonged milling time, compressibility decreased owing to a decrease in the plastic deformation capacity. The highest flowability level was obtained when hard TiCu phase was synthesized after 30 hours of milling. Different linear and nonlinear compaction equations were used to investigate the densification response of TiCu powder in a rigid mold during uniaxial compression. Cooper-Eaton nonlinear equation was found to be the best fit compared to the linear equation. The contribution of particle rearrangement to the densification behavior was high, and it increased upon increasing the applied pressure. At pressures below 1200 MPa, the contribution of plastic deformation to the powder densification was negligible.



<https://doi.org/10.30501/acp.2023.387236.1118>

1. INTRODUCTION

Commercially pure titanium is widely used in several dental products because of its excellent biocompatibility, corrosion resistance, and lightweight properties. However, pure Ti has some drawbacks in structural and biomedical applications such as its poor tribological and antibacterial properties, to name a few [1]. It has been reported that in dental prostheses, there is significant wear of the cast commercially pure (CP) titanium. Bacteria can also grow on Ti when bacterial infection occurs [2]. One way to solve these problems is to alloy titanium with other elements such as Cu. Alloying Ti and

Cu can improve the mechanical properties required for dental applications [3]. C. Ohkubo et al. investigated the effect of alloying elements, such as Cu, on the wear resistance of Ti. They demonstrated that addition of Cu (5 wt. %) introduced Ti/Ti₂Cu eutectoid and improved the wear resistance [4]. The tribological behavior of Ti-Cu intermetallic alloys produced by Powder Metallurgy (PM) method was studied [5]. Intermetallic Ti-Cu alloys are characterized by higher wear resistance to a tungsten carbide (WC) counterface and lower friction coefficients than commercially pure titanium, and their tribological properties can be significantly enhanced upon increasing the milling time owing to the grain

Please cite this article as: Akbarpour, M. R., Moniri Javadhesari, S., "Characterization of Flowability and Compaction Behavior of Biomedical Ti-Cu Intermetallic Alloy Synthesized by Mechanical Alloying Method", *Advanced Ceramics Progress*, Vol. 9, No. 2, (2023), 8-15. <https://doi.org/10.30501/acp.2023.387236.1118>

2423-7485/© 2023 The Author(s). Published by MERC.

This is an open access article under the CC BY license (<https://creativecommons.org/licenses/by/4.0/>).



refinement and increase in the Ti_2Cu_3 content. Much research has been done so far to evaluate the antibacterial and biocompatibility of TiCu alloys [6-9]. The properties of this alloy depend on the Cu content and formed intermetallic phases. Based on the conducted research, the superior antibacterial activity and biocompatibility of the Ti-Cu alloy make it feasible to use it as an implant material with minimal bacterial infection. It is also possible to obtain antimicrobial properties in the Ti-Cu alloys by adding copper elements. The antimicrobial properties of copper make it effective in killing bacteria quickly when released into the body. Bacteria cells produce copper toxin due to the presence of Cu (I) ions that can damage cell membranes and kill bacteria.

PM [5,7], casting [1], and Selective Laser Melting (SLM) [10,11] methods have recently been widely used to produce bulk Ti-Cu alloys. The properties of the Ti-Cu alloy parts processed with PM and SLM are strongly influenced by those of the powder. Mechanical alloying with a high-energy ball mill is a manufacturing process for nanocrystalline Ti-Cu powder that has been referred to many times in the literature [12,13]. More details of the microstructural and morphological changes in Ti-Cu powder during mechanical milling can be found in previous studies [13]. As the milling time has been shown to affect the powder properties, varying process conditions such as milling time can affect the flowability and compressibility of the powder used to manufacture Ti-Cu alloy. In the literature, no studies have been conducted on the effects of Ti-Cu alloy milling time/powder features on its flowability and compactibility, which play a key role in powder densification. Therefore, in the present work, Ti-Cu powder was mechanically alloyed for different times, and its morphology, hardness, size, flowability, and compaction behavior were studied for use in processing the Ti-Cu parts.

2. MATERIALS AND METHODS

Table 1 lists the raw materials and their characteristics. A mixture of Ti-50 at. % Cu powder was ball milled in a planetary ball mill (Retsch 400MA) for different times. The milling conditions and phase transformations that occur during milling have been previously reported in several studies [13].

TABLE 1. The used raw materials and their characteristics

Material	Average Particle Size (D_{50}) (μm)	Purity (%)	Manufacturer
Ti powder	45.9	99.5	Merck, Germany
Cu powder	12.5	99.7	Merck, Germany

To investigate the microstructure of the milled powder, Scanning Electron Microscopes (SEMs, Philips XL30) equipped with EDS and Transmission Electron Microscopes (TEMs, FEG Philips CM200) with Cu $K\alpha$ radiation ($\lambda=0.154$ nm) and a 0.02 degree/sec scan rate were used. As observed in the X-ray diffraction (XRD) patterns, the crystallite size and microstrain of the specimens were calculated using the Williamson-Hall method. Apparent Density (AD) and Tap Density (TD) of the powders were measured using the standard cup and funnel methods (ISO 3923). The powders milled for 1, 5, 10, 20, 30, and 40 hours were each compressed at 400, 600, 800, 1000, 1200, and 1400 MPa, respectively, with zinc stearate acting as a die lubricant. A density measurement was performed using Archimedes' law on the green samples. Each sample was measured three times, and their mean values were reported to ensure accuracy. As part of the flowability testing, an open-base Angle of Response (AOR) method was used to measure flowability. Each AOR test utilized a funnel to pour powder onto a large horizontal plate until a cone-shaped pile of powder formed, grew to a sufficient height, and no more powder accumulated. A digital camera was used to image the pile, and the angle value was measured by image analysis.

3. RESULTS AND DISCUSSION

3.1. Changes in the Structure and Morphology

The Ti-Cu powder was mechanically milled for different times using high-energy ball milling. At the beginning of milling, only severe plastic deformation occurred under the steel ball impact. Figures 1a and 1b demonstrate the flakes of Ti and Cu powder mixture milled for five hours. As the milling progressed, the strong impact of the steel ball made the particles of the powder mixture plastically deformed that led to the formation of a cold weld, revealing a prominent lamellar structure. With further milling, the distance between the lamellae decreased. As shown in Figures 1c and 1d, no lamellar structures can be observed after 30 hours of milling. At this stage, the microstructure of the powder was uniform. Our previous work described the morphological and microstructural changes in the Ti-Cu powder during milling. The average particle size after different milling times was measured using SEM micrographs, the values of which are listed in Table 2. The change in the Ti-Cu powder particle size with milling time showed an identical tendency to that of metal powders in general. During the first hours of milling, when cold welding is the dominant mechanism, the average particle size increases. When the milling is prolonged, work hardening results in the fracture of milled powders and the reduction of the particle size. After milling for a certain length of time, steady-state

equilibrium is obtained when a balance is achieved between the rate of welding, which tends to increase the

average particle size and rate of fracturing, thus leading to a decrease in the average particle size.

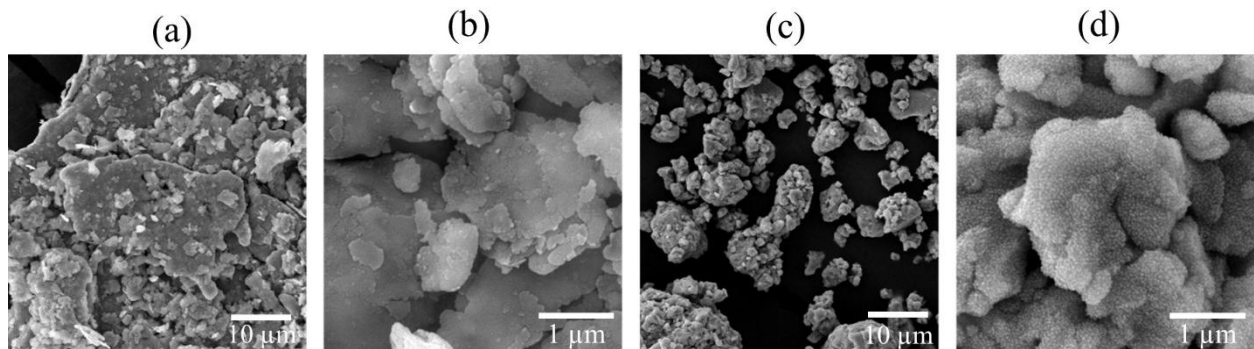


Figure 1. SEM micrographs illustrating the morphology of Ti-50 at. % Cu powder alloyed for 5 h (a, b) and 30 h (c, d)

TABLE 2. Features of the powder milled for different times

	Milling Time, h					
	1	5	10	20	30	40
Average Particle Size, μm	15.3	23.4	37.8	28.2	25.9	24.0
Grain Size, nm	98	35	29	17	7	6
Powder Morphology	Flake	Flake	Flake	Small Flake/Equiaxed	Equiaxed	Equiaxed
Phases	Ti, Cu	Ti, Cu	Ti, Cu	Ti, Cu	TiCu	TiCu

The Ti-Cu intermetallic powder was synthesized by milling Ti-Cu powder mixtures for 30 h. Table 2 summarizes the phases and crystallite sizes obtained from the XRD results of the powders milled for different times. The powder flow and compaction behaviour were explained based on these data.

Figure 2 depicts the SEM image of the powder particles mechanically alloyed for an hour as well as the maps of Ti and Cu distributions on the surfaces of the particles. As shown in this figure, Ti and Cu are not evenly distributed on the powder particles. Some regions of the microstructure were rich in Ti while others were rich in Cu (Figures 2a, 2b, and 2c).

Based on the EDS analysis (Figure 2d), sharp peaks are associated with major Ti while the faint ones are associated with minor Cu. Work hardening and fracturing of the powder gradually distributes the alloying elements into the powder volume as the MA period increases. Figure 3 shows the elemental maps of the distribution of Ti and Cu in the SEM image of the powder particles after 30 hours of milling. This figure also confirms that the alloying elements are evenly dispersed in the powder (Figures 3b and 3c). The EDS analysis (Figure 3d) reveals the approximately equal mol % presence of Ti and Cu in the particles, confirming their uniform dispersion at the atomic level.

3.2. Apparent and Tap Densities and Flowability

As shown in Figure 4a, the milling time affects the

apparent and tap densities of Ti-50 at. % Cu powder. As the milling time increased, the apparent and tap densities decreased and then increased. Hausner Ratio (HR) represents the relationship between the powder tap and apparent densities. It also indicates the flow potential of the powder. The higher the HR value, the lower the flowability of the powder at the beginning of the compaction. The HR value greater than 1.25 is indicative of the poor powder flowability.

The relationship between the HR and milling time for the Ti-Cu powder is shown in Figure 4b. The HR variation with the milling time depicted three distinct zones, i.e., 1-10, 10-30, and more than 30 h. Milling up to 10 hours results in a high HR due to the flake shape of the powders. During the first few hours of milling, the powders undergo plastic deformation and cold-welding, and they take a layered shape with poor flowability. Milling the powder for more than 10 hours induces work hardening and fracture in addition to plastic deformation. This in turn reduced the relative size of the powder and increased their sphericity. A milling process lasting more than 30 hours has little effect on the particle size and morphology of the powder and thus on the HR of the product. As shown in Figure 5, the AOR varied with the milling time. As the AOR increased, there was a stronger force between the particles, which reduced the flowability of the powder. AOR increased when the powder was mechanically milled for up to 10 hours. This increase was associated with the flake morphology of the

powder as well as the increase in the flake size. Based on the figure, it is evident that milling for longer than 10 minutes reduced the AOR, and milling for 30 minutes yielded the lowest AOR, indicating the highest

flowability. This is related to the changes in the powder morphology from flaky to equiaxial, which occur during milling.

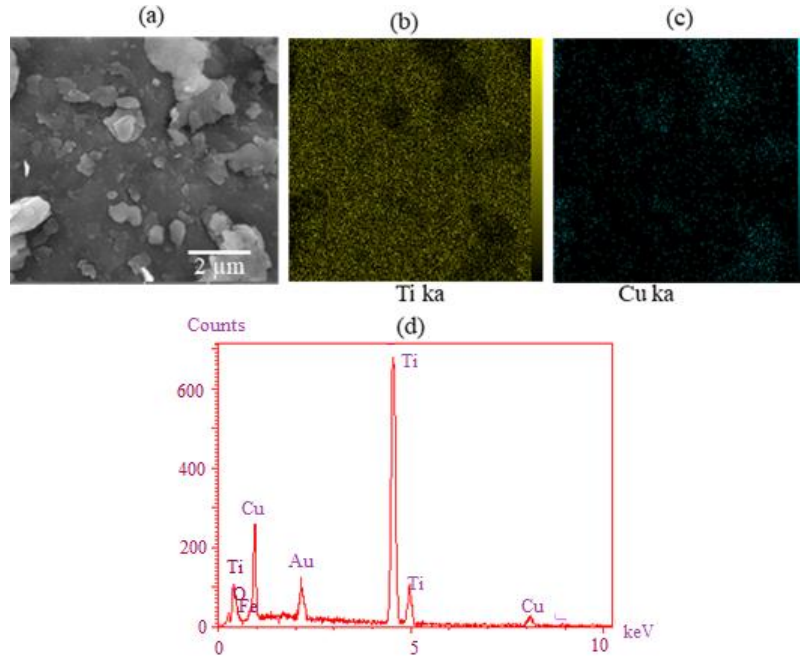


Figure 2. (a) SEM micrograph of a particle surface, (b) Ti distribution, (c) Cu distribution, and (d) EDS analysis of the 1 h mechanically alloyed Ti-Cu powder

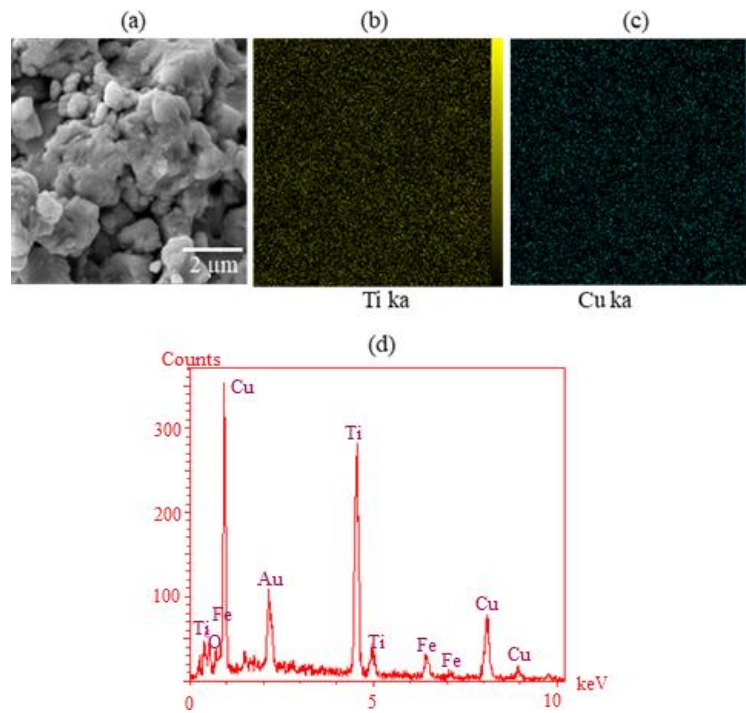


Figure 3. (a) SEM micrograph of a particle surface; (b) Ti distribution; (c) Cu distribution; and (d) EDS analysis of the 30 h mechanically alloyed Ti-Cu powder

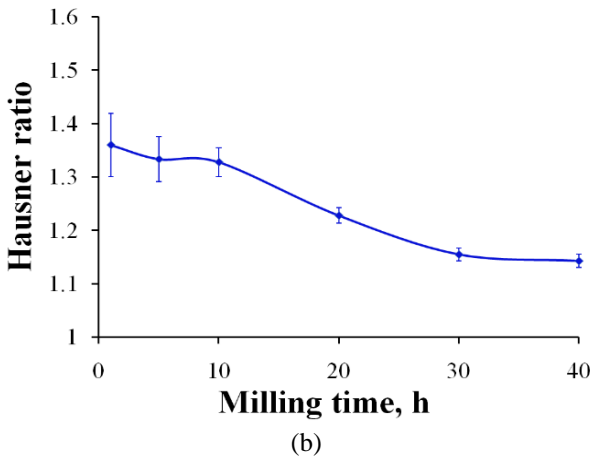
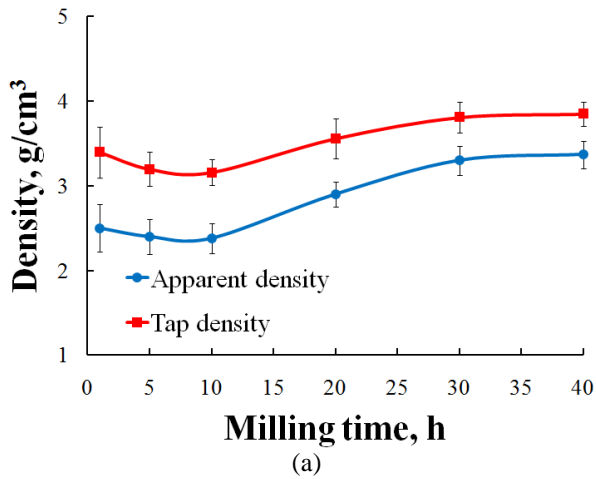


Figure 4. (a) TD and AD versus MM time, and (b) HR versus MM for Ti-50 at. % Cu powder

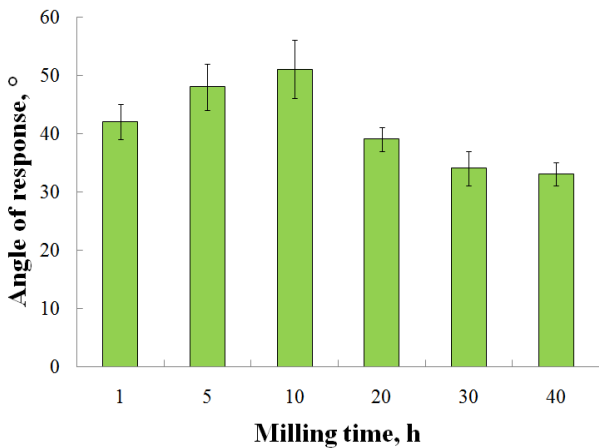


Figure 5. The angle of repose of the alloy powder milled for different times

To assess the variations in the density of the green samples with the milling time, the powders milled for different durations were compacted at 600 MPa. Figure 6

depicts the relationship between the compact density and milling time. Although the flowability of the powder increases with the milling time owing to work hardening and formation of a hard TiCu phase, the plastic deformation capacity of the powder during compression diminishes, resulting in a decrease in density. Owing to the hardening effect of mechanical milling, the green density of the compacts tends to decrease upon increasing milling duration for the metallic powders. In Figure 6, plastic deformation was found to be important for determining the green density of a powder. In terms of green density, powders with excellent plastic deformation properties (with a shorter milling time) showed the highest values.

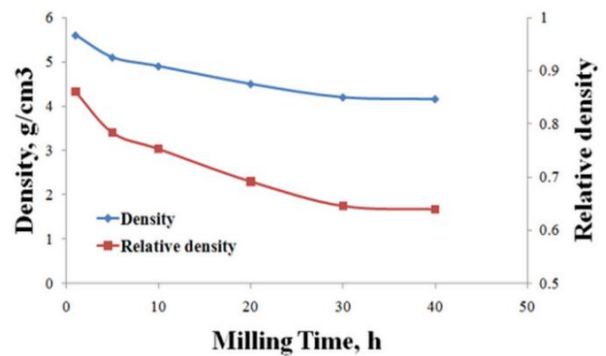


Figure 6. Variations in the density of green samples compressed at 600 MPa pressure with milling time

3.3. Compressibility of TiCu powder

Figure 7 depicts the compressibility curve of the TiCu powder milled for 30 hours and compacted under various pressures. The Ti-Cu powder milled for 30 hours has an intermetallic TiCu structure and high hardness. As the applied pressure increased, the relative density increased as well. The densification of metallic powders under pressure is a two-stage process that includes Particle Rearrangement (PR) at low pressure and Plastic Deformation (PD) at high pressures. These mechanisms are usually active simultaneously, particularly at the local scale. The hardness of the TiCu powder was 634 HV. As a result, particle rearrangement plays a major role in densification at low pressures. Linear modified Heckel, Panelli-Filho, and Ge equations as well as non-linear Cooper and Eaton equations [14-17] were used to assess the data compressibility. The Equations are as follows:

$$\text{Heckel: } \ln(1/(1-D)) = K_1 P + B_1 \tag{1}$$

$$\text{Panelli-Filho: } \ln(1/(1-D)) = K_2 \sqrt{P} + B_2 \tag{2}$$

$$\text{Ge: } \log[\ln(1/(1-D))] = K_3 \log(P) + B_3 \tag{3}$$

Cooper and Eaton:

$$(1/D_0 - 1/D)/(1/D_0 - 1) = A_1 \exp(C_1/P) + A_2 \exp(C_2/P) \quad (4)$$

where D_0 , P , and D represent the initial relative density of the powder, applied pressure, and relative density under the applied pressure, respectively. The densification indexes K_1 , K_2 , and K_3 describe the ease with which the powder can be compacted by both PR and PD under an applied load. The constants C_1 and C_2 describe the pressures at which this two-stage densification is expected to occur.

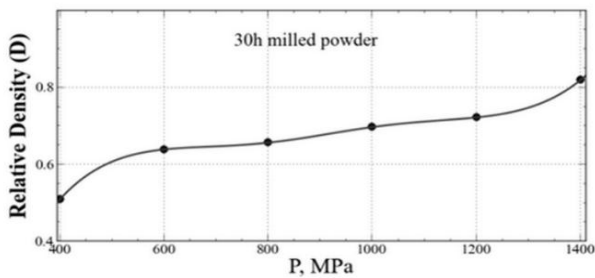


Figure 7. Compaction pressure effects on the relative density of TiCu mechanically milled for 30 h

To determine the densification behavior of the TiCu powder, the experimental data shown in Figure 7 were fitted with several linear and nonlinear equations (Figures 8 and 9). Curve Expert Professional software was utilized to carry out the statistical analysis (Version 1.6.5). Table 3 summarizes the results. The Cooper and Eaton non-linear equation fits the experimental findings for TiCu powder quite well, according to the analysis of variance with a high coefficient of determination ($R^2 = 0.992$). The maximum coefficient of determination was obtained using the Cooper and Eaton equation. coefficients of determination of the linear equations were < 0.976 .

An illustration of the roles of the PR ($A_1 \exp(C_1/P)$) and PD ($A_2 \exp(C_2/P)$) mechanisms in TiCu powder densification is shown in Figure 9. According to the figure analysis, the PR significantly contributes to densification and increases with increasing pressure. However, the PD mechanism significantly contributes to densification at pressures higher than 1400 MPa. According to this study, a nonlinear Cooper-Eaton equation can accurately describe the densification behaviour of TiCu powder.

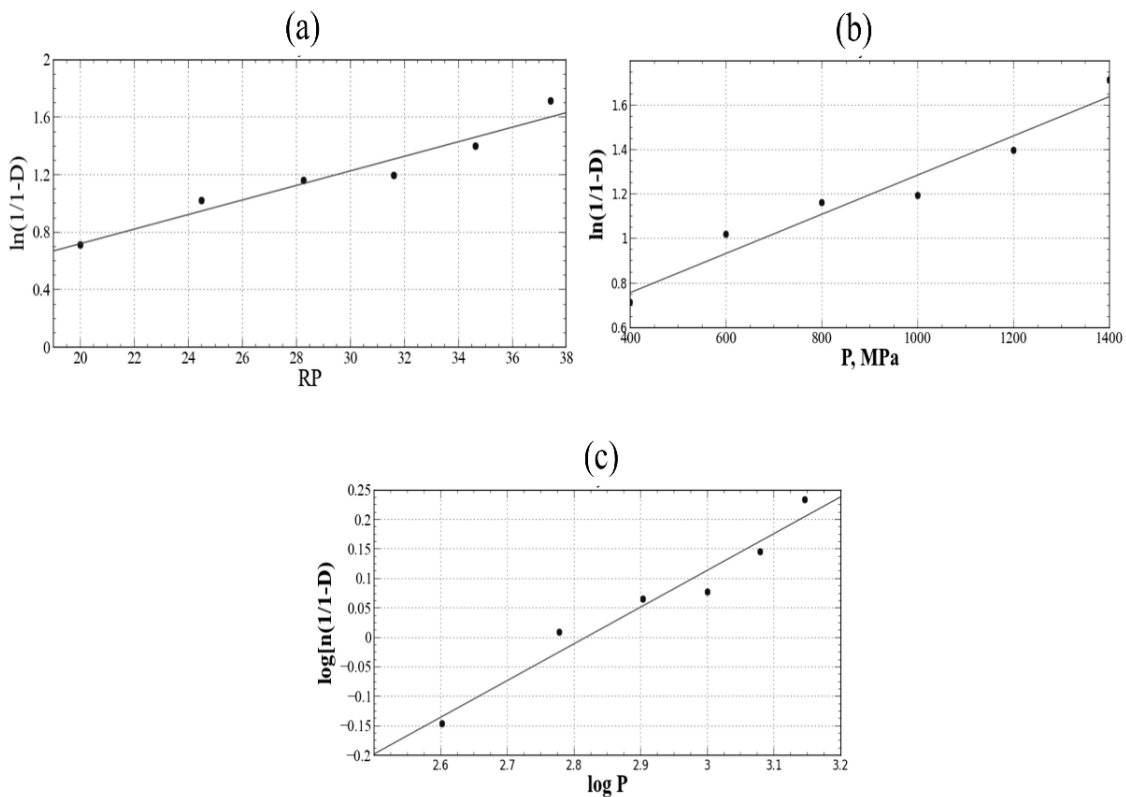


Figure 8. Experimental data of TiCu nanostructured powder, fitted by linear modified Heckel (a) , Panelli-Filho (b), and Ge (c) equations

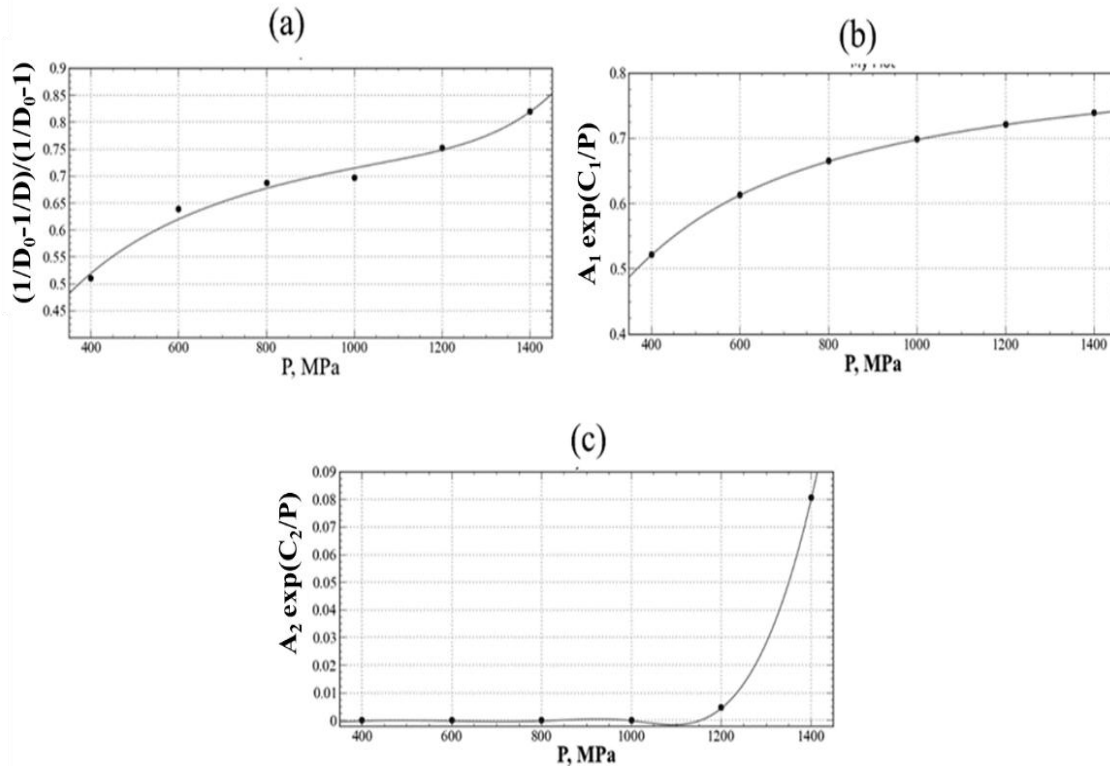


Figure 9. Experimental data of TiCu nanostructured powder, fitted by Cooper and Eaton non-linear equation (a), and the contribution of (b) particle rearrangement ($A_1 \exp(C_1/P)$), and (c) plastic deformation ($A_2 \exp(C_2/P)$) mechanisms on the densification of the powder

TABLE 2. An analysis of the compressibility of TiCu powder using linear compaction equations. R^2 represents the coefficient of determination and MPa^{-1} is the dimension of densification indexes

Heckel		Panelli-Filho		Ge		Cooper and Eaton non-linear equation				
K_1	R^2	K_2	R^2	K_3	R^2	A_1	A_2	C_1	C_2	R^2
0.009	97.3	0.05	96.8	0.62	97.6	$6.5E+03$	$1.6E+04$	0.88	211.1	99.2

4. CONCLUSION

The microstructural and morphological evolution, flowability, and compressibility of the Ti-50 at. % Cu powder milled for different times were investigated in this study. Followed by an increase in the milling time, the change in the powder size and morphology was similar to that of the pure metal. Increasing the milling time up to 10 hours reduced the tap and apparent densities of the alloy; however, further milling improved them. The green density of the powder mixture was reduced after milling. After milling for 10 hours, the AOR of the powder increased, indicating a greater force between the particles and a decreased flowability. Increasing the milling time from 10 to 40 hours reduced the AOR of the powder and improved the alloy flowability, thus making it suitable for consolidation. The determining factor in the flowability of this powder is its morphological change from a flake to equiaxed. A mathematical model for the

compressibility of metallic alloyed powders (e.g., TiCu powder) was proposed using linear and non-linear compaction equations. A comparison of the linear and non-linear equations revealed that Cooper and Eaton's non-linear equation provided the best fit. Particle rearrangement was found to play a significant role in the densification process, and this effect was intensified with pressure. Plastic deformation was negligible under the applied pressure of 1200 MPa.

ACKNOWLEDGEMENTS

The author wish to acknowledge University of Maragheh for the all support throughout this work.

REFERENCES

1. Pripanapong, P., Tachai, L., "Microstructure and mechanical

- properties of sintered Ti-Cu alloys”, *Advanced Materials Research*, Vol. 93-94, (2010), 99-104. <https://doi.org/10.4028/www.scientific.net/AMR.93-94.99>
2. Zhang, E., Ren, J., Li, S., Yang, L., Qin, G., “Optimization of mechanical properties, biocorrosion properties and antibacterial properties of as-cast Ti-Cu alloys”, *Biomedical Materials*, Vol. 11, No. 6, (2016), 065001. <https://doi.org/10.1088/1748-6041/11/6/065001>
 3. Zhang, E., Liu, C., “Effect of surface treatments on the surface morphology, corrosion property, and antibacterial property of Ti-10Cu sintered alloy”, *Biomedical Materials*, Vol. 10, No. 4, (2015), 045009. <https://doi.org/10.1088/1748-6041/10/4/045009>
 4. Ohkubo, C., Shimura, I., Aoki, T., Hanatani, S., Hosoi, T., Hattori, M., Oda, Y., Okabe, T., “Wear resistance of experimental Ti-Cu alloys”, *Biomaterials*, Vol. 24, No. 20, (2003), 3377-3381. [https://doi.org/10.1016/S0142-9612\(03\)00157-1](https://doi.org/10.1016/S0142-9612(03)00157-1)
 5. Akbarpour, M. R., Javadhesari, S. M., “Wear performance of novel nanostructured Ti-Cu intermetallic alloy as a potential material for biomedical applications”, *Journal of Alloys and Compounds*, Vol. 699, (2017), 882-886. <https://doi.org/10.1016/j.jallcom.2017.01.020>
 6. Javadhesari, S. M., Alipour, S., Akbarpour, M. R., “Biocompatibility, osseointegration, antibacterial and mechanical properties of nanocrystalline Ti-Cu alloy as a new orthopedic material”, *Colloids and Surfaces B: Biointerfaces*, Vol. 189, (2020), 10889. <https://doi.org/10.1016/j.colsurfb.2020.110889>
 7. Liu, J., Zhang, X., Wang, H., Li, F., Li, M., Yang, K., Zhang, E., “The antibacterial properties and biocompatibility of a Ti-Cu sintered alloy for biomedical application”, *Biomedical Materials*, Vol. 9, No. 2, (2014), 025013. <https://doi.org/10.1088/1748-6041/9/2/025013>
 8. Javadhesari, S. M., Alipour, S., Akbarpour, M. R., “Effects of SiC nanoparticles on synthesis and antimicrobial activity of TiCu nanocrystalline powder”, *Ceramics International*, Vol. 46, No. 1, (2020), 114-120. <https://doi.org/10.1016/j.ceramint.2019.08.240>
 9. Javadhesari, S. M., Alipour, S., Akbarpour, M. R., “Microstructural characterization and enhanced hardness, wear and antibacterial properties of a powder metallurgy SiC/Ti-Cu nanocomposite as a potential material for biomedical applications”, *Ceramics International*, Vol. 45, No. 8, (2019), 10603-10611. <https://doi.org/10.1016/j.ceramint.2019.02.127>
 10. Han, Y., Wang, H. R., Cao, Y. D., Hou, W. T., Li, S. J., “Improved corrosion resistance of selective laser melted Ti-5Cu alloy using atomized Ti-5Cu powder”, *Acta Metallurgica Sinica (English Letters)*, Vol. 32, (2019), 1007-1014. <https://doi.org/10.1007/s40195-019-00896-1>
 11. Zong, W., Zhang, S., Zhang, C., Ren, L., Wang, Q., “Design and characterization of selective laser-melted Ti6Al4V-5Cu alloy for dental implants”, *Materials and Corrosion*, Vol. 71, No. 10, (2020), 1697-1710. <https://doi.org/10.1002/maco.202011650>
 12. Shon, I. J., Kim, N. R., Du, S. L., Ko, I. Y., Cho, S. W., Kim, W., “Rapid consolidation of nanostructured TiCu compound by high frequency induction heating and its mechanical properties”, *Materials Transactions*, Vol. 51, No. 11, (2010), 2129-2131. <https://doi.org/10.2320/matertrans.M2010251>
 13. Akbarpour, M. R., Hesari, F. A., “Characterization and hardness of TiCu-Ti₂Cu₃ intermetallic material fabricated by mechanical alloying and subsequent annealing”, *Materials Research Express*, Vol. 3, No. 4, (2016), 045004. <https://iopscience.iop.org/article/10.1088/2053-1591/3/4/045004>
 14. Hesabi, Z. R., Hafizpour, H. R., Simchi, A., “An investigation on the compressibility of aluminum/nano-alumina composite powder prepared by blending and mechanical milling”, *Materials Science and Engineering: A*, Vol. 454, (2007), 89-98. <https://doi.org/10.1016/j.msea.2006.11.129>
 15. Nazari, K. A., Nouri, A., Hilditch, T., “Compressibility of a Ti-based alloy with varying amounts of surfactant prepared by high-energy ball milling”, *Powder Technology*, Vol. 279, (2015), 33-41. <https://doi.org/10.1016/j.powtec.2015.03.044>
 16. Sivasankaran, S., Sivaprasad, K., Narayanasamy, R., Iyer, V. K., “An investigation on flowability and compressibility of AA 6061_{100-x} wt.% TiO₂ micro and nanocomposite powder prepared by blending and mechanical alloying”, *Powder Technology*, Vol. 20, No. 1, (2010), 70-82. <https://doi.org/10.1016/j.powtec.2010.03.013>
 17. Ramírez-Vinasco, D., León-Patiño, C. A., Aguilar-Reyes, E. A., Rodríguez-Ortiz, G., “Compressibility behaviour of conventional AlN-Cu mixtures and Cu-(AlN-Cu) composite powder mixtures”, *Powder Technology*, Vol. 403, (2022), 117385. <https://doi.org/10.1016/j.powtec.2022.117385>



Materials and Energy Research Center

MERC

Contents lists available at [ACERP](#)

Advanced Ceramics Progress

Journal Homepage: www.acerp.ir

Advanced Ceramics Progress

Original Research Article

The Effect of Temperature and Al as an Additive on the Synthesis, Structure, Densification, and Conductivity of Garnet-Type $\text{Li}_7\text{La}_3\text{Zr}_2\text{O}_{12}$

Leila Rezazadeh ^a, Susan Hasheminia ^a, Zahra Khakpour ^b, *^a Assistant Professor, Department of Mechanic, Marand Branch, Islamic Azad University, Marand, Iran^b Assistant Professor, Department of Ceramic, Materials and Energy Research Center, Karaj, Iran* Corresponding Author Email: z.khakpour@merc.ac.ir (Z. Khakpour)URL: https://www.acerp.ir/article_172226.html

ARTICLE INFO

A B S T R A C T

Article History:

Received 26 February 2023
 Received in revised form 21 May 2023
 Accepted 06 June 2023

Keywords:

Li Solid State Electrolyte
 Synthesis
 Densification
 Ionic Conductivity

Garnet-type $\text{Li}_7\text{La}_3\text{Zr}_2\text{O}_{12}$ (LLZO) solid-state electrolytes are promising candidates for application in next-generation solid-state batteries. Of note, the most controversial issue is to stabilize the cubic phase structure (c-LLZO) with high density after the sinter process to reach high ionic conductivity with the desired strength. Considering this issue, the current study aims to investigate the synthesis and sintering of LLZO with Al substituted and without any additive. The LLZO ceramic was synthesized through conventional solid-state reaction. The effect of heating temperature on the synthesis of the cubic structure was studied using X-Ray Diffraction (XRD). The ionic conductivity of the samples was examined by AC Impedance Spectroscopy. The obtained results indicated that Al doping led to the cubic phase stabilization and that it had a positive effect on the sintering regime so that the sample with Al dopant was densified at the lower temperature of 1140 °C. The total ion conductivity of Al-LLZO is 0.1 mS cm^{-1} which is comparable to the values of high temperature-sintered samples.


<https://doi.org/10.30501/acp.2023.387377.1119>

1. INTRODUCTION

Nowadays, energy crisis is one of the most critical challenges facing most countries. In recent decades, the significant reduction in fossil fuel reserves as well as considerable increase in the environmental pollution caused by fossil fuels consumption have forced governments and industries to find solutions to these problems and achieve superior technology in the field of energy production. Since exploitation of non-conventional energy sources such as wind, solar or nuclear sources is bound to some limitations, the focus is more on the use of batteries and fuel cells to store and

produce as much energy as possible [1,2]. Among different types of commercial batteries such as lead, nickel-cadmium, nickel-hydrogen, and lithium batteries, lithium batteries enjoy the energy density of about ten times higher than that of lead and nickel-cadmium batteries in theory. In addition, from an environmental point of view, the presence of toxic elements such as cadmium and lead in these batteries is considered a severe problem such as the expansion of the market for nickel-hydrogen batteries [3]. However, the energy density of these batteries is theoretically still about one-fifth of that of the rechargeable lithium batteries. Lithium batteries have the highest electric driving force (emf)

Please cite this article as: Rezazadeh, L., Hasheminia, S., Khakpour, Z., "The Effect of Temperature and Al as an Additive on the Synthesis, Structure, Densification, and Conductivity of Garnet-type $\text{Li}_7\text{La}_3\text{Zr}_2\text{O}_{12}$ ", *Advanced Ceramics Progress*, Vol. 9, No. 2, (2023), 16-23. <https://doi.org/10.30501/acp.2023.387377.1119>

2423-7485/© 2023 The Author(s). Published by MERC.

This is an open access article under the CC BY license (<https://creativecommons.org/licenses/by/4.0/>).

among the other types of batteries. Lithium batteries are used in energy storage and other various applications, including energy consumers and energy transmission and production on a very high scale [2,3]. Currently, Lithium hexa-fluoro phosphate (LiPF_6) is practically the only conducting salt used in commercial lithium-ion batteries. However, this type of electrolyte has some major problems and limitations including the leakage of organic electrolytes, freezing at lower temperatures of application environments, and burning at higher temperatures [4,5]. A flexible electrolyte without any leakage is required, especially for energy devices, to enhance the safety levels. To enhance the safety of the LIBs, extended research studies were and still are being conducted to substitute a suitable solid electrolyte (either polymer, or ceramic) with comparable ionic conductivity. However, these polymer and ceramic electrolyte systems have quite low ionic conductivity at the ambient temperature. In ceramic materials, various types of solid-state electrolytes have been investigated, mainly glass or glass ceramics consisting of oxides, sulfides or a mixture of both. Unfortunately, they have either high ionic conductivity or good chemical stability rather than both [5-8]. One of the most recently studied compounds is garnet-type $\text{Li}_7\text{La}_3\text{Zr}_2\text{O}_{12}$ (LLZO) that was first examined by Thangadurai et al. [9]. Among the most important reasons behind the increasing attention to LLZO in this field are its wide electrochemical stability window, high ionic conductivity at room temperature, and non-flammability. In addition, compared to other solid electrolytes such as sulfide-based solid electrolytes, lithium-garnet enjoys more excellent chemical thermodynamic stability and particularly, its greater stability against lithium metal is essential [3,6].

The garnet-type LLZO is generally stabilized in a two-phase structure namely the cubic (space group $\text{Ia}\bar{3}\text{d}$), which is necessary to achieve high ionic conductivity, and tetragonal structure (space group $\text{I4}_1/\text{acd}$), which is thermodynamically more stable at room temperature. On the contrary, ionic conductivity is two to three orders of magnitude lower than usual [8,10]. The main challenge in the synthesis of LLZO is to reach the ideal cubic conductor phase, which is unpractical in every study with the usual sinter of LLZO bodies. However, Murugan et al. [11] obtained a dense cubic phase with high conductivity. Of note, the results obtained from other groups who followed Murugan's method for synthesis and sintering revealed that the final product contained much more stable tetragonal mainly because the tetragonal phase was thermodynamically more stable and was easily obtained through the usual solid-state reaction sintering method in the temperature range of 950-980 °C [12,13]. Researches remark that to stabilize the preferred cubic phase, it is necessary to use higher temperatures while higher temperatures facilitate and speed up the release and loss of lithium from the electrolyte. Consequently, engineering sintering temperature and

storage time, controlling the lithium release reduction, and reaching the cubic phase with the density above 90 % will still remain the essential challenges in the field of LLZO solid electrolyte. Consequently, many researchers in this field have focused on stabilizing the cubic phase. In this regard, many studies on stabilizing the cubic structure of LLZO put their main focus on the dopants such as Al^{3+} , Ga^{3+} , Fe^{3+} substitute for Li^+ sites [6,11,14-18] and Ta^{5+} and Nb^{5+} substitute for Zr^{4+} sites [19,20] to create vacancies in the structure. To lower the sintering temperature, synthesis through a sol-gel process [21] based on the rapid sintering method [22], field-assisted sintering technique [23], and expensive methods such as hot-press or spark plasma sintering methods [24,25] have been investigated. However, using Al, Ga, and Ta as a sintering aid was reported to be effective in increasing the density of the sintered samples [16,17]. In this research, the LLZO electrolyte was synthesized based on a facile solid-state method. In addition, the composition of raw materials was modified, and the synthesis conditions (i.e., temperature, time and atmosphere) were optimized. Finally, the electrochemical analysis was done on the electrolytes by carrying out some detailed tests, evaluating the effects of the composition, grain, and grain boundary conductivity, and determining the best sample for battery construction.

2. MATERIALS AND METHODS

LLZO powder was synthesized through the solid-state method using stoichiometric amounts of Li_2CO_3 , La_2O_3 (preheated at 900 °C for 10 h), ZrO_2 , and Al_2O_3 . An excessive amount of 10 wt. % Li_2CO_3 was then mixed to compensate for the lithium evaporation during the sintering process. The raw materials were mixed through a planetary mill with zirconia balls for six hours in isopropanol under an air atmosphere and then dried at 100 °C. The obtained powder was heated in a furnace in a zirconia crucible (for the sample without Al dopant) and alumina crucible with a lid to prevent lithium loss during heat treatment at 900-1100 °C for 10 h. In the following step, the mixed powder was reground and pressed into pellets with 16.3 mm diameter at 300 MPa, followed by sintering in the temperature range of 1100-1260 °C for 8 h. The pellets were placed in a small crucible surrounded by layers of mother sacrificial powder to suppress the potential volatilization of Li_2O during the preparation.

The phase compositions of the as-synthesized LLZO powders and sintered pellets were studied by X-ray diffractometry (Philips) using $\text{Cu K}\alpha$ radiation ($\lambda = 1.5417 \text{ \AA}$) as the X-ray source in a 2θ range of 10-80 with the step size of 0.02° and step time of 2 s. The relative densities of the obtained ceramic pellets were geometrically estimated and compared to the theoretical density of LLZO. The theoretical density of samples was

calculated from the lattice parameters determined by X-Ray Diffraction (XRD). For the ionic conductivity measurement, gold electrodes were applied to both sides of the sintered bodies by removing the surface layer using a coating of Au paste, drying, and heat treatment at 200 °C for 20 min. The samples were then loaded into a spring-loaded Swagelok cell with stainless steel electrodes. The ionic conductivity tests were carried out in the temperature range of 298-393 K and frequency range of 0.1-2×10⁶ Hz. The samples were first heated up and then cooled down to room temperature to do conductivity measurement so as to eliminate any effect of moisture on conductivity. The complex impedance spectra were analyzed using commercially available Z-View software.

3. RESULTS AND DISCUSSION

Figure 1 demonstrates the XRD patterns of the synthesized LLZO powder without Al dopant heated at 950 °C for 10 h and LLZO pellet sintered at 1250 °C for 8 h. For the sintered sample, the XRD pattern was taken from the crushed pellet. According to the XRD results, the cubic LLZO phase was mainly synthesized at this temperature because it was well matched with the standard pattern known as the cubic garnet phase (PDF# 045-0109). The pyrochlore phase La₂Zr₂O₇, however, was regarded as the majority phase of the synthesized powder at 950 °C, indicating that the interaction between Li₂CO₃ and pyrochlore phase La₂Zr₂O₇ which leads to the synthesis of LLZO is not yet complete at this temperature. There is also a possibility that a proportion of the LLZO phase is the tetragonal phase that cannot be detected in the XRD measurements.

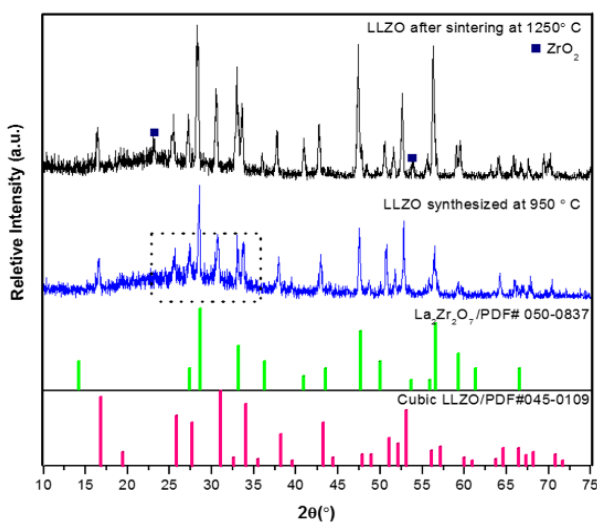
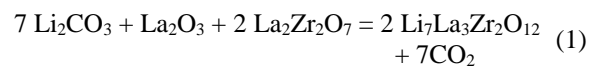


Figure 1. XRD patterns for pure LLZO powder after synthesized at 950 °C for 10 h and pellet after sintered at 1250 °C

Based on some earlier research results [21,26-28], pyrochlore phase La₂Zr₂O₇ is the first phase formed (~ 690 °C) during the synthesis process of LLZO. The following phenomenon is the melting of Li₂CO₃ in the temperature range of 700-750 °C [26]. The carbonate melt can react with other phases (La₂Zr₂O₇, ZrO₂, La₂O₃) which typically results in the LLZO formation in the temperature range of 750-800 °C when the melted Li₂CO₃ reacts with La₂Zr₂O₇ and La₂O₃ according to following equation:



Since the LLZO formation is completed by the melting and reaction of amorphous Li₂CO₃, opting the optimal temperature and reasonable time of the synthesis process is vital. According to the research reports [26], the rate of Li₂CO₃ decomposition is a crucial parameter that determines the LLZO synthesis reaction. The XRD pattern of the synthesized LLZO powder in Figure 1 also illustrates a broad feature, i.e., an amorphous halo, from about 25 to 40 degrees marked by dotted rectangular, confirming that the powder is semi-crystalline or it has an amorphous phase. Consequently, the reaction between the melted Li₂CO₃ and pyrochlore phase has not been yet accomplished at the selected temperature and time. Several studies reported the presence of a secondary La₂Zr₂O₇ phase. For instance, Liu et al. [28] showed that the La₂Zr₂O₇ phase appeared as a second phase in all the synthesized samples; however, it was removed after the sintering process. Figure 1 illustrates the XRD pattern of the sintered sample at 1250 °C for 8 h, showing more substantial peaks belonging to the LLZO phase than the synthesized powder while a considerable amount of pyrochlore phase is still present. In addition, a small amount of ZrO₂ can be detected. In a study by J. Kosir et al. [21], increasing the temperature led to the decomposition of the LLZO due to the faster Li outgassing that facilitated more formation of La₂Zr₂O₇ phase. Consequently, sintering at the high temperature of 1250 °C promoted the formation of off-stoichiometric LLZO compounds and impurities. Figure 2 demonstrates the XRD pattern of the synthesized pure LLZO and Al-doped one at 1100 °C for 10 h. For better comparison and conclusion of the synthesis of Al-doped LLZO, two batches of the weighted stoichiometry of the precursors were prepared to heat up at 950 °C for 8 h and at 1100 °C for 8 h. Upon increasing the temperature, the peaks belonging to C-LLZO get sharper; however, a plenty amount of the unwanted pyrochlore phase is still present and did not disappear. There is also a deviation from the base line in the same range of the XRD as there is in the XRD pattern of pure LLZO at 950 °C (marked by the dotted line in Figure 2).

In this regard, it can be concluded that even by increasing the synthesis temperature up to 1100 °C, the reaction between the melted Li_2CO_3 and pyrochlore phase will not be complete yet. Figure 2 demonstrates the XRD pattern of the $\text{Li}_{6.85}\text{Al}_{0.15}\text{La}_3\text{Zr}_2\text{O}_{12}$ sample after heating at 950 °C and 1100 °C.

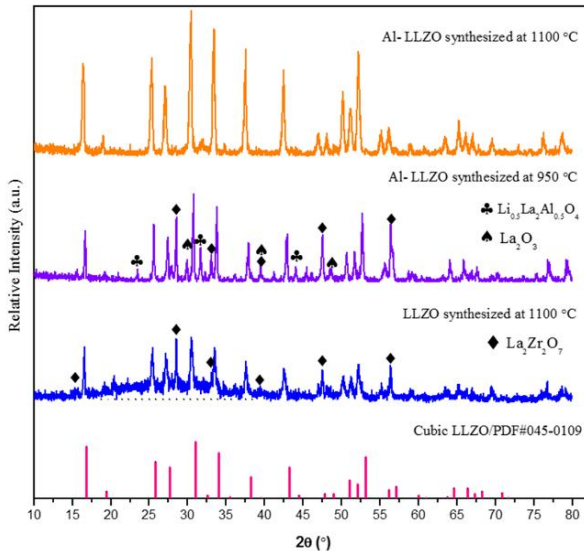


Figure 2. XRD patterns of pure LLZO and Al-LLZO powder synthesized at 950 °C and 1100 °C for 10 h

Accordingly, all the diffraction peaks of the sample heated at 1100 °C can be assigned to the cubic garnet structure. Of note, the final reaction of the sample heated at 950 °C is not complete, and there are still some middle phases present.

As observed, the cubic phase LLZO was synthesized at the lower temperature of 950 °C with other phases of $\text{La}_2\text{Zr}_2\text{O}_7$, $\text{Li}_{0.5}\text{La}_2\text{Al}_{0.5}\text{O}_4$, and La_2O_3 still present in lower amounts.

The XRD data of Al-LLZO synthesized at 1100 °C shows very strong and sharp peaks without any shoulder, compared to the pure LLZO (1100 °C), confirming the formation of good crystallinity and high purity of the cubic LLZO.

In order to consider the effect of Al on the sintering and densification of the compounds, pure LLZO and Al-LLZO synthesized at 1100 °C were selected due to the pure LLZO-1100 diffraction peaks assigned to a garnet structure, showing stronger peaks than the same one synthesized at 950 °C. Although the powders were uniaxially pressed and subjected to the same sintering conditions at 1200 °C, eight hours is needed to form dense ceramic pellets, and the densification results were completely different between pure LLZO and Al-LLZO. In the aluminum-doped sample, the specimens under the sintering conditions were bloated and melted in some areas, and 60 % of the theoretical density was the relative density of pure LLZO. As a result, Al-LLZO was sintered at lower temperatures while the pure LLZO was sintered at higher temperatures (i.e., 1230 °C and 1260 °C). Calculation of the geometrical relative densities confirmed that the density increased up to ~90 % for the Al-LLZO pellets at the temperatures of 1170 °C and 1140 °C for 8 h. On the contrary, the density of pure LLZO increased up to 68 % with an increase in the sintering temperature up to 1260 °C for 8 h.

The XRD pattern of pure LLZO (Figure 3) is characterized by strong peaks for $\text{La}_2\text{Zr}_2\text{O}_7$ as well as minor characteristic peaks indexed to the LLZO phase.

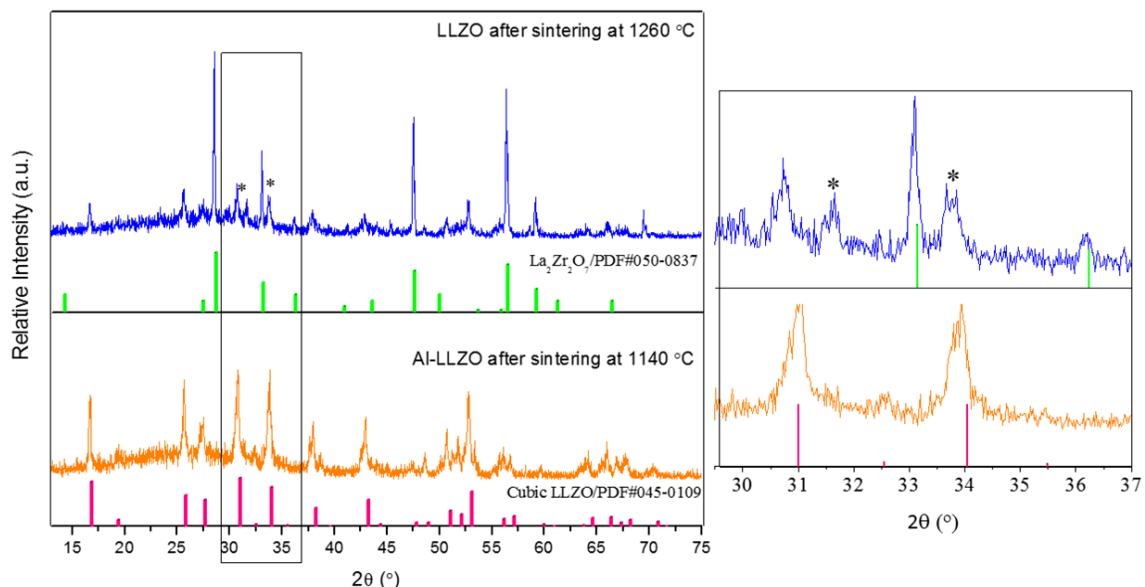


Figure 3. XRD patterns of pure LLZO and Al-LLZO powder synthesized at 950 °C and 1100 °C for 10 h

Compared to the synthesized LLZO powder before sintering (Figure 2), the pure LLZO sample is characterized by a reduction in the peak intensity of the garnet LLZO phase whose diffraction patterns contains both tetragonal and cubic phases, as demonstrated in the magnified view, which shows the split peaks compared to the cubic structure materials. The peaks at $2\theta \approx 31$ and $2\theta \approx 34$ marked by stars in Figure 3 can be split into two peaks that are indicative of the presence of t-LLZO [13]. The XRD pattern of Al-LLZO after sintering (Figure 3) is found to be the cubic garnet LLZO structure with no secondary phases found in the diffraction pattern. Of note, the reduction in the peak intensity of the sintered sample, compared to the Al-LLZO sample, before sintering is notable. Figure 4 illustrates the digital images of the prepared ceramic samples according to which, the sintering ability of pure LLZO sample was quite weak and consequently, it could not be densified properly even by increasing the temperature up to 1260 °C. In contrast to the pure LLZO sample, the Al-LLZO pellet has dense appearance with uniform coloration which is consolidated into a dense body (Figure 4c). A comparison between Figure 4b and 4c reveals that the significant increase in the densities of the Al-LLZO and pure LLZO samples confirms the change in their structures as well as characteristics. While all pure samples sintered between 1200-1260 °C did not densify to reach acceptable pellet densities of over 70 % and remained in a powdered state after sintering (cracked during handling), the Al-LLZO samples were densified at the reduced temperature of 1140 °C with the density of ~ 90 %. A. Paoella et al. [26] investigated the impact of lithium loss during the sintering process of c-LLZO and reported that the pure c-LLZO was metastable and dependent on the sintering time. During the sintering process, the cubic-LLZO becomes tetragonal phase at 1100 °C in the presence of gas flow. As a result, the cubic-LLZO becomes metastable and between c-LLZO and $\text{La}_2\text{Zr}_2\text{O}_7$ impurity before sintering, lithium migration reaction under gas flow occurs. The cubic phase was preserved by intensifying the $\text{La}_2\text{Zr}_2\text{O}_7$ phase, probably due to the lithium loss under no gas flow condition. Therefore, to avoid the pyrochlore $\text{La}_2\text{Zr}_2\text{O}_7$ phase, it is vital to maintain as much lithium as possible. C. Lopez et al. [29] provided a dry O_2 atmosphere to control the sintering conditions and reported the density value of 70 % for the Ga-doped LLZO samples sintered in air at 1085 °C. The density, however, increased as high as 94 % of the theoretical density of the samples sintered in dry O_2 . In their research, J. Kosir et al. [21] concluded that the higher amount of excess Li (more than 10 %) along with adding Al as the dopant are the main keys to obtain the densified sample. S. Afyon et al. [30] studied the synthesis of Ga doped Li garnet structure through the modified sol-gel combustion method and showed that lowering the overall powder processing and sintering temperature was both advantageous to avoid Li-losses

and an alternative strategy for stabilizing the cubic phase. Another research [18,21] on the Al-doped LLZO confirmed the promoted sintering of samples with the hypothesis that the reaction between Li_2O and Al_2O_3 would form a liquid phase, such as LiAlO_2 , which enabled a liquid sintering and accelerated densification [28]. Therefore, dopants such as Al can be used to produce the cubic LLZO by lowering the lithium content to create Li vacancies disrupting the long-range lithium order to stabilize cubic structure at room temperature [31]. Moreover, Al_2O_3 assisted in sintering and densification at the lower temperature 1140 °C, rather than above 1200 °C. Here, a lower sintering temperature is more preferable and suitable mainly because it ensures a better morphology and reduces lithium loss during heating.

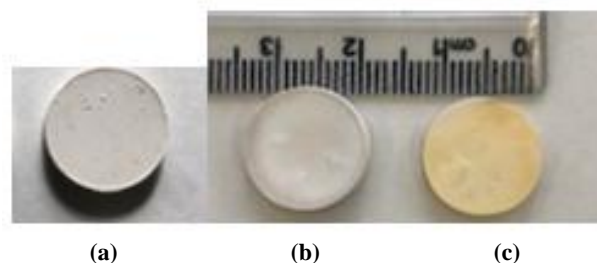


Figure 4. Picture of the LLZO pellets (a) before sintering; (b) LLZO pellet obtained after sintering at 1260 °C for 8 h; (c) Al-LLZO pellet obtained after sintering at 1140 °C for 8 h

Figure 5 presents the results of the AC conductivity measurements (in Nyquist format) for the Al-LLZO sample using Au blocking electrodes in the temperature range of 25-120 °C in the air.

Typically, impedance spectra are composed of three parts based on the frequency range measurement: the high-frequency range corresponds to the bulk resistance, intermediate-frequency flattened semicircle represents the grain-boundary resistance, and low-frequency spike stands for the contribution of the electrode. The Nyquist plots of the Al-LLZO represent only one clear semicircle in the high-frequency region which is attributed to the total conductivity of the Al-LLZO sample and fitted with an equivalent circuit presented in the inset of Figure 5. In this figure, the distance from zero to the intercept of the linear tail with the real axis is the total conductivity. Accordingly, the total ionic conductivity values of the Al-LLZO sintered at 1140 °C were 0.1, 0.28, 0.48, 0.7, and 1.0 mS cm^{-1} at the temperatures of 25 °C, 50 °C, 100 °C, and 120 °C, respectively.

These values are in good agreement with those reported in other studies [26,27,29,32,33]. Of note, in some of these research, operating different atmosphere [29], adding other additives such as Ga, Ta, and using the advanced sintering technics [23] were taken into consideration.

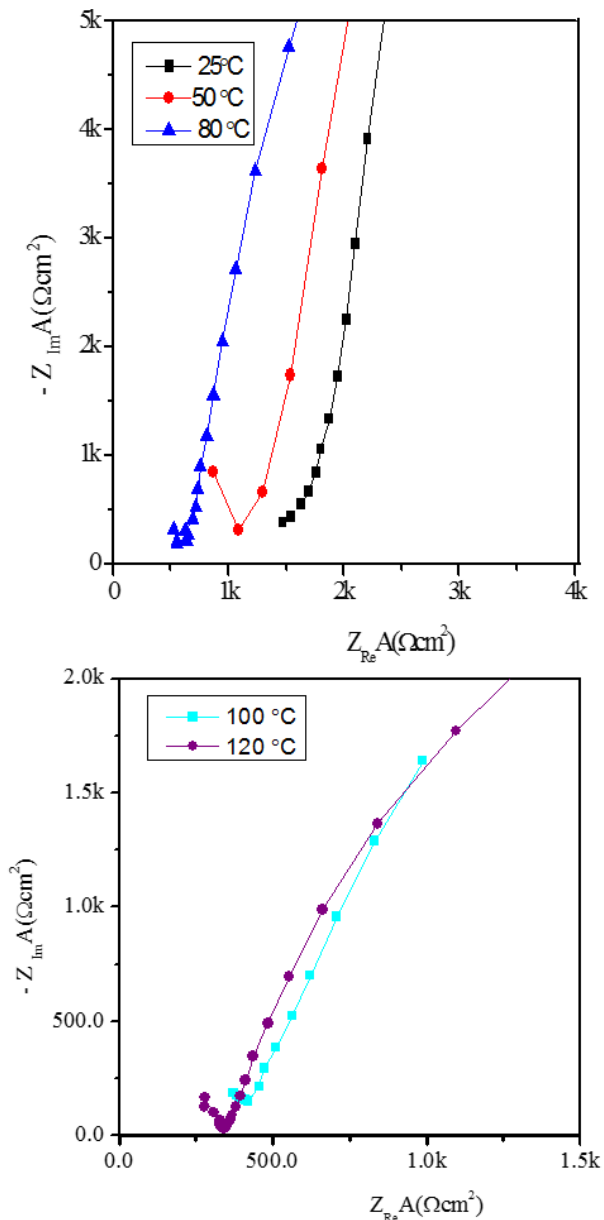


Figure 5. The impedance plots for the Al-LLZO sample sintered at 1140 °C measured at 25, 50, 80, 100, and 120 °C

The Arrhenius equation was used to calculate the activation energy E_a :

$$\sigma T = A \exp\left(\frac{-E_a}{k_B T}\right) \quad (2)$$

where σ is the ionic conductivity (Scm^{-1}), A a pre-exponential parameter, k the Boltzmann's constant, and T the absolute temperature. According to Figure 6, the activation energy E_a was measured as 0.27 eV in the temperature range of 25-130 °C, representing high-quality microstructure for moving lithium ions. Since Al-doped sample in this study exhibited the desired

sintering behavior and just reached the acceptable density at 1140 °C, the significant role of Al in stabilizing the cubic structure and densification should be proved that would finally lower the activation energy needed for lithium movement in the structure.

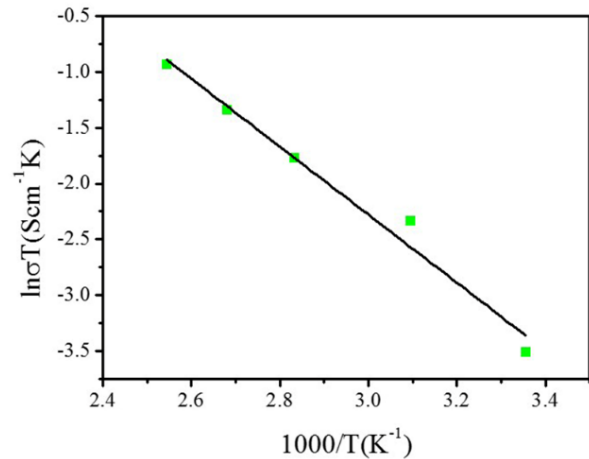


Figure 6. Arrhenius plot of Al-LLZO sample sintered at 1140 °C for 8 h

4. CONCLUSION

In our study, the sintering ability of the synthesized LLZO with Al and without any additive was investigated. The undoped LLZO samples resulted in broken or very fragile strength future after sintering at low or even as high as at 1260 °C temperatures. Lithium loss resulted in low density and transforming to an unwanted phase at high temperature. On the other hand, the Al-doped LLZO resulted in the cubic system, high relative density, and high conductivity. The ionic conductivity of Al-LLZO of 0.1 mScm^{-1} is on the same order of magnitude as most as solid-state electrolytes.

ACKNOWLEDGEMENTS

The authors appreciate use of the ceramic laboratories of materials and energy research center and electrochemical lab facilities.

REFERENCES

1. Fallah Vostakola, M., Amini Horri, B., "Progress in material development for low-temperature solid oxide fuel cells: A review", *Energies*, Vol. 14, No. 5, (2021), 1280. <https://doi.org/10.3390/en14051280>
2. Han, X., Gong, Y., Fu, K., He, X., Hitz, G. T., Dai, J., Pearse, A., Liu, B., Wang, H., Rubloff, G., Mo, Y., "Negating interfacial impedance in garnet-based solid-state Li metal batteries", *Nature*

- Materials*, Vol. 16, No. 5, (2017), 572-579. <https://doi.org/10.1038/nmat4821>
- Tarascon, J. M., Armand, M., "Issues and challenges facing rechargeable lithium batteries", *Materials for Sustainable Energy*, Vol. 7, (2010), 171-179. https://doi.org/10.1142/9789814317665_0024
 - Zheng, F., Kotobuki, M., Song, S., Lai, M. O., Lu, L., "Review on solid electrolytes for all-solid-state lithium-ion batteries", *Journal of Power Sources*, Vol. 389, (2018), 198-213. <https://doi.org/10.1016/j.jpowsour.2018.04.022>
 - Zhu, Y., Gonzalez-Rosillo, J. C., Balaish, M., Hood, Z. D., Kim, K. J., Rupp, J. L., "Lithium-film ceramics for solid-state lithionic devices", *Nature Reviews Materials*, Vol. 6, No. 4, (2021), 313-331. <https://doi.org/10.1038/s41578-020-00261-0>
 - Kim, A., Woo, S., Kang, M., Park, H., Kang, B., "Research progresses of garnet-type solid electrolytes for developing all-solid-state Li batteries", *Frontiers in Chemistry*, Vol. 8, (2020), 468. <https://doi.org/10.3389/fchem.2020.00468>
 - Afyon, S., Kravchik, K. V., Wang, S., van den Broek, J., Hänsel, C., Kovalenko, M. V., Rupp, J. L., "Building better all-solid-state batteries with Li-garnet solid electrolytes and metalloid anodes", *Journal of Materials Chemistry A*, Vol. 7, No. 37, (2019), 21299-21308. <https://doi.org/10.1039/c9ta04999a>
 - Thangadurai, V., Narayanan, S., Pinzaru, D., "Garnet-type solid-state fast Li ion conductors for Li batteries: critical review", *Chemical Society Reviews*, Vol. 43, No. 13, (2014), 4714-4727. <https://doi.org/10.1039/c4cs00020j>
 - Thangadurai, V., Weppner, W., "Recent progress in solid oxide and lithium ion conducting electrolytes research", *Ionic*, Vol. 12, (2006), 81-92. <https://doi.org/10.1007/s11581-006-0013-7>
 - Ren, Y., Chen, K., Chen, R., Liu, T., Zhang, Y., Nan, C. W., "Oxide electrolytes for lithium batteries", *Journal of the American Ceramic Society*, Vol. 98, No. 12, (2015), 3603-3623. <https://doi.org/10.1111/jace.13844>
 - Murugan, R., Thangadurai, V., Weppner, W., "Fast lithium ion conduction in garnet-type $\text{Li}_7\text{La}_3\text{Zr}_2\text{O}_{12}$ ", *Angewandte Chemie International Edition*, Vol. 46, No. 41, (2007), 7778-7781. <https://doi.org/10.1002/anie.200701144>
 - Awaka, J., Kijima, N., Hayakawa, H., Akimoto, J., "Synthesis and structure analysis of tetragonal $\text{Li}_7\text{La}_3\text{Zr}_2\text{O}_{12}$ with the garnet-related type structure", *Journal of Solid State Chemistry*, Vol. 182, No. 8, (2009), 2046-2052. <https://doi.org/10.1016/j.jssc.2009.05.020>
 - Logéat, A., Köhler, T., Eisele, U., Stiasny, B., Harzer, A., Tovar, M., Senyshyn, A., Ehrenberg, H., Kozinsky, B., "From order to disorder: The structure of lithium-conducting garnets $\text{Li}_{7-x}\text{La}_3\text{Ta}_x\text{Zr}_{2-x}\text{O}_{12}$ ($x = 0-2$)", *Solid State Ionics*, Vol. 206, (2012), 33-38. <https://doi.org/10.1016/j.ssi.2011.10.023>
 - Rettenwander, D., Wagner, R., Reyer, A., Bonta, M., Cheng, L., Doeff, M. M., Limbeck, A., Wilkening, M., Amthauer, G., "Interface instability of Fe-stabilized $\text{Li}_7\text{La}_3\text{Zr}_2\text{O}_{12}$ versus Li metal", *The Journal of Physical Chemistry C*, Vol. 122, No. 7, (2018), 3780-3785. <https://doi.org/10.1021/acs.jpcc.7b12387>
 - Zhuang, L., Huang, X., Lu, Y., Tang, J., Zhou, Y., Ao, X., Yang, Y., Tian, B., "Phase transformation and grain-boundary segregation in Al-Doped $\text{Li}_7\text{La}_3\text{Zr}_2\text{O}_{12}$ ceramics", *Ceramics International*, Vol. 47, No. 16, (2021), 22768-22775. <https://doi.org/10.1016/j.ceramint.2021.04.295>
 - Matsuda, Y., Sakaida, A., Sugimoto, K., Mori, D., Takeda, Y., Yamamoto, O., Imanishi, N., "Sintering behavior and electrochemical properties of garnet-like lithium conductor $\text{Li}_{6.25}\text{M}_{0.25}\text{La}_3\text{Zr}_2\text{O}_{12}$ (M: Al^{3+} and Ga^{3+})", *Solid State Ionics*, Vol. 311, (2017), 69-74. <https://doi.org/10.1016/j.ssi.2017.09.014>
 - Chen, C., Sun, Y., He, L., Kotobuki, M., Hanc, E., Chen, Y., Zeng, K., Lu, L., "Microstructural and electrochemical properties of Al- and Ga-doped $\text{Li}_7\text{La}_3\text{Zr}_2\text{O}_{12}$ garnet solid electrolytes", *ACS Applied Energy Materials*, Vol. 3, No. 5, (2020), 4708-4719. <https://doi.org/10.1021/acsaem.0c00347>
 - Xue, W., Yang, Y., Yang, Q., Liu, Y., Wang, L., Chen, C., Cheng, R., "The effect of sintering process on lithium ionic conductivity of $\text{Li}_{6.4}\text{Al}_{0.2}\text{La}_3\text{Zr}_2\text{O}_{12}$ garnet produced by solid-state synthesis", *RSC Advances*, Vol. 8, No. 24, (2018), 13083-13088. <https://doi.org/10.1039/C8RA01329B>
 - Wang, R., Liu, F., Duan, J., Ren, Y., Li, M., Cao, J., "Enhanced electrochemical performance of Al- and Nb-codoped LLZO ceramic powder and its composite solid electrolyte", *ACS Applied Energy Materials*, Vol. 4, No. 12, (2021), 13912-13921. <https://doi.org/10.1021/acsaem.1c02644>
 - Yang, L., Tao, X., Huang, X., Zou, C., Yi, L., Chen, X., Zang, Z., Luo, Z., Wang, X., "Efficient mutual-compensating Li-loss strategy toward highly conductive garnet ceramics for Li-metal solid-state batteries", *ACS Applied Materials & Interfaces*, Vol. 13, No. 47, (2021), 56054-56063. <https://doi.org/10.1021/acsaem.1c15115>
 - Košir, J., Mousavihashemi, S., Wilson, B. P., Rautama, E. L., Kallio, T., "Comparative analysis on the thermal, structural, and electrochemical properties of Al-doped $\text{Li}_7\text{La}_3\text{Zr}_2\text{O}_{12}$ solid electrolytes through solid state and sol-gel routes", *Solid State Ionics*, Vol. 380, (2022), 115943. <https://doi.org/10.1016/j.ssi.2022.115943>
 - Yang, L., Dai, Q., Liu, L., Shao, D., Luo, K., Jamil, S., Liu, H., Luo, Z., Chang, B., Wang, X., "Rapid sintering method for highly conductive $\text{Li}_7\text{La}_3\text{Zr}_2\text{O}_{12}$ ceramic electrolyte", *Ceramics International*, Vol. 46, No. 8, (2020), 10917-10924. <https://doi.org/10.1016/j.ceramint.2020.01.106>
 - Zhang, Y., Chen, F., Tu, R., Shen, Q., Zhang, L., "Field assisted sintering of dense Al-substituted cubic phase $\text{Li}_7\text{La}_3\text{Zr}_2\text{O}_{12}$ solid electrolytes", *Journal of Power Sources*, Vol. 268, (2014), 960-964. <https://doi.org/10.1016/j.jpowsour.2014.03.148>
 - Kim, Y., Jo, H., Allen, J. L., Choe, H., Wolfenstine, J., Sakamoto, J., "The effect of relative density on the mechanical properties of hot-pressed cubic $\text{Li}_7\text{La}_3\text{Zr}_2\text{O}_{12}$ ", *Journal of the American Ceramic Society*, Vol. 99, No. 4, (2016), 1367-1374. <https://doi.org/10.1111/jace.14084>
 - Baek, S. W., Lee, J. M., Kim, T. Y., Song, M. S., Park, Y., "Garnet related lithium ion conductor processed by spark plasma sintering for all solid state batteries", *Journal of Power Sources*, Vol. 249, (2014), 197-206. <https://doi.org/10.1016/j.jpowsour.2013.10.089>
 - Paoletta, A., Zhu, W., Bertoni, G., Savoie, S., Feng, Z., Demers, H., Gariepy, V., Girard, G., Rivard, E., Delaporte, N., Guerfi, A., "Discovering the influence of lithium loss on garnet $\text{Li}_7\text{La}_3\text{Zr}_2\text{O}_{12}$ electrolyte phase stability", *ACS Applied Energy Materials*, Vol. 3, No. 4, (2020), 3415-3424. <https://doi.org/10.1021/acsaem.9b02401>
 - Rangasamy, E., Wolfenstine, J., Sakamoto, J., "The role of Al and Li concentration on the formation of cubic garnet solid electrolyte of nominal composition $\text{Li}_7\text{La}_3\text{Zr}_2\text{O}_{12}$ ", *Solid State Ionics*, Vol. 206, (2012), 28-32. <https://doi.org/10.1016/j.ssi.2011.10.022>
 - Liu, K., Ma, J. T., Wang, C. A., "Excess lithium salt functions more than compensating for lithium loss when synthesizing $\text{Li}_{6.5}\text{La}_3\text{Ta}_{0.5}\text{Zr}_{1.5}\text{O}_{12}$ in alumina crucible", *Journal of Power Sources*, Vol. 260, (2014), 109-114. <https://doi.org/10.1016/j.jpowsour.2014.02.065>
 - Bernuy-Lopez, C., Manalastas Jr, W., Lopez del Amo, J. M., Aguadero, A., Aguesse, F., Kilner, J. A., "Atmosphere controlled processing of Ga-substituted garnets for high Li-ion conductivity ceramics", *Chemistry of Materials*, Vol. 26, No. 12, (2014), 3610-3617. <https://doi.org/10.1021/cm5008069>
 - Afyon, S., Krumeich, F., Rupp, J. L., "A shortcut to garnet-type fast Li-ion conductors for all-solid state batteries", *Journal of Materials Chemistry A*, Vol. 3, No. 36, (2015), 18636-18648. <https://doi.org/10.1039/c5ta03239c>
 - Thompson, T., Wolfenstine, J., Allen, J. L., Johannes, M., Huq, A., David, I. N., Sakamoto, J., "Tetragonal vs. cubic phase stability in Al-free Ta doped $\text{Li}_7\text{La}_3\text{Zr}_2\text{O}_{12}$ (LLZO)", *Journal of Materials Chemistry A*, Vol. 2, No. 33, (2014), 13431-13436. <https://doi.org/10.1039/C4TA02099E>
 - Dhivya, L., Karthik, K., Ramakumar, S., Murugan, R., "Facile synthesis of high lithium ion conductive cubic phase lithium garnets for electrochemical energy storage devices", *RSC Advances*, Vol. 5, No. 116, (2015), 96042-96051. <https://doi.org/10.1039/c5ra18543b>

33. Li, Y., Han, J. T., Wang, C. A., Xie, H., Goodenough, J. B.,
“Optimizing Li⁺ conductivity in a garnet framework”, *Journal of*

Materials Chemistry, Vol. 22, No. 30, (2012), 15357-15361.
<https://doi.org/10.1039/C2JM31413D>



Materials and Energy Research Center
MERC

Contents lists available at [ACERP](#)

Advanced Ceramics Progress

Journal Homepage: www.acerp.ir



Original Research Article

Nanoindentation-Based Mechanical Properties Evaluation of Nano-Structure and Composite Plasma Spray Formed Ceramic Nozzles

Sana Seifollahpour ^a, Afshin Ashofteh ^{b,*}, Amir Hossein Shahdadi ^c, Mahmoud Mosavi Mashhadi ^d

^a MSc, School of Mechanical Engineering, College of Engineering, University of Tehran, Tehran, Tehran, Iran

^b Assistant Professor, Mahallat Institute of Higher Education, Mahallat, Markazi, Iran

^c PhD, School of Mechanical Engineering, Sharif University of Technology, Tehran, Tehran, Iran

^d Professor, School of Mechanical Engineering, College of Engineering, University of Tehran, Tehran, Tehran, Iran

* Corresponding Author Email: a.ashofteh@mahallat.ac.ir (A. Ashofteh)

URL: https://www.acerp.ir/article_170954.html

ARTICLE INFO

ABSTRACT

Article History:

Received 28 February 2023
Received in revised form 28 April 2023
Accepted 07 May 2023

Keywords:

Nano Indentation
Plasma Spray Forming
Ceramics
Composites

Ceramic nozzles are unique options in aerospace industry due to their ability to operate at high temperatures. However, their brittleness, structural defects, poor formability, and need for complex methods for measuring their mechanical properties are among the main obstacles to their development. In this study, four different conical nozzles were produced through Plasma Spray Forming (PSF). Given that Yttria-Stabilized Zirconia (YSZ) is one of the most common materials in high-temperature applications, it is considered as the base material. Throughout the research, three YSZ alternatives were investigated by changing the chemical composition (Ceria-Yttria co-Stabilized Zirconia (CYSZ)), by changing the particle size (nanostructured YSZ), and by double layer architecture design. The mechanical properties of the conical nozzles were then evaluated by the nanoindentation test using Oliver and Pharr method. This method can be quick and applicable for evaluation of the mechanical properties of ceramic parts based on the load-depth curve. X-Ray Diffraction (XRD) and Scanning Electron Microscopy (SEM) were performed for the phase analysis and coating microstructure and porosities investigation. The results highlighted the promising features of nano-structured YSZ that are strongly based on the presence of nano-zones inside the coating structure.



<https://doi.org/10.30501/acp.2023.387714.1121>

1. INTRODUCTION

Plasma spraying is a popular deposition method for materials with very high melting point such as ceramics that has been widely used in different industries due to its inexpensiveness (relatively low cost), high velocity, and suitable quality. The deposition process involves melting a ceramic powder using a high-temperature plasma stream, shooting the molten particles to the substrate, and

forming a dense layer. The plasma jet consists of three hot, moderate, and cold regions, depending on the location. A particle can hit the substrate in a melted, semi-melted, and unmelted forms. The most common case of this method application is creation of barrier coatings against oxidation, corrosion, high temperature, etc. [1]. The porous films created by this method are widely used in the automotive, aerospace, and power generation industries, and there are increasing demands

Please cite this article as: Seifollahpour, S., Ashofteh, A., Shahdadi, A., Mosavi Mashhadi, M., "Nanoindentation-Based Mechanical Properties Evaluation of Nano-Structure and Composite Plasma Spray Formed Ceramic Nozzles", *Advanced Ceramics Progress*, Vol. 9, No. 2, (2023), 24-35. <https://doi.org/10.30501/acp.2023.387714.1121>

2423-7485/© 2023 The Author(s). Published by MERC.

This is an open access article under the CC BY license (<https://creativecommons.org/licenses/by/4.0/>).



for their improvements to reach advanced functionality and durability [2]. Therefore, plasma-sprayed coatings protect the substrate from damages in working conditions. On the contrary, the substrate supports the brittle coating. However, this combination can be the source of some damages caused by the inconsistency of the physical and mechanical properties of the substrate (mainly metallic) and the coating (mainly ceramic) [3]. For example, in thermal cycles, Coefficient of Thermal Expansion (CTE) mismatch between the two layers can cause cracks in the coating. In working conditions with limited mechanical loads, the coating can withstand without the substrate support and consequently, separation of the coating from the substrate can prevent any thermal and functional mismatch. An example of Plasma Spray Forming (PSF) is production of high-temperature ceramic nozzles [4].

Nanoindentation technique is an effective procedure for measuring the mechanical properties of materials even in its small volumes and wide acceptance arising from the improvements made within this technique [5]. Nanoindentation is an applicable method for investigating nano-scale mechanical properties such as hardness or Young's modulus and also dislocation nucleation at the nanoscale [6]. Nanoindentation forces the indenter tip into the surface and measures the reflected response and created mark. Mechanical characterization of the phases has an evident advantage [7], and Nanoindentation is an ideal method for measuring material properties at sub-micrometer scales by applying small loads, thus enabling the individual identification of each phase in heterogeneous cases. [8-10]. It can also be very effective for thin films and micro-/nano-electromechanical system (MEMS/NEMS) devices [11,12] that, along with other methods, measures the complex compliance of linearly viscoelastic materials [13,14]. Indenter geometry and variation in a testing method have been already discussed in some works [15,16]. Based on these studies, it can be concluded that this method can be practically and effectively used in ceramic coatings like YSZ fabricated by different methods such as EB-PVD or APS [17-20]. Nanoindentation is also practical in measuring through-thickness and in-plane properties of multi- and single-layer nanocomposite films [21-23]. A literature survey revealed many reports that compared the deposited and bulk properties of ceramics with those of nanoindentation [24]. The potentials of this method are the properties and structural features evaluation of the composites and nanocomposites [25-31].

Owing to its relatively high CTE and low thermal conductivity, YSZ is usually used as a thermal protector at temperatures above 1100 °C. In addition, Ceria-Yttria co-Stabilized Zirconia (CYSZ) is commonly used as a thermal barrier coating on the hot parts of a combustion chamber and the first row of the turbine blades owing to its resistance to thermal shock, low thermal conductivity,

good wear resistance, and high resistance to hot corrosion. According to some research studies, Ceria-Stabilized Zirconia (CSZ) is characterized by more toughness and better thermal shock resistance than YSZ. In addition, yttria is more costly than ceria. The main weakness of CSZ is its significantly lower erosion resistance. Mixing Ceria with Yttria as co-stabilizers and creating CYSZ is a solution that combines the properties of both materials and offers advanced performance [1].

Nanostructured coatings exhibit improved performance due to nano zones. Compared to the conventional coatings, the overall porosity in these coatings does not change much but their distribution becomes uniform in terms of size and position. In material engineering and design, composite and nano-structure coatings are solutions that are considered in many cases [32,33].

In this study, the properties of the YSZ ceramic nozzles are considered as the base, and the effect of changes in the chemical composition, nano structuration, and architecture on the mechanical properties were investigated. In this regard, CYSZ, nanostructured YSZ (YSZ-N), and a layered composite of YSZ-N and CYSZ were first produced by PSF and then, their hardness and elastic modulus were calculated using Oliver-Pharr technique. Based on the results of Nanoindentation, X-Ray Diffraction (XRD), and Scanning Electron Microscopy (SEM) images, the performance and the reasons behind such mechanisms were elaborated.

2. MATERIALS AND METHODS

2.1. Materials

In this study, three different powders including nano- and micro-structured YSZ and CYSZ (Table 1) were used, and the effect of changing different factors on the performance of YSZ, the current conventional material in many high-temperature applications, was investigated.

- Changing the chemical composition by using CYSZ
- Changing microstructure by YSZ nano-structuring (YSZ-N)

Changing the architecture by producing a layered composite structure consisting of YSZ-N and CYSZ.

Accordingly, four different conical ceramic nozzles of YSZ, YSZ-N, and CYSZ, and a composite of YSZ-N and CYSZ were produced by plasma spray forming.

2.2. Mandrel Design

The mandrel was a hollow tapered cylinder with a small slope along its length made from Al 6061 (Figure 1).

The tapered design of the mandrel facilitates the separation process. Aluminum 6061 has a CTE of about $25 \times 10^{-6} \text{ }^\circ\text{C}^{-1}$ which is approximately 2.5 times higher than that of YSZ (10×10^{-6} [34]) and CYSZ. If the mandrel has proper roughness (in our case $0.67 \pm 0.1 \text{ } \mu\text{m}$), different CTEs of the deposited layer and substrate

facilitate better separation. More surface roughness can cause strong mechanical bonds and cracks during cooling

while quite low roughness will decrease the deposition efficiency.

TABLE 1. Characteristics of ceramic powders

	YSZ	CYSZ	YSZ-NANO
Full Name	Yttria Stabilized Zirconia	Ceria-yttria co-stabilized zirconia	Yttria Stabilized Zirconia-nano structured
Formula	ZrO ₂ -8 wt. % Y ₂ O ₃	ZrO ₂ 24CeO ₂ 2.5Y ₂ O ₃	ZrO ₂ -8 wt. % Y ₂ O ₃
Producer	METCO 234A	METCO 205NS	INFRAMAT Nanox TM S4007
Shape	spherical	spherical	spherical
Density	1.8 – 2.4 g/cm ³	2.2 ± 0.1 g/cm ³	1.4 - 1.7 g/cm ³
Melting point	about 2800 °C	about 2800 °C	about 2800 °C
Particle size	50-70 μm	40-50 μm	< 100 nm (agglomerated size: 15-150 μm)

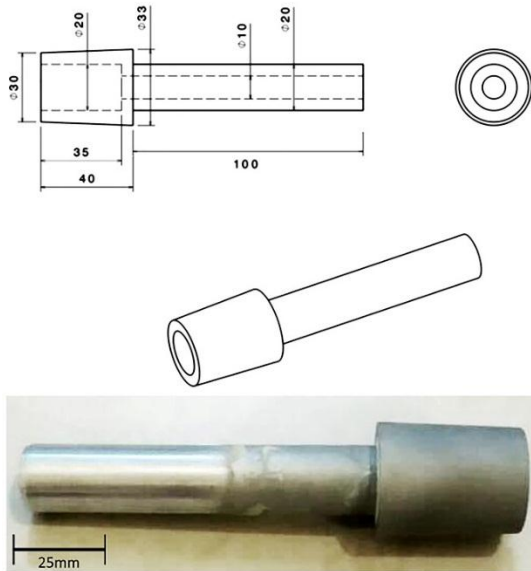


Figure 1. Mandrel used in the plasma spray forming process

2.3. Plasma Spraying

At the beginning of the deposition process, the mandrel was sandblasted with alumina to increase the adhesion of the molten powders to the surface. In the next step, the mandrel was preheated at 200 °C without feeding the powder to prevent thermal shock and damage. In the main spraying process, powders enter the plasma where they melt and accelerate at a very high speed. These melted particles sit on the rotating mandrel and with the linear movement of the spraying gun, a layer will be formed. At the end of each linear movement of the gun, it pauses for 15 seconds to release the residual stresses and then, the next cycle begins. This time allows the stress to release by providing the needed time for heat transfer. Of note, longer pause causes loose connections. The thickness of each deposition round is approximately 100-150 μm. To reach the desired thickness (in this study 450 μm), the deposition process was run three times. Once the process is complete, the coated mandrel is post-heated at 200 °C without powder to prevent cracking and then, it opens from the APS machine and cools down quickly. Plasma spraying parameters were selected in

consultation with experts based on conventional values in high-temperature applications. More details are given in Table 2.

Table 2. Plasma spraying parameters

Parameter	YSZ	CYSZ	YSZ-N
Current (A)	600	600	600
Voltage (V)	55	55	55
Primary gas flow (Ar) (nlpm*)	40	42	35
Secondary gas flow (H ₂) (nlpm)	9	9	9
Carrier gas flow (Ar) (nlpm)	2.5	2.5	2.5
Powder feed rate (gr/min)	50	40	50
Spray distance (mm)	150	150	100
Rotation speed (RPM)	120	120	120
Surface roughness (μm)	0.67±0.1	0.67±0.1	0.67±0.1

* Normal Liter Per Minute

2.4. Separation

The important part of the process is the coating separation from the mandrel. For this purpose, the mandrel is immersed in liquid nitrogen. The difference in the CTE of both mandrel and coating, as well as the conical shape, causes the coating separation. The higher surface roughness, as previously assumed to be essential for successful deposition, can be a reason for the complexity of the separation process. According to Figure 2-b, the ceramic coating is easily separated from the conical part of the mandrel but the part of the coating that was formed on the cylindrical trail of the mandrel is not separated from it. This is another confirmation of the importance of the conical geometry of the mandrel.

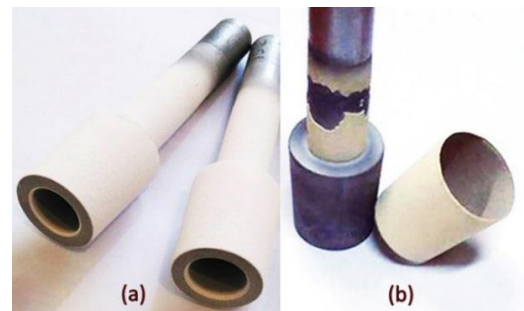


Figure 2. (a) Coated mandrel and (b) nozzle separated from the mandrel

2.5 Theoretical Background

The nanoindentation test involves an indenter (in this study, pyramid-shaped with angle $\alpha = 136^\circ$) that penetrates into the surface to a specified load or depth. Then, it is unloaded as a result of which, penetration depth (h) is measured as a function of load (P). Figure 3 shows an example of the notch created in this test on the polished section of coating.

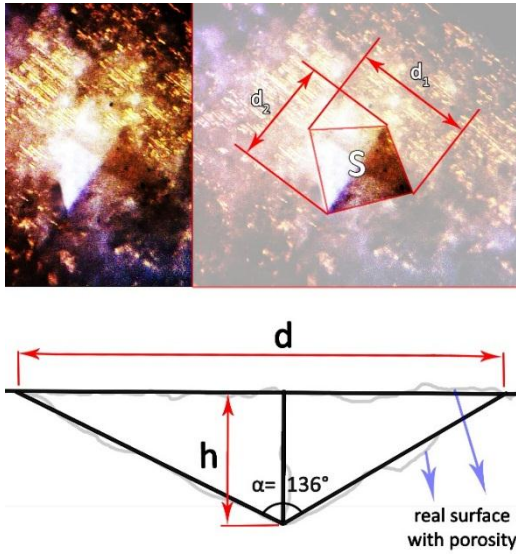


Figure 3. The indenter effect on the surface along with the schematic representation of important elements

Given that the microstructure of the plasma-sprayed ceramic materials is porous, d_1 and d_2 are slightly different from each other. For ease of calculation, their average value $((d_1+d_2)/2)$ is considered as d . Consequently, h can be calculated by Equation (1):

$$\tan\left(\frac{\alpha}{2}\right) = \frac{d}{2h} = \frac{\frac{(d_1+d_2)}{2}}{h} \rightarrow h = \frac{\frac{(d_1+d_2)}{4}}{\tan\left(\frac{\alpha}{2}\right)} \cong \frac{\frac{(d_1+d_2)}{4}}{2.475} \quad (1)$$

$$\rightarrow h \cong \frac{d_1 + d_2}{9.9}$$

Equation (2) shows the projected area of the indented region (S):

$$S = \frac{d_1 \times d_2}{2} \approx \frac{d^2}{2} \approx \frac{(4.95 h)^2}{2} \approx 12.25 h^2 \quad (2)$$

Considering the load P and consequence projected area S , we can measure the hardness HV at that load from Equation (3) [35]:

$$HV = \frac{2 P \sin \frac{136^\circ}{2}}{d^2} = \frac{1.8544 P}{d^2} \quad [\text{kgf/mm}^2] \quad (3)$$

Figure 4 is a typical load-penetration depth curve in which the starting point of the loading process is the origin (O). Followed by applying the load, a diagram similar to L_1 is traversed. After reaching the maximum load (A), the load remains constant while h increases a little (L_2). Once the value of h becomes fixed, unloading begins (L_3). At the end of the path (point C , the load is zero), a residual amount of h will be formed which represents the plastic deformation of the sample. It corresponds to what happens in the stress-strain diagram after removing the load in the plastic area.

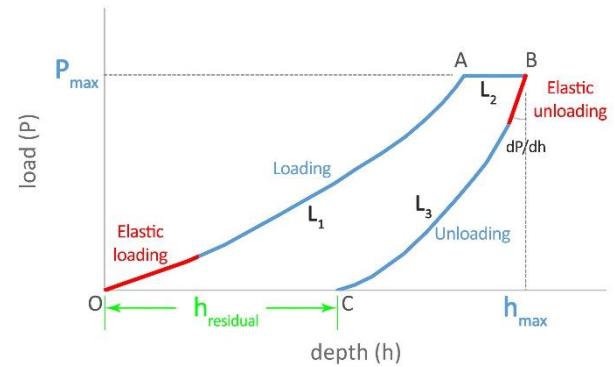


Figure 4. Nanoindentation load-depth curve

Three important parameters must be measured from the P - h curve:

- P_{max} : the maximum load
- h_{max} : the maximum penetration depth
- $\gamma = \frac{dP}{dh}$: the elastic unloading stiffness, defined as the slope of the elastic unloading curve

The quality and preciseness of measurement strongly depend on the experimental measurement of parameters [36]. In this test, the loading and unloading rates are similar but the slopes of the elastic loading and unloading are independent of each other that are determined considering the properties of the material.

The effective elastic modulus, E_f , is calculated using the γ and the S , as shown in Equation (4):

$$E_f = \frac{\sqrt{\pi} \gamma}{2 \beta \sqrt{S}} \quad (4)$$

In the above equation, β has a constant value according to the indenter. Traditionally, this parameter compensates for the stiffness deviations caused by the asymmetry of the pyramidal indenters. It should be noted that β is dimensionless and is normally taken as 1 [33], hence $\beta=1$ in the present study. Reduced modulus (E_r) shows that the measured displacement is a combination of both indenter and sample. Given that, the elastic modulus of the sample (E) can be calculated using the Poisson's ratio of the sample (ν), modulus of the indenter (E_i), and

Poisson's ratio of the indenter (ν_i). The effective elastic modulus is as shown in Equation. (5):

$$\frac{1}{E_f} = \frac{1 - \nu^2}{E} + \frac{1 - \nu_i^2}{E_i} \quad (5)$$

Diamond indenter has $E_i = 1140$ GPa and $\nu_i = 0.07$. The Poisson's ratio of the sample must come from tests on the bulk material or an estimation.

3. RESULTS AND DISCUSSION

In the layered composite structure, CYSZ provides toughness and shock resistance on the working surface, and YSZ works as a support. Given the lower price of CYSZ, it can be concluded that this change can also have cost-reduction effects. Figure 5 represents the SEM image of the elements contained in it. Porosity, which can be seen as the black areas in the image, is formed between the splats during spraying but the vertical cracks are mainly caused by shrinkage after the spraying process [37]. The amounts of Y are 5 % in the upper layer and 1.2 % in the lower layer, which decreased by 76 %. In addition, Zr decreased from 71.3 % to 57.5 %, which is a 19.4 % decrease. This difference is fully evident in Figure 6. In the analysis of the YSZ layer, the amount of Y is only 5 %; however, in the CYSZ layer, the sum of Ce and Y values is equal to 21.3 %.

To check the mechanical properties of the four produced nozzles, the cross-section of each sample was mounted. The indentation effect is smaller than the structural defects such as pores in the coating. In this study, nanoindentation tests were repeated five times, and the average of the obtained results was taken into account (Table 3).

Consideration of the number of repetitions is necessary because the ceramic samples produced by the plasma spraying method have inherently various structural defects and consequently, the properties and microscopic behavior of the material are slightly different at various points. The obtained results are listed in Table 3. In these samples, the largest diameter and depth of the notch were related to the nanostructured YSZ sample, and the

composite, CYSZ, and conventional YSZ samples are in the next ranks. These opposite results were obtained for hardness. According to the findings, the nano-structuration of YSZ would cause extensive changes in properties. A thorough examination of the microstructures shows that in the nano-structured samples, porosities are more uniformly distributed, some of which are present in the nano zones. In these coatings, 16.2 % of the area belongs to nano zones.

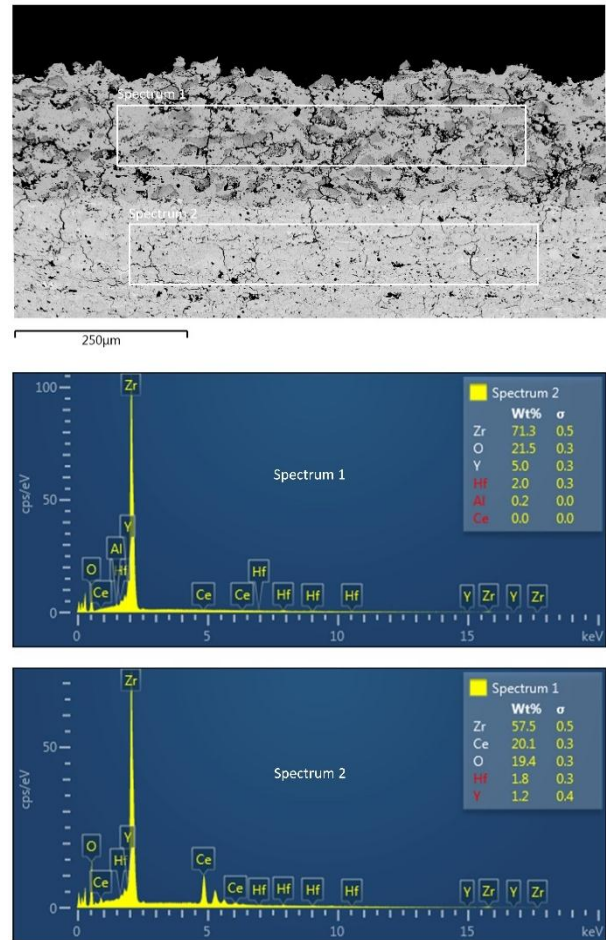


Figure 5. Percentage of elements in the exposed areas in the double-layer composite sample

Table 3. Hardness and depth of the notch for 100g load

	d* (at P=100 g) (μm)						HV (kgf/mm ²)						h** (μm)					
	T1***	T2	T3	T4	T5	Av.	T1	T2	T3	T4	T5	Av.	T1	T2	T3	T4	T5	Av.
YSZ	12.2	12.7	12.6	11.9	12.5	12.4	12.5	11.5	11.7	13.1	11.9	12.1	2.5	2.6	2.5	2.4	2.5	2.5
CYSZ	13.8	13.9	14.2	13.9	14.1	14	9.7	9.6	9.2	9.6	9.3	9.5	2.8	2.8	2.9	2.8	2.8	2.8
YSZ-N	20.2	21	12.7	19.8	12.7	17.3	4.5	4.2	11.5	4.7	11.5	6.2	4.1	4.2	2.6	4	2.6	3.5
C-YN	13.2	19.6	18.2	16.1	14.7	16.4	10.6	4.8	5.6	7.2	8.6	6.9	2.7	4	3.7	3.3	3	3.3

* Average diameter of the pyramid indenter

** Penetration depth

*** Test number 1

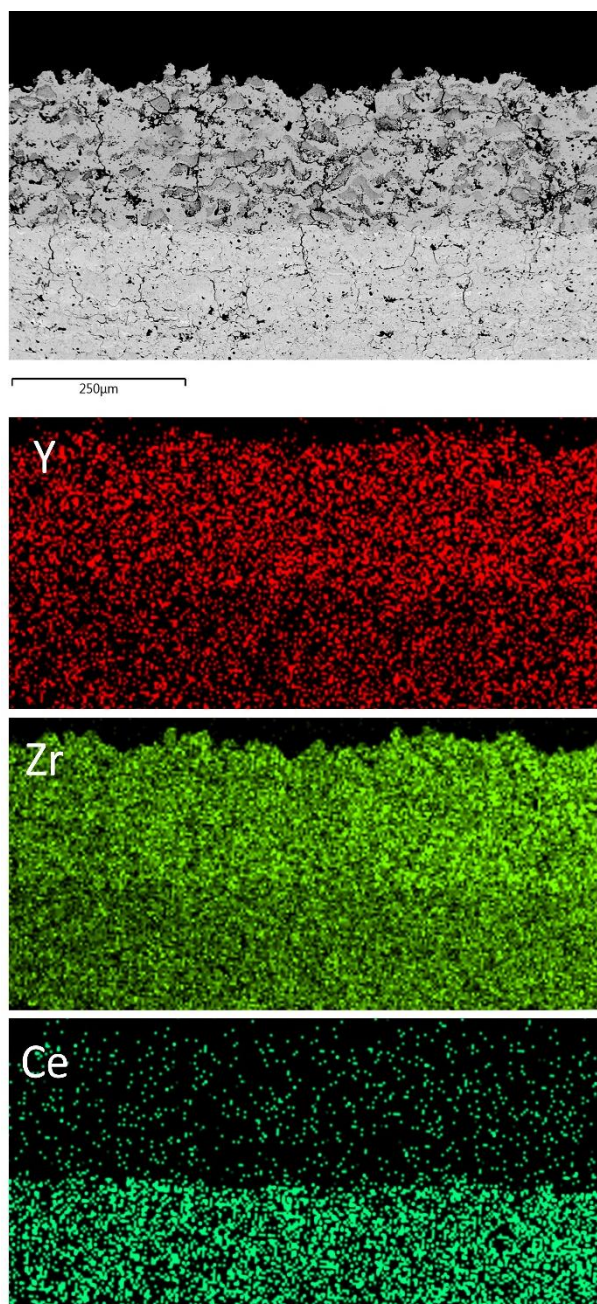


Figure 6. Distribution of elements in each layer of the double-layer composite sample

Nano zones consist of a large number of nanoparticles in nano dimensions that are uniformly distributed. Figure 7 shows the nano zones with high magnification and based on the particle size in this area, it can be concluded that particles will remain nano-structured during the deposition process.

This necessity exists in nanostructure and composite samples with greater intensity. Some samples were also mounted at about 45° angle to check whether there was a difference in the properties of the material in the planes that were angled compared to the perpendicular ones.

Further investigations show that the average results do not differ much in different planes but similar to the vertical plane, the results are slightly different in different locations.

The first investigation was carried out by applying a 100 g load on samples and checking the hardness and depth of the indentation.

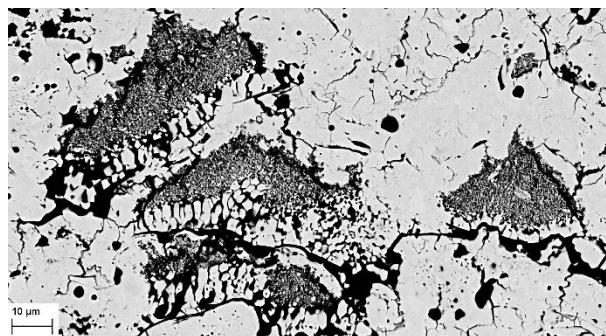


Figure 7. Nano zones with high magnification

As illustrated in the above pictures, large porosities are not observed in these areas (unlike the conventional type). In addition, these areas reduced the brittleness of the structure by creating a barrier against crack growth. As observed in Figure 8, many cracks in the structure stop or change their direction upon reaching the nano regions.

To create nano zones, the spraying parameters must be carefully adjusted at the time of layer deposition. As a result, a part of the nano-powders will be melted while the rest will remain unmelted. In the case of more melting, there is a narrow range where the nanostructure will be destroyed, and the coating will be micro-structured. On the contrary, in case few particles are melted, the connection and integrity of the coating will not be well formed. The adjusted parameters for the powders of this study are given in Table 2. The proper distribution of these particles on the coating surface causes final product gain more structural strength and less brittleness in addition to having the properties of conventional YSZ coatings.

The main elements in the microstructure of each sample are:

- **YSZ:** The porosities and cracks are distributed in the structure but porosities play the main role in its performance. Among all four samples in this study, the highest porosity is related to this material (Table 4).
- **CYSZ:** This coating has a denser structure containing porosities with smaller dimensions and better distribution; however, the number of these structural cracks are more than that of YSZ that play the main role in its performance.
- **YSZ-N:** The main factor causing differences in the performance of this material is the nano zones that in turn create a more uniform microstructure.

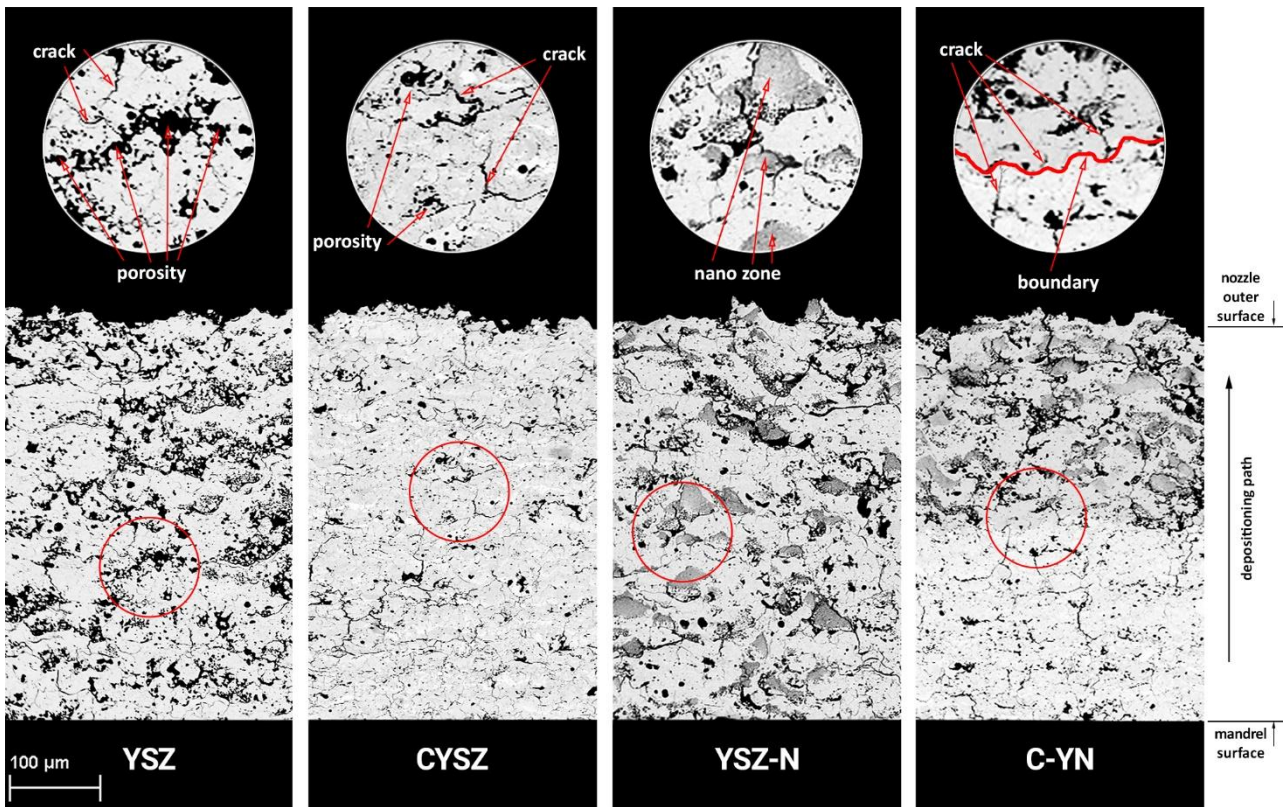


Figure 8. Cross-sectional SEM image of the four samples

- C-YN: The layer boundary plays the main role in this sample. The presence of this element controls the cracks and any damages. If a crack grows in a double-layer structure from the outer surface along the thickness, it will be stopped/weakened after reaching the layer boundary. Figure 8 demonstrates some cracks that stop after reaching the layer boundary.

In all samples, porosities are almost uniformly distributed (Figure 8) and according to Table 4, the amount of porosity has a direct relationship with the hardness. A comparison of the porosity of both YSZ and YSZ-N shows that they are of the same material that fully explains the importance of this parameter.

Table 4. Porosity and hardness of all samples [38,39]

	HV (kgf/mm ²)	Porosity (%)
YSZ	12.1	18.44
CYSZ	9.5	14.24
YSZ-N	6.2	9.61
C-YN	6.9	11.92*

*average value of YSZ-N and C-YN

Figure 9 shows the change of the effect of applying different loads on the sample surface. In case the indenter is placed inside the material, plastic and elastic deformations will happen and after exiting the indenter, the elastic deformation will be removed (Figure 10).

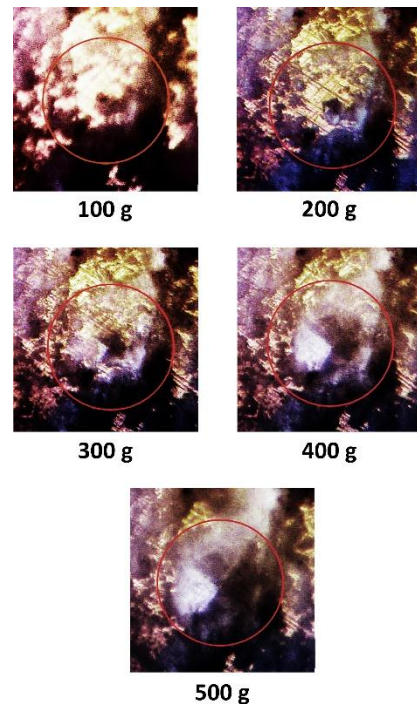


Figure 9. Changing the effect of the indenter by increasing the load

Due to the structural defects, the created notch is not

exactly symmetrical, and its dimensions are slightly different.

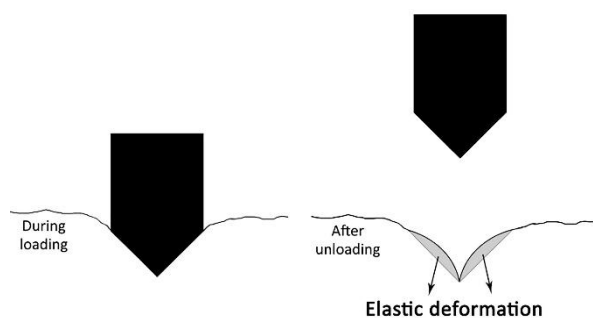


Figure 10. Schematic representation of elastic and plastic deformations during the nanoindentation process

In the ceramic samples, due to the brittleness and complexity of making the tensile test sample, it is practically difficult to measure the elastic modulus by the conventional methods; therefore, alternative methods such as the nanoindentation test are used. For this purpose, followed by applying a load and creating a notch in the material and then removing the load and checking the final notch, the elastic modulus can be determined. Table 5 presents the test results during loading and unloading. Figure 11 illustrates the graph of four tested samples. According to the obtained results and calculation of the elastic modulus based on the theoretical background relations, the reduced and elastic moduli of the samples are given in Table 6.

Table 5. Changing the depth of the notch during the loading and unloading stages

P (g)	YSZ		CYSZ			YSZ-N			C-YN		
	h (μm)		P	h (μm)		P	h (μm)		P	h (μm)	
	L*	UL**		L	UL		L	UL		L	UL
0	0	6.9	0	0	8.1	0	0	9.5	0	0	9.2
100	2.5	8.4	100	2.8	9.3	100	3.5	11.4	100	3.3	10.6
200	5.1	9.1	200	5.4	10	200	6.6	12.6	200	6.3	11.6
300	7.1	9.7	300	7.4	10.5	300	9.3	13.4	300	8.8	12.2
400	8.6	10.1	400	9.2	10.9	400	11.7	13.9	400	10.8	12.8
500	10.1	10.4	500	11	11.2	500	13.6	14.1	500	12.7	13.1
500	10.4		500	11.2		500	14.1		500	13.1	

*: Loading **:Unloading

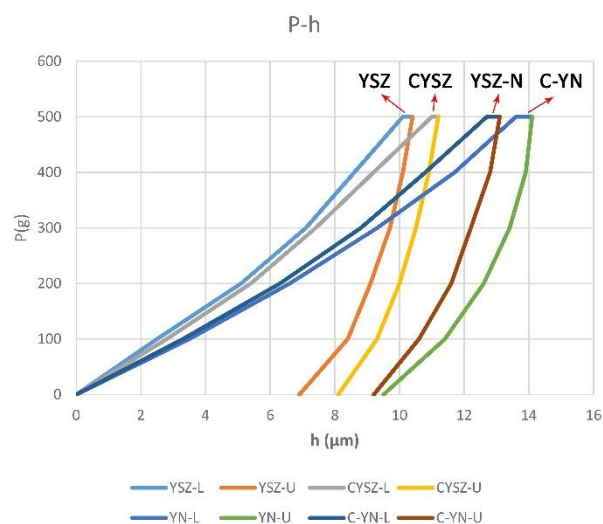


Figure 11. Loading and unloading curve

Table 6. Reduced elastic modulus (E_r) and elastic modulus (E)

	YSZ	CYSZ	YSZ-N	C-YN
E_r (GPa)	122.3	104.2	133.2	91.7
E (GPa)	130.3	107.4	143.5	94

On the one hand, there is a nanostructured layer with proper distribution and nano zones, which shows extraordinary characteristics. On the other hand, there is a CYSZ layer with a denser structure and more structural cracks. Despite the lowest L_2 length of CYSZ (a region where under a constant load, h advances slightly) in the graphs illustrated in Figure 11, the nanostructured and composite samples have the highest L_2 . In the nanostructure sample, the nano zones provide the context for more deformation in this area due to the structural order and integrity as well as lack of obstacles to deformation. In the composite sample, the presence of the layer boundary causes deformation because the layer boundary has less structural integrity, hence vulnerable to loads.

Based on the results, nano-structuring of YSZ enhances the elastic modulus up to about 10%. Of note, the double-layer structure has a much lower modulus due to its layered structure and difference in the properties of the two layers. The calculated results are comparable with other references that are mainly in the range of 50 GPa-250 GPa [40-45].

The XRD test results reveal that the monoclinic zirconia phase is presented in all samples before spraying.

After deposition, this phase disappears, and only a limited amount in YSZ will remain due to its transformation into a non-convertible tetragonal phase.

In YSZ, the wide peaks are attributed to the incorporation of some Zirconium Oxide (c) and Yttrium Zirconium Oxide (t) peaks near each other.

According to the Rietveld analysis, the most important phase of the YSZ is tetragonal Yttrium Zirconium Oxide (Figure. 12 and Table 7) formed as a result of the high cooling rate of the molten droplets during deposition. The wide peaks in 2θ about 35° , 60° , 75° , 82° , and 85° is the proof of the formation of tetragonal Yttrium Zirconium Oxide. In YSZ, tetragonal ZrO_2 peaks cannot be identified but cubic ZrO_2 peaks are detected, which the reason is why the number of the peaks of this material is higher than those of other samples.

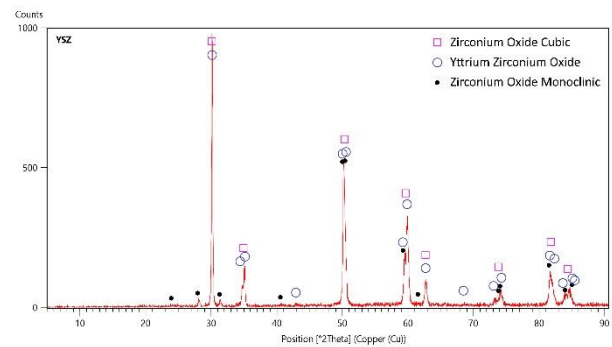


Figure 12. YSZ XRD test results

Table 7. Properties and percentage of phases in XRD results (based on the Rietveld analysis)

	Unit Cell Parameters				Materials			
	Crystal System	a*	c*	c/a	Volume**	YSZ	CYSZ	C-YN
Zirconium Oxide (c)	Cubic	5.175	5.175	1	138.581	30.8 %	16.5 %	21.8 %
Zirconium Oxide (t)	Tetragonal	3.641	5.218	1.433	69.189	-	81.5 %	27.8 %
Zirconium Oxide (m)	Monoclinic	5.210	5.370	1.03	145.16	0.7 %	-	-
Yttrium Zirconium Oxide	Tetragonal	3.613	5.162	1.429	67.482	68.5 %	0.4 %	47 %
Cerium	Cubic	5.161	5.161	1	137.468	-	1.6 %	3.4 %

*: 10^2 pm

** : 10^6 pm³

Both CYSZ and C-YN contain a small amount of Cerium with a cubic structure because the weight percentage of CeO_2 decreases due to its vaporization in the plasma area. In addition, the tetragonal phases in these samples do not have any shift because their unit cell volume is much smaller (about half) than that of other phases. In the presence of Ce, cubic ZrO_2 has a left phase shift in smaller 2θ and a right shift in greater 2θ resulting from the residual stress during deposition and rapid cooling. The main phase of the CYSZ is ZrO_2 (t) (Figure. 13), and its intensity is less than that of other phases with the highest number of peaks. YSZ sample contains only cubic zirconia but the samples containing CYSZ contain tetragonal ZrO_2 peaks due to the stability of the phases with CeO_2 . In CYSZ, a slight phase transition from monoclinic to tetragonal increases the thermal shock resistance. The main crystal system of all samples is tetragonal while the cubic ZrO_2 is still visible (Fig. 14).

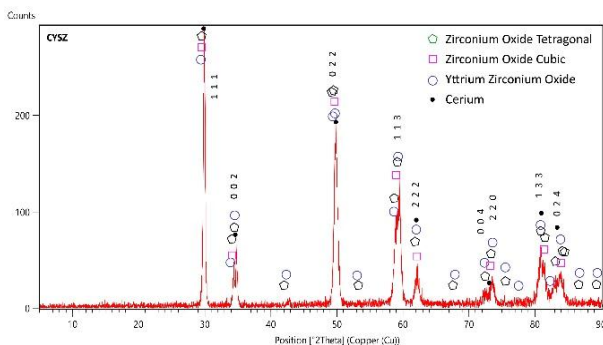


Figure 13. CYSZ XRD test results

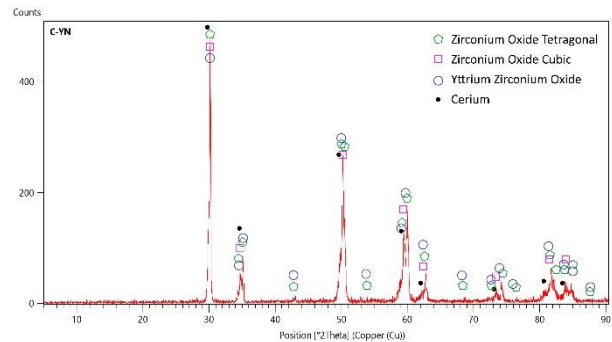


Figure 14. C-YN XRD test results

A comparison of the graphs shows that due to the higher volume fraction of the ZrO_2 (c) phase, the peaks in both YSZ and CYSZ are more intense than those of their counterparts. However, the presence of ZrO_2 (t) causes wider peaks in CYSZ and C-YN and in the CYSZ, where this phase is about 81.5 %, the phases are in a wider state with lower intensity and higher number of peaks.

The results from Raman analysis (Figure 15) confirm the formation of the tetragonal phase in the samples. In this figure, CYSZ, which has the highest degree of tetragonal phase, has the most intense peaks while on the opposite side, YSZ has the least intense peaks. In YSZ and at Raman shift 1000 (Cm^{-1}), a wide peak is observed, confirming the higher percentage of cubic structure in this material; however, this peak is very weak in other samples.

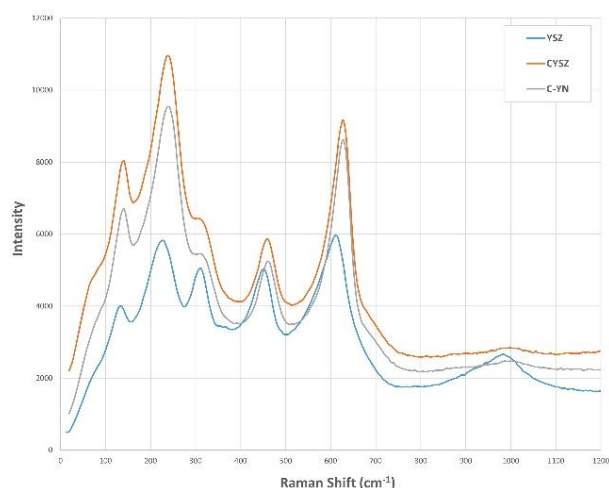


Figure 15. Raman spectroscopy results

4. CONCLUSION

Ceramic nozzles, in many cases, do not bear mechanical loads and are only responsible for controlling the flow. They do not need a metallic substrate and therefore, they can be used separately. In this study, YSZ conical nozzle is considered as the base sample for which three alternatives are designed. CYSZ is cheaper than its counterparts and is characterized by some properties such as better shock resistance. Nanostructured YSZ exhibits improved performance due to its more uniform structure and presence of nano zones, and the double-layer composite sample provides a combination of the aforementioned properties. These four samples were created through the PSF method, and their elastic modulus and hardness were determined using nanoindentation. The results showed that the nanostructured YSZ had the lowest hardness and highest elastic modulus. On the contrary, the composite sample had the lowest elastic modulus, and the YSZ sample had the highest degree of hardness.

ACKNOWLEDGEMENT

The authors thank Mapna Turbine Blade Eng. & Mfg. co. PARTO for cooperation in experimental fields.

REFERENCES

- De la Roche, J., Alvarado-Orozco, J. M., Gomez, P. A., Cano, I. G., Dosta, S., Toro, A., "Hot corrosion behaviour of dense CYSZ/YSZ bilayer coatings deposited by atmospheric plasma spray in $\text{Na}_2\text{SO}_4 + \text{V}_2\text{O}_5$ molten salts", *Surface and Coatings Technology*, Vol. 432, (2022), 128066. <https://doi.org/10.1016/j.surfcoat.2021.128066>
- Bhandari, S., Chakravarthy, Y., Misra, V. C., Tiwari, N., Lenka, R. K., Patro, P. K., Kaity, S., Satpati, S. K., Mahata, T., Ghorui, S., "Investigating Atmospheric Pressure Plasma Spray Coating of YPO_4 and its Performance as a Corrosion Barrier Protective Layer Against Molten Uranium", *Journal of Thermal Spray Technology*, Vol. 31, No. 5, (2022), 1568-1580. <https://doi.org/10.1007/s11666-022-01367-3>
- Sivaramapandian, J., Ananth, M. P., Selvabharathi, R., "Influence of plasma spray WCCrCNi coating and shot peening on surface properties and corrosion behaviour of AZ31 Mg alloy", *Journal of Materials Research and Technology*, Vol. 19, (2022), 3189-3200. <https://doi.org/10.1016/j.jmrt.2022.05.183>
- Fang, J. C., Xu, W. J., "Plasma spray forming", *Journal of Materials Processing Technology*, Vol. 129, No. 1-3, (2002), 288-293. [https://doi.org/10.1016/S0924-0136\(02\)00667-2](https://doi.org/10.1016/S0924-0136(02)00667-2)
- Li, X., Bhushan, B., "A review of nanoindentation continuous stiffness measurement technique and its applications", *Materials Characterization*, Vol. 48, No. 1, (2002), 11-36. [https://doi.org/10.1016/S1044-5803\(02\)00192-4](https://doi.org/10.1016/S1044-5803(02)00192-4)
- Wang, W., Yao, P., Wang, J., Huang, C., Zhu, H., Zou, B., Liu, H., Yan, J., "Crack-free ductile mode grinding of fused silica under controllable dry grinding conditions", *International Journal of Machine Tools and Manufacture*, Vol. 109, (2016), 126-136. <https://doi.org/10.1016/j.ijmactools.2016.07.007>
- Zhang, Z., Yao, P., Wang, J., Huang, C., Cai, R., Zhu, H., "Analytical modelling of surface roughness in precision grinding of particle reinforced metal matrix composites considering nanomechanical response of material", *International Journal of Mechanical Sciences*, Vol. 157-158, (2019), 243-253. <https://doi.org/10.1016/j.ijmecs.2019.04.047>
- Li, X., Bhushan, B., "Dynamic mechanical characterization of magnetic tapes using nanoindentation techniques", *IEEE Transactions on Magnetics*, Vol. 37, No. 4, (2001), 1616-1619. <https://doi.org/10.1109/20.950917>
- Casellas, D., Caro, J., Molas, S., Prado, J. M., Valls, I., "Fracture toughness of carbides in tool steels evaluated by nanoindentation", *Acta Materialia*, Vol. 55, No. 13, (2007), 4277-4286. <https://doi.org/10.1016/j.actamat.2007.03.028>
- Nayebi, B., Parvin, N., Shahedi Asl, M., Motallebzadeh, A., Shokouhimehr, M., "Nanostructural and nanoindentation characterization of ZrB_2 ceramics toughened with in-situ synthesized ZrC ", *International Journal of Refractory Metals and Hard Materials*, Vol. 94, (2021), 105391. <https://doi.org/10.1016/j.ijrmhm.2020.105391>
- Odegard, G. M., Gates, T. S., Herring, H. M., "Characterization of viscoelastic properties of polymeric materials through nanoindentation", *Experimental Mechanics*, Vol. 45, (2005), 130-136. <https://doi.org/10.1007/BF02428185>
- Gregory, J. R., Spearing, S. M., "Nanoindentation of neat and in situ polymers in polymer-matrix composites", *Composites Science and Technology*, Vol. 65, No. 3-4, (2005), 595-607. <https://doi.org/10.1016/j.compscitech.2004.09.001>
- Daphalapurkar, N. P., Dai, C., Gan, R. Z., Lu, H., "Characterization of the linearly viscoelastic behavior of human tympanic membrane by nanoindentation", *Journal of the Mechanical Behavior of Biomedical Materials*, Vol. 2, No. 1, (2009), 82-92. <https://doi.org/10.1016/j.jmbbm.2008.05.008>
- Gaillard, Y., Anglada, M., Jiménez-Piqué, E., "Nanoindentation of yttria-doped zirconia: Effect of crystallographic structure on deformation mechanisms", *Journal of Materials Research*, Vol. 24, No. 3, (2009), 719-727. <https://doi.org/10.1557/jmr.2009.0091>
- Cuadrado, N., Seuba, J., Casellas, D., Anglada, M., Jiménez-Piqué, E., "Geometry of nanoindentation cube-corner cracks observed by FIB tomography: Implication for fracture resistance estimation", *Journal of the European Ceramic Society*, Vol. 35, No. 10, (2015), 2949-2955. <https://doi.org/10.1016/j.jeurceramsoc.2015.03.031>

16. Pathak, S., Kalidindi, S. R., "Spherical nanoindentation stress-strain curves", *Materials Science and Engineering: R: Reports*, Vol. 91, (2015), 1-36. <https://doi.org/10.1016/j.msere.2015.02.001>
17. Fujikane, M., Setoyama, D., Nagao, S., Nowak, R., Yamanaka, S., "Nanoindentation examination of yttria-stabilized zirconia (YSZ) crystal", *Journal of Alloys and Compounds*, Vol. 431, No. 1-2, (2007), 250-255. <https://doi.org/10.1016/j.jallcom.2006.05.058>
18. Campo, M., Ureña, A., Rams, J., "Effect of silica coatings on interfacial mechanical properties in aluminium—SiC composites characterized by nanoindentation", *Scripta Materialia*, Vol. 52, No. 10, (2005), 977-982. <https://doi.org/10.1016/j.scriptamat.2005.01.036>
19. Ulm, F. J., Abousleiman, Y., "The nanogranular nature of shale", *Acta Geotechnica*, Vol. 1, (2006), 77-88. <https://doi.org/10.1007/s11440-006-0009-5>
20. Dadfar, M. R., Rahimipour, M. R., Vaezi, M., Gholamzadeh, A., "Characterization and Phase Transformation of Spherical YSZ Powders Fabricated Via air Plasma Spray Method", *Advanced Ceramics Progress*, Vol. 2, No. 4, (2016), 32-38. <https://doi.org/10.30501/acp.2016.70034>
21. Lu, H., Huang, G., Wang, B., Mamedov, A., Gupta, S., "Characterization of the linear viscoelastic behavior of single-wall carbon nanotube/polyelectrolyte multilayer nanocomposite film using nanoindentation", *Thin Solid Films*, Vol. 500, No. 1-2, (2006), 197-202. <https://doi.org/10.1016/j.tsf.2005.11.051>
22. Saraev, D., Miller, R. E., "Atomic-scale simulations of nanoindentation-induced plasticity in copper crystals with nanometer-sized nickel coatings", *Acta Materialia*, Vol. 54, No. 1, (2006), 33-45. <https://doi.org/10.1016/j.actamat.2005.08.030>
23. Huang, G., Daphalapurkar, N. P., Gan, R. Z., Lu, H., "A method for measuring linearly viscoelastic properties of human tympanic membrane using nanoindentation", *Journal of Biomechanical Engineering*, Vol. 130, No. 1, (2008), 014501. <https://doi.org/10.1115/1.2838034>
24. Guicciardi, S., Melandri, C., Silvestroni, L., Sciti, D., "Indentation grid analysis of nanoindentation bulk and in situ properties of ceramic phases", *Journal of Materials Science*, Vol. 43, (2008), 4348-4352. <https://doi.org/10.1007/s10853-008-2657-3>
25. Botero, C. A., Jiménez-Piqué, E., Baudín, C., Salán, N., Llanes, L., "Nanoindentation of Al₂O₃/Al₂TiO₅ composites: Small-scale mechanical properties of Al₂TiO₅ as reinforcement phase", *Journal of the European Ceramic Society*, Vol. 32, No. 14, (2012), 3723-3731. <https://doi.org/10.1016/j.jeurceramsoc.2012.05.034>
26. Silva, A. P., Booth, F., Garrido, L., Aglietti, E., Pena, P., Baudín, C., "Young's modulus and hardness of multiphase CaZrO₃-MgO ceramics by micro and nanoindentation", *Journal of the European Ceramic Society*, Vol. 38, No. 4, (2018), 2194-2201. <https://doi.org/10.1016/j.jeurceramsoc.2017.11.007>
27. Bor, B., Giuntini, D., Domènech, B., Swain, M. V., Schneider, G. A., "Nanoindentation-based study of the mechanical behavior of bulk supercrystalline ceramic-organic nanocomposites", *Journal of the European Ceramic Society*, Vol. 39, No. 10, (2019), 3247-3256. <https://doi.org/10.1016/j.jeurceramsoc.2019.03.053>
28. Li, W., Liu, W., Qi, F., Chen, Y., Xing, Z., "Determination of micro-mechanical properties of additive manufactured alumina ceramics by nanoindentation and scratching", *Ceramics International*, Vol. 45, No. 8, (2019), 10612-10618. <https://doi.org/10.1016/j.ceramint.2019.02.128>
29. Szymanski, W., Lipa, S., Fortuniak, W., Chojnowski, J., Pospiech, P., Mizerska, U., Slomkowski, S., Nyczyk-Malinowska, A., Hasik, M., "Silicon oxycarbide (SiOC) ceramic microspheres—Structure and mechanical properties by nanoindentation studies", *Ceramics International*, Vol. 45, No. 9, (2019), 11946-11954. <https://doi.org/10.1016/j.ceramint.2019.03.085>
30. Zhang, Z., Yao, P., Wang, J., Huang, C., Zhu, H., Liu, H., Zou, B., "Nanomechanical characterization of RB-SiC ceramics based on nanoindentation and modelling of the ground surface roughness", *Ceramics International*, Vol. 46, No. 5, (2020), 6243-6253. <https://doi.org/10.1016/j.ceramint.2019.11.094>
31. Nayeypashae, N., Etemadi, E., Mohammad Sadeghi, B., Seyedein, S. H., "Experimental and Numerical Study of the Thermo-Mechanical Behavior of Plasma-Sprayed Gadolinium and Yttria Zirconate-Based Thermal Barrier Coatings", *Advanced Ceramics Progress*, Vol. 7, No. 4, (2021), 36-51. <https://doi.org/10.30501/acp.2022.322563.1078>
32. Zerafati, F., H. Majidian, Nikzad, L., "Dispersion Properties of Nano YSZ Particles in Aqueous Suspensions", *Advanced Ceramics Progress*, Vol. 5, No. 3, (2019), 15-22. <https://doi.org/10.30501/acp.2019.95763>
33. Bahamirian, M., "A Comparative Study on the Phase Stability of ZrO₂-8wt. % Y₂O₃: Nano- and Micro-Particles", *Advanced Ceramics Progress*, Vol. 8, No. 2, (2022), 53-60. <https://doi.org/10.30501/acp.2022.352174.1097>
34. Bahamirian, M., Hadavi, S. M. M., Farvizi, M., Keyvani, A., Rahimipour, M. R., "Thermal Durability of YSZ/Nanostructured Gd₂Zr₂O₇ TBC Undergoing Thermal Cycling", *Oxidation of Metals*, Vol. 92, (2019), 401-421. <https://doi.org/10.1007/s11085-019-09937-7>
35. Leitner, A., Maier-Kiener, V., Kiener, D., "Extraction of flow behavior and Hall-Petch parameters using a nanoindentation multiple sharp tip approach", *Advanced Engineering Materials*, Vol. 19, No. 4, (2017), 1600669. <https://doi.org/10.1002/adem.201600669>
36. Oliver, W. C., Pharr, G. M., "Measurement of hardness and elastic modulus by instrumented indentation: Advances in understanding and refinements to methodology", *Journal of Materials Research*, Vol. 19, No. 1, (2004), 3-20. <https://doi.org/10.1557/jmr.2004.19.1.3>
37. Goudarzi, Z. M., Valefi, Z., Zamani, P., Taghi-Ramezani, S., "Comparative investigation of the effect of composition and porosity gradient on thermo-mechanical properties of functionally graded thick thermal barrier coatings deposited by atmospheric plasma spraying", *Ceramics International*, Vol. 48, No. 19, (2022), 28800-28814. <https://doi.org/10.1016/j.ceramint.2021.12.307>
38. Ashofteh, A., Mashhadi, M. M., Amadeh, A., Seifollahpour, S., "Effect of layer thickness on thermal shock behavior in double-layer micro- and nano-structured ceramic top coat APS TBCs", *Ceramics International*, Vol. 43, No. 16, (2017), 13547-13559. <https://doi.org/10.1016/j.ceramint.2017.07.061>
39. Ashofteh, A., Mashhadi, M. M., Amadeh, A., "Thermal shock behavior of multilayer and functionally graded micro- and nano-structured topcoat APS TBCs", *Ceramics International*, Vol. 44, No. 2, (2018), 1951-1963. <https://doi.org/10.1016/j.ceramint.2017.10.138>
40. Łatka, L., Cattini, A., Chicot, D., Pawłowski, L., Kozerski, S., Petit, F., Denoirjean, A., "Mechanical properties of yttria-and ceria-stabilized zirconia coatings obtained by suspension plasma spraying", *Journal of Thermal Spray Technology*, Vol. 22, (2013), 125-130. <https://doi.org/10.1007/s11666-012-9874-7>
41. Adams, J. W., Ruh, R., Mazdiyasi, K. S., "Young's modulus, flexural strength, and fracture of yttria-stabilized zirconia versus temperature", *Journal of the American Ceramic Society*, Vol. 80, No. 4, (1997), 903-908. <https://doi.org/10.1111/j.1151-2916.1997.tb02920.x>
42. Okazaki, M., "Effect of microstructure on elastic modulus of YSZ thermal barrier coatings", *Journal of the Society of Materials Science, Japan*, Vol. 57, No. 11, (2008), 1121-1131. <https://doi.org/10.2472/jms.57.1121>
43. Jin, L., Yu, Q., Rauf, A., Zhou, C., "Elastic, electronic and thermal properties of YSZ from first principles", *Solid State Sciences*, Vol. 14, No. 1, (2012), 106-110. <https://doi.org/10.1016/j.solidstatesciences.2011.11.003>

44. Shimonosono, T., Ueno, T., Hirata, Y., "Mechanical and thermal properties of porous yttria-stabilized zirconia", *Journal of Asian Ceramic Societies*, Vol. 7, No. 1, (2019), 20-30. <https://doi.org/10.1080/21870764.2018.1547248>
45. Gadag, S., Subbarayan, G., Barker, W., "Thermo-elastic properties of dense YSZ and porous Ni-ZrO₂ monolithic and isotropic materials", *Journal of Materials Science*, Vol. 41, (2006), 1221-1232. <https://doi.org/10.1007/s10853-005-3660-6>



Materials and Energy Research Center

MERC

Contents lists available at ACERP

Advanced Ceramics Progress

Journal Homepage: www.acerp.ir

Advanced Ceramics Progress

Original Research Article

Investigating the Phenomenon of Flutter as well as the Mechanical and Microstructural Properties of Layered Composite of Aluminum Sheet with An Epoxy Matrix Reinforced with Carbon Fibers

Kaveh Kolahgar Azari ^a, Amir Hossein Sayadi Kelemi ^b, Ali Alizadeh ^{c,*}, Hamid Omidvar ^d^a PhD Candidate, Composite Engineering Institute, Malek Ashtar University of Technology, Tehran, Tehran, Iran^b MSc Student, Department of Materials Science and Engineering, Sharif University of Technology, Tehran, Tehran, Iran^c Associate Professor, Composite Engineering Institute, Malek Ashtar University of Technology, Tehran, Tehran, Iran^d Associate Professor, Department of Materials and Metallurgical Engineering, Amirkabir University of Technology, Tehran, Tehran, Iran* Corresponding Author Email: alizadehh53@gmail.com (A. Alizadeh)URL: https://www.acerp.ir/article_172522.html

ARTICLE INFO

ABSTRACT

Article History:

Received 03 March 2023
 Received in revised form 29 May 2023
 Accepted 12 June 2023

Keywords:

Fiber Metal Laminates
 Carbon Fibers
 Surface Treatment
 Flutter In Composites

Flutter is an example of an aero-elastic phenomena that involves analyzing the interaction between elastic and aerodynamic forces, both static and dynamic. This study examined the effects of the stacking of polymer and aluminum layers on the modal frequency, drop weight impact, and tensile characteristics of polymeric composites and Fiber Metal Laminates (FMLs) incorporating carbon fibers. In this study, Carbon Fiber Reinforced Plastic (CFRP) laminates were used in the FML composite specimen. Based on a hand-lay-up method, 20 layers of carbon fiber prepregs were used to fabricate the specimen, i.e., Al/4CFRP/Al (Al2C1) and then, Al/4CFRP/Al/4CFRP/Al (Al3C2) fiber metal laminates with two stacking arrangements were made. The surfaces of the aluminum sheets were treated through an anodizing method to improve the adhesion between aluminum and polymer layers. The fracture surface of the specimen was investigated using Optical Microscopy (OM) and Scanning Electron Microscopy (SEM). The mechanical properties along with the vibration behavior of specimen were also studied accordingly. The results showed that Al3C2 had the greatest values of the required frequency for vibration and lowest stress brought on by vibration, with 0.0008 MPa for the initial state. Additionally, the FML sample demonstrated a higher frequency and less stress from vibration than the CFRP specimen with the same thickness. According to the findings of the impact tests, CFRP and Al3C2 had the lowest (210 KJm⁻²) and the highest (960 KJm⁻²) values, respectively. However, due to the lower weight of Al2C1 than that of Al3C2, the specific absorbed energy value of the former was higher (4.7 Jm²kg⁻¹) than that of the latter (2.3 Jm²kg⁻¹). In tensile testing, Al3C2 was characterized by the best tensile properties (i.e., yield strength of 580 MPa and ultimate tensile strength of 897 MPa) compared to other samples. The current study demonstrated that compared to other specimen, Al3C2 possessed the least potential to flutter occurrence in a possible real situation.

<https://doi.org/10.30501/acp.2023.388186.1122>

1. INTRODUCTION

Aerospace, shipbuilding, and automobile industries all

utilize polymer-based composites which are a significant form of composites in general. In recent years, metal sheets have been replaced by polymer composites due to

Please cite this article as: Kolahgar Azari, K., Sayadi Kelemi, A. H., Alizadeh, A., Omidvar, H., "Investigating the Phenomenon of Flutter as well as the Mechanical and Microstructural Properties of Layered Composite of Aluminum Sheet with An Epoxy Matrix Reinforced with Carbon Fibers", *Advanced Ceramics Progress*, Vol. 9, No. 2, (2023), 36-44. <https://doi.org/10.30501/acp.2023.388186.1122>

2423-7485/© 2023 The Author(s). Published by MERC.

This is an open access article under the CC BY license (<https://creativecommons.org/licenses/by/4.0/>).

their great mechanical strength, low cost, and outstanding corrosion and chemical resistance [1]. Fiber Metal Laminates (FMLs) composites are a new kind of polymer-based composites made of sheet metal and fiber-reinforced polymer composites. Various types of FML have been developed to date to reduce the weight of products so as to replace aluminum alloys with the FML composites in automotive and other relative applications [2]. FML composites have facilitated the production of materials with acceptable mechanical and physical properties thanks to their strong impact resistance, convenient repair conditions, high fatigue resistance, low density, and reasonably excellent stiffness [3]. Aluminum, titanium, magnesium, and steel alloys are suitable candidates for the metal layer in FML [3,4]. In addition to its affordable costs in comparison to other choices, aluminum also has good mechanical and chemical qualities [5]. FML composites employ many aluminum alloy grades including 2024 and 7075. The excellent mechanical qualities of these types of alloys such as their high fracture toughness, strong strength, and inexpensive cost have made them a popular and interesting option in a wide range of applications in FML composites [4,6]. To ensure the greatest functioning of the finished components, a strong mechanical link between these layers must be maintained. The mechanical characteristics of the finished composites are improved by a higher degree of adhesion between the layers of the composite and metal sheet.

A number of techniques can be used to improve the adhesion among the composite layers such as providing the mechanical connections (such as bolts and nuts) and using the bonding agents (such as binders), to name a few. It should be noted that the surface modification of aluminum (as metal sheet) is also necessary sometimes and in this regard, surface modification techniques using chemicals, electrochemistry, and mechanics can be useful [2]. Abdullah et al. [7] investigated the composites consisting of woven fibers of glass and polypropylene resin and aluminum sheets under high-speed impact experiments. Based on the test results and an analytical method, they concluded that the energy required to break the specimen in GLARE was higher than that needed for a multi-layer aluminum sheet.

Sadighi et al. [8] investigated the effect of the number and arrangement of fibers and aluminum layers on the FML composite properties. They discovered that the samples with more layers of aluminum exhibited higher impact resistance than those with more layers of polymer. They further evaluated the impact resistance of the multilayer fiber-metal composites made of different metals with various thickness values under low-speed impacts. They discovered that increasing the thickness of the aluminum layer improved the performance of the composite under impact and increased the mass of the layer. Therefore, it can be suitably used in cases that do not require lightweight components only. In the current

work, FML composites with various configurations of aluminum sheets and polymer composites were used to evaluate their vibration, tensile, and impact characteristics and factors controlling these qualities. Another noteworthy advantage of the FMLs is that their mechanical characteristics can be easily modified to meet some particular requirements by altering the direction, thickness, and number of layers in the composite. The components that make up FML each have unique qualities that interact to produce a complicated pattern of the mechanical failure behavior (metal layers are pliable while the composite layers are brittle). Iaccarino et al. [9] found that the bending properties of Carbon Fiber Reinforced Aluminum Laminates (CARALLs) were dependent on the bond between the composite sheet and aluminum layers while the tensile properties were not affected. Poor bonding can reduce the interlayer shear strength by about 10 times.

They also discovered that despite a minor reduction in the strong bonded specimen, the bond strength had no effect on the residual strength of a slit specimen. In order to determine the stress-strain curve, residual strain in relation to a particular stress level, and stress-shear curve, they did some experiments on the FMLs. Based on a comparison between the numerical data and experimental results, they proposed a modified classical lamination model. Although the results did not match their predictions in all cases of failure, they were successful in developing a reasonable model overall.

Dhaliwal and Newaz [10] studied the effect of the position of the metal layers on the stacking materials and then, they produced and tested some CARALL specimens using carbon fiber laminates as the outer layers. The regular CARALL, which featured aluminum laminates as the outer layers, was compared to their laminates and the bending behavior they exhibited, and it was discovered that the former had more strength than the latter.

The impact behavior of the fiber metal sheets has been thoroughly studied in recent years. Abdullah and Cantwell [7] studied the impact behavior of the glass fiber-reinforced polypropylene FML and found that FML offered excellent impact resistance under low-to-high velocity loads. Their findings showed that the FMLs absorbed energy through plastic deformation in aluminum and micro-cracks in composite layers [11].

The improved mechanical characteristics are provided by manufacturing the aluminum-reinforced epoxy composites using the compression molding process. FMLs are hybrid concepts for wind turbines, boats, and marine components in addition to the aerospace sector. Bonding of thin metal sheets to the fiber-reinforced polymer composites without adhesive layers or other adhesive layers forms the basis of the FMLs mainly because the fracture toughness of the metal/composite joint surface increases followed by preparation of a suitable metal surface, such as anodizing and priming

with a corrosion inhibitor. The unique characteristics of the FMLs include fatigue, corrosion, and impact resistance [12]. Layering on the metal or composite surface, however, is crucial that has a detrimental impact on the strength characteristics. The weakest feature of the FMLs is the fracture toughness of a metal/composite contact. The impact and fatigue are two common external stress events that make the metal/composite contact break in the FMLs.

Nazari et al. [13] compared the vibrational properties of the cylindrical FML specimens containing glass fibers and aluminum sheets with epoxy and polymer composites containing glass fibers numerically and experimentally. According to their observations, the amount of natural frequency in all frequency numbers for the FML sample is higher than that of the polymer composite, which is in line with the results obtained in this study.

Khalili et al. [14] carried out torsional vibration test on two samples of polymer composite and FML at different temperatures. They found that the frequency required to vibrate the FML sample at different temperatures was higher than that needed for the polymer composite. They also reported that as the temperature increased, the frequency of both the polymer and FML composite samples increased as well.

The current study aims to investigate the effect of the anodized aluminum sheet on the mechanical properties of the manufactured FML composite specimen. In addition to the mechanical performance, the vibrational behavior of the specimen was studied in order to determine whether or not they were prone to flutter phenomena.

2. MATERIALS AND METHODS

2.1. Materials

In the present study, in order to manufacture the desired FML composites, a particular type of CFRP was used (RC200-carbon pre-impregnated with epoxy resin), with each layer 25 mm thick. Table 1 lists the physical and mechanical properties of carbon pre-coated fabric with epoxy resin.

TABLE 1. Properties of carbon pre-coated fabric with epoxy resin [15]

Properties	Quantity
Coefficient of Thermal Expansion (10^{-6} K^{-1})	2.1
Density (g/cm^3)	1.6
Compressive Strength (MPa)	570
Shear Strength (MPa)	90
Shear Modulus (GPa)	5
Young's Modulus (GPa)	70
Ultimate Tensile Strain (%)	0.85
Ultimate Compressive Strain (%)	0.8

In order to prepare the FML composite metal sheet [16], aluminum sheets with the thickness of 2 mm were used. Then, XRF chemical analysis was done to evaluate the accuracy of the purchased aluminum sheet. Table 2 shows the chemical composition of the purchased aluminum sheets using XRF.

TABLE 2. Chemical composition of aluminum sheets 2024-T3

Element	wt. %
Al	93.954
Cu	3.546
Mg	1.696
Mn	0.437
Si	0.203
Cr	0.119
Ti	0.024
V	0.021

Table 3 shows the physical and mechanical properties of 2024-T3 aluminum. Epoxy resin provides excellent chemical resistance to corrosion against a wide range of organic and inorganic acids [17], alkalis, oxidizing chemicals, and salts and offers good mechanical properties.

TABLE 3. Physical and mechanical properties of 2024-T3 aluminum [18]

Properties	Quantity
Coefficient of Thermal Expansion (10^{-6} K^{-1})	22.6
Density (g/cm^3)	2.78
Thickness (mm)	2
Tensile Strength (MPa)	469
Young's Modulus (GPa)	73.1
Ultimate Tensile Strain (GPa)	0.2

2.2. Electrochemical Preparation of 2024-T3 Aluminum Surface

In the anodizing method, the surface was first placed in a 5.1 % by weight solution of sodium hydroxide at 60 °C for two minutes to remove the weak oxide layer and possible scratches. Then, in order to deoxidize the surface, the sample was placed in an aqueous solution containing a few drops of 66 % by weight nitric acid for five minutes. After preparing the aluminum sheet, the sample was anodized in 3.0 % by weight solution at 55 °C with a constant flow of 7.0 A/dm² for 45 minutes.

2.3. Fabrication of Polymer Composite and FML

In order to determine how the arrangement of the polymer composite and the aluminum sheet would affect the vibration, impact, and tensile characteristics of these composites, the samples were created in accordance with Table 4.

First, a manual layering technique was employed to make all three samples of CFRP, A12C1, and A13C2 and create the composites. The samples were then placed in a

specific mold under 2 kPa of pressure and heated up to 200 °C for baking operations and generating a strong connection between the layers for 40 minutes in order to bake and reach maximum strength.

TABLE 4. Properties of polymer and FML composite samples

Sample Code	Al2024 Layers	CFRP Layers	Lamination
CFRP	0	1	20 layers of carbon fiber pre-impregnated as a polymer composite
Al2C1	2	1	4 layers of carbon fibers with a thickness of 1 mm as a polymer composite in the middle of 2 aluminum sheets with a thickness of 2 mm 2 layers of the polymer composite containing 4 layers of carbon fiber with the thickness of 1 mm among 3 layers of aluminum sheet with the thickness of 2 mm
Al3C2	3	2	

2.4. Mechanical Testing

Dynamic vibration, impact, and static tensile tests with the reliability coefficient of 3 for each sample were done as the related mechanical tests in this study. A changing excitation point and an accelerometer were taken into consideration on a fixed location during the vibration test. Signals for stimulation and reaction were measured and delivered to the two channels installed on the analyzer. The frequency response function was determined by eye examination in accordance with the resonance peaks in the frequency response on the analyzer monitor. Based on the Hounsfield H25KS traction device and the 3039D standard, the tensile behavior of the samples was examined. A force-displacement diagram was obtained as a result of the tensile test, which was carried out at the loading speed of 5 mm/min.

The impact device (manufactured by Iran University of Science and Technology) and the standard 7136ASTM D were utilized to investigate the impact properties of the manufactured samples. The square-shaped specimen as the target was 10×10 cm² in size, which was hit by a steel sphere with the mass of 5.9 kg and a tip which was hemispherical in shape with the diameter of 1 cm falling from a height of 47 cm at the speed of 3 m/s. Another set of samples were subjected to a single shear stress test using a Hounsfield H25KS machine and the ASTM D 1002-01 [13] standard. The samples were loaded at the strain rate of 2 mm/min. Shear-displacement data was recorded on a computer connected to the test device, and the force was divided by the initial area of the joint to calculate the shear stress. It should be mentioned that each test was carried out on the comparable samples at least three times in order to

demonstrate the repeatability of the results, and the final results are an average of the output data.

2.5. Microscopic Studies

Meiji Techno IM 7200 light microscope was used to investigate the joint chapter as well as the failure interface of the composite samples and study the failure mechanism. Scanning Electron Microscopy (SEM) of VEGA\TESCAN-LMU model was also used to study the surface of the modified aluminum and fracture interface of the samples.

3. RESULTS AND DISCUSSION

3.1. Assessing the Aluminum Sheet's Surface Condition

In order to assess the effect of surface treatment, a SEM microscope was utilized. The microscopic pictures of the aluminum surface before (a) and after (b) surface modification are shown in Figure 1.

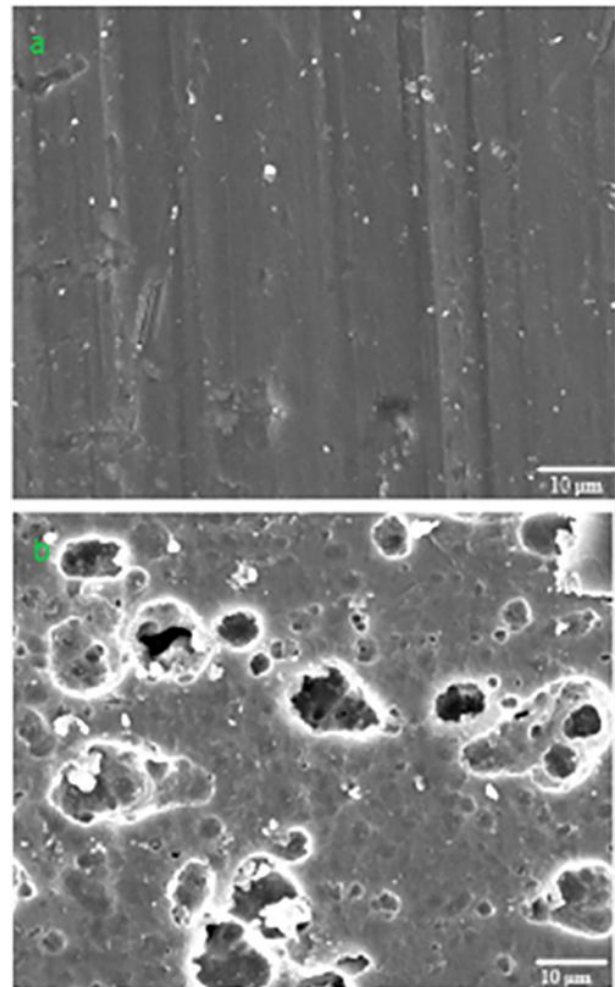


Figure 1. Microscopic image of a) the unmodified aluminum surface and b) anodized aluminum surface

Surface modification increases the specific contact surface between the aluminum and polymer, creates cavities on the aluminum surface where the polymer easily penetrates, makes a mechanical bonding between the composite of aluminum and polymer, and enhances the adhesion of the epoxy layer to the aluminum surface. The mechanical qualities would probably be better owing to the improvement in the load transmission between the layers.

3.2. Vibration Test Results

Vibration tests were carried out on all three samples CFRP, Al2C1, and Al3C2, and the first five natural frequencies were recorded by the device. Tables 5 and 6 show the frequencies obtained by the vibration test and the stresses obtained from these frequencies for all three samples, respectively.

All three samples, CFRP, Al2C1, and Al3C2, underwent vibration testing, and a device was used to capture the first five natural frequencies. Tables 5 and 6 list the frequencies for each of the three samples that were determined through the vibration test and the stresses determined from these frequencies. In Table 6, the initial frequency of the Al3C2 sample is 257 Hz, which is 110 % and 233 % higher than the frequencies of the Al2C1 and CFRP samples, respectively. The frequency of the Al2C1 sample was 122 Hz at the same frequency, which is 58 % higher than the frequency of the CFRP sample. As a result, less vibration occurs in the desired portion when FML composites are used instead of polymer composites. Additionally, a significant increase in the natural frequency is observed in the Al2C1 sample, compared to the Al3C2 sample. In this regard, the improvement in the vibrational properties can be attributed to an increase in the number of hybrid composite layers.

TABLE 5. The first five frequencies of polymer composite and FML (in Hz, with a tolerance of $\pm 5\%$)

Samples	Mod1	Mod2	Mod3	Mod4	Mod5
CFRP	77	129	154	188	272
Al2C1	122	157	189	249	341
Al3C2	257	322	378	394	443

TABLE 6. Maximum amount of stress equivalent to Von misses in the first five frequencies (in MPa, with a tolerance of $\pm 5\%$)

Samples	Mod1	Mod2	Mod3	Mod4	Mod5
CFRP	0.2245	0.1112	1.12	0.1132	0.0201
Al2C1	0.002	0.0074	0.0014	0.0012	0.0009
Al3C2	0.0008	0.0006	0.0002	0.00009	0.00004

The percentage difference between the fifth frequency of the Al3C2 sample (443 Hz) and the fifth frequencies of the Al2C1 sample and the CFRP sample, respectively, diminishes as the frequencies increased. In general, it can

be concluded that the Al3C2 sample has a higher frequency for all five desirable states than the other two samples, which ultimately lowers the vibration.

According to Table 5, the highest stress from the first frequency for the Al3C2 sample is around 0.0008 MPa, which is 100 % and 60 % lower than the values for the CFRP and Al2C1 samples, respectively. Low stresses lengthen the useful life of the part and boost the number of fatigue cycles, hence less worries about the flutter phenomena in components made from FML composites. It seems that the reduction in the frequency stress results from adding more FML composite layers. Additionally, using FML composites instead of polymer composites reduces the likelihood of fatigue failure because the maximum stress of Al2C1 (0.002 MPa) is nearly 99 % lower than that of CFRP.

Contrary to frequency, the level of stress rises as the number of frequencies grows. The frequency differences between the samples cause an increase in the maximum stress differential. For instance, the Al3C2 sample has a maximum stress of 0.00004 MPa at the fifth frequency, which is 101 and 95 % lower than the maximum stresses of the CFRP and Al2C1 samples, respectively.

3.3. Impact Test Results

The impact test results for the CFRP, Al2C1, and Al3C2 samples are shown in Figure 2. The energy absorption rate for the CFRP sample is 210 KJ/m², which is 300 % less than the 850 KJ/m² for the Al2C1 sample and 350 % less than the 960 KJ/m² for the Al3C2 sample. This might be justified by the metal layers of the Al2C1 and Al3C2 samples. The existence of an additional aluminum layer and its impact on strengthening the entire system account for the difference between the two Al2C1 and Al3C2 samples.

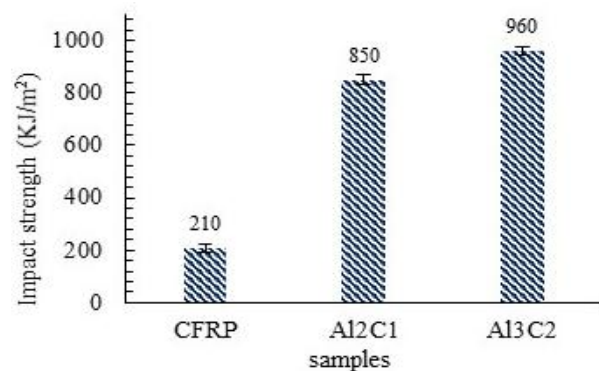


Figure 2. Adsorbed energy in the impact test

The interface of fiber breakdown in the CFRP and Al2C1 samples is depicted in Figure 3. As seen in Figure 3a, debonding of the fibers from the resin results from the failure brought on by impact on the composite sample. Additionally, Optical Microscope images were

taken which are shown in Figure 4. As illustrated in Figure 4a, CFRP sample demonstrated a significant distortion in layers after the impact. Due to the absence of a rigid layer, the structure endured a significant amount of strain prior to failure but showed little delamination. Figure 4b shows debonding of Al2C1 sample after the impact. The force concentration on bonding surface is high, consequently, delamination occurs.

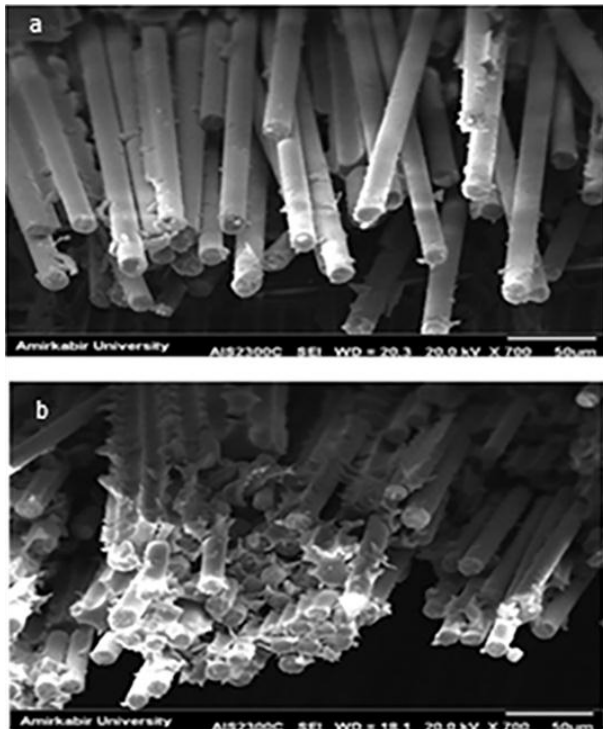


Figure 3. SEM images of the fiber breakdown surface of a) CFRP and b) Al2C1

However, in Figure 3b, the epoxy resin sustains less damage than the CFRP specimen due to the relatively even distribution of the applied load throughout the FML layers. Therefore, the absorbed energy during the impact test is greater for the Al2C1 sample.

Moreover, the FML composites can have an increased amount of plastic deformation prior to any failure. This in turn increases the energy absorption during the impact test. The SEM image (figure 3a) and impact strength diagram (figure 2) demonstrate that the CFRP samples, compared to their Al2C1 and Al3C2 counterparts, have a substantial potential to fail catastrophic. The FML specimen enjoy an improved and effective bonding between the layers of the polymer composite and aluminum sheets. Since the enhanced surface microstructure of aluminum sheet (Figure 1b), the porosity of surface facilitates improved bonding strength between layers in the FML composite.

The reason for the little discrepancy in the quantity of

energy absorbed by the Al2C1 and Al3C2 samples was examined using the force-time diagram. The force-time diagram for the impact test for the Al3C2 and Al2C1 samples is shown in Figure 5. Similar behavior is observed in the diagram up until the A-zone, where it reaches its maximum value. The Al3C2 composite has a maximum applied force of 5840 N, which is 840 N more than the maximum applied force on Al2C1 sample. In contrast to Al2C1, Al3C2 requires more force to reach the maximum zone (A-zone).

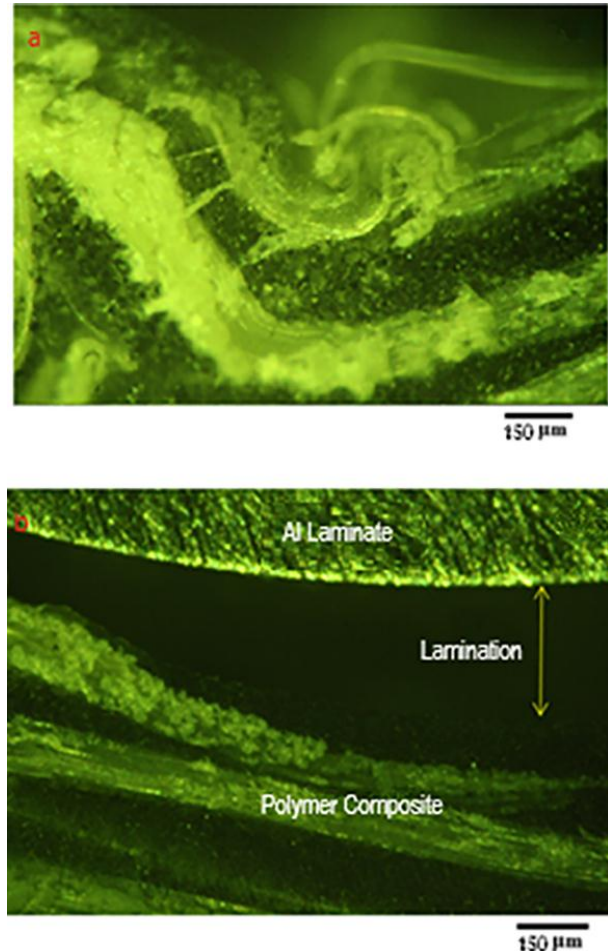


Figure 4. Optical microscope images from side view a) CFRP sample and b) Al2C1 sample after impact test

The graphs climb again to the local maximum value (C-zone) after reaching their maximum value, and this section of the graph (AC) shows how much impact strength is still present in FML. After a significant amount of time, the graph gradually reaches its minimum at the D-zone.

Fan et al. [19] studied the absorbed energy from low velocity impact in three different types of FML composite laminates and three types of polymer composite laminates. They noticed that the sample FMLs had a higher rate of refractive energy absorption than

polymer composites and that the perforation energy increased as the layer thickness increased. Additionally, increasing the composite layer thickness enhanced the impact resistance, which is consistent with the findings of the current study.

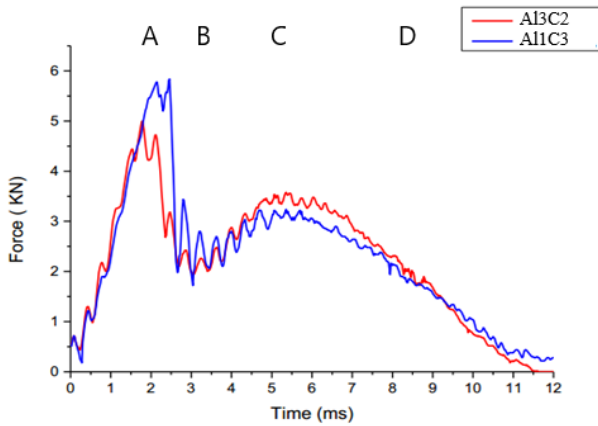


Figure 5. Force-Time diagram of Al3C2 and Al2C1 layered composites.

They further discovered that as the number of layers in the FML samples increased, the rate of refractive energy absorption decreased, primarily as a result of the growing sample weight.

The specific energy absorption quantity is calculated by dividing the weight unit by the energy per unit area. As a result, the composite samples can absorb more energy when their weight and thickness increase. The quantity of specific absorbed energy for the CFRP, Al2C1, and Al3C2 samples is shown in Figure 6.

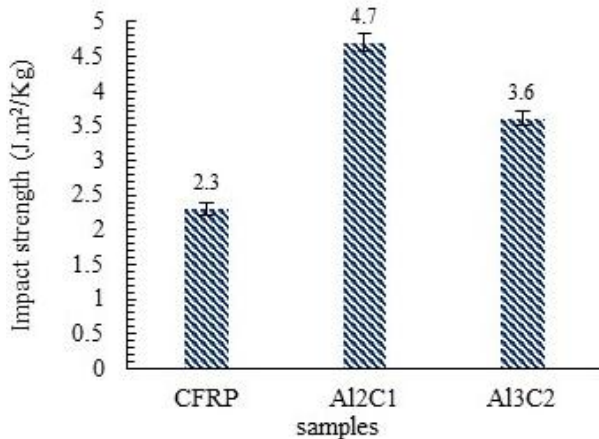


Figure 6. Specific adsorbed energy for 3 samples

According to Figure 6, FML samples have a greater specific energy absorption rate than the polymer composite samples. However, the specific energy

absorption (Jm²/kg) of the Al3C2 sample is about 30 % lower than that of the Al2C1 sample. Therefore, it can be concluded that as the overall weight of the FML composite increases, the amount of specific energy absorbed decreases while increasing the number of layers.

3.4. Tensile Test Results

Table 7 and Figure 7 show the effect of aluminum and polymer composite arrangement on the tensile properties of CFRP, Al2C1, and Al3C2 samples. The yield and final strength values of the Al3C2 sample are 580 and 897 MPa, respectively (Table 7) which is 110 and 150 % greater than those of the CFRP sample (274 and 357 MPa). Additionally, the tensile and yield strength values of the Al2C1 sample are 427 and 653 MPa, respectively, which are 55 and 83 percent higher than those of the CFRP polymer sample. The tensile modulus value of the CFRP sample is 31 GPa, which is 62 % and 71 % lower than those of the Al2C1 (50 GPa) and Al3C2 (53 GPa) samples, respectively.

TABLE 7. Tensile properties of polymer and FML composites (±5 MPa).

Samples	Yield Strength (Mpa)	UltimateTensile Strength (MPa)	Young’s Modulus (GPa)
CFRP	274	357	31
Al2C1	427	653	50
Al3C2	580	897	53

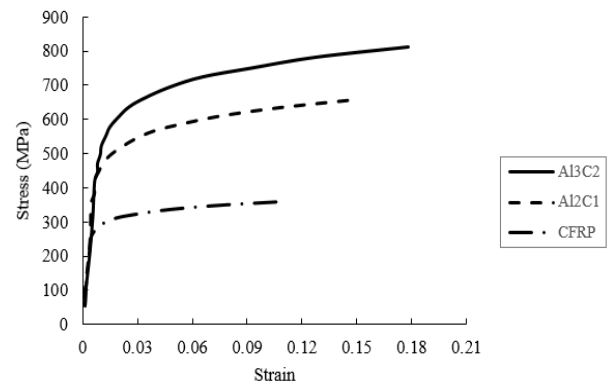


Figure 7. Stress-strain diagram of the tensile test of CFRP, Al2C1, and Al3C2 samples

Increasing the number of aluminum sheets in the FML composite rises the yield strength value from 427 up to 580 MPa in the Al2C1 and Al3C2 samples, respectively. The ultimate tensile strength follows the same pattern and increases from 653 up to 897 MPa in Al2C1 and Al3C2, respectively. Young’s modulus, however, does not follow the previous pattern since the materials are identical in type, hence little difference in the Young’s modulus of the Al2C1 and Al3C2 specimen.

The findings of the tensile test demonstrate that the tensile properties are improved when the polymer composite is converted to the FML version with the same thickness. Additionally, the amount of tensile properties increases upon increasing the thickness or the number of layers of the FML composite.

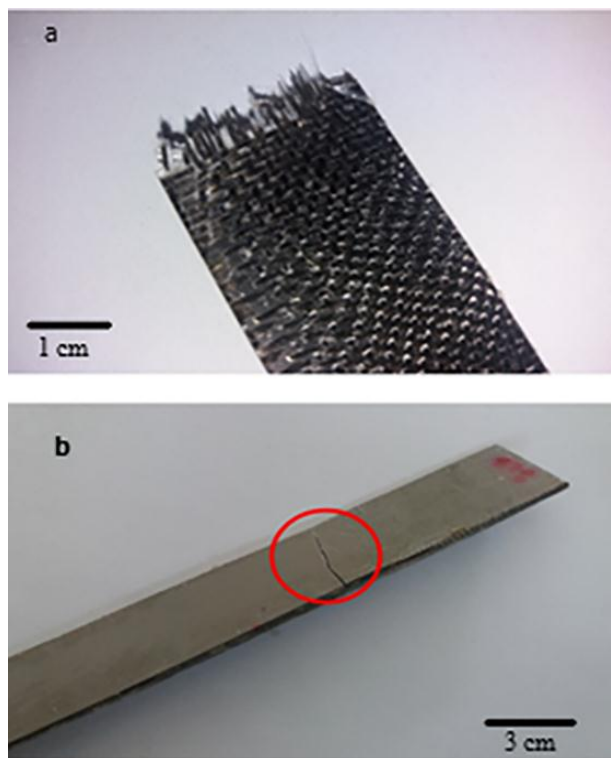


Figure 8. Overall view of fractured sample a) CFRP and b) Al1C2 after tensile test

4. CONCLUSIONS

This study evaluated the effects of 2024-T3 aluminum sheets and carbon fiber-reinforced epoxy composite on the vibration (free vibration), impact, and tensile properties of polymer composite laminates combining the two materials. The following remarks are the final findings of this research:

1. The mechanical properties of the FML composite increased upon increasing the bonding strength between the components of the FML composite as well as the porosity of the surface modification of aluminum sheet through an electrochemical technique (i.e., anodizing).
2. According to the results from the vibration tests, the FML samples required a greater frequency to produce vibration than the polymer composite samples. With an increase in the number of polymer and aluminum layers, the needed frequency and maximum stress in the FML increased due to a decrease in the natural

vibration of the samples.

3. Inclusion of the metal layers in the composite may be the reason why the FML samples absorb more energy than polymer composite samples. The absorbed energy would increase with an increase in the polymer and aluminum layers. The energy absorption rate for the CFRP sample was obtained as 210 KJ/m², 300 % and 350 % less than that of the Al2C1 (850 KJ/m²) and Al3C2 (960 KJ/m²) samples, respectively. Although the specificity of the FML samples is greater than that of the polymer composite samples, the specific energy absorption of the Al3C2 samples (3.6 Jm²kg⁻¹) was about 30 % lower than that of the Al2C1 samples (4.7 Jm²kg⁻¹), hence more layers. The FML composite materials lowered the amount of specific energy absorbed while causing weight growth.
4. Compared to the raw polymer components, making FML composite boosts all tensile parameters including yield and final strength, modulus, and tensile strain. In a similar vein, adding more layers improved the tensile properties of the FML composite. According to the data, the yield and final strength values of the Al3C2 sample were calculated as 580 and 897 MPa, respectively, which are 110 and 150 % greater than those of the CFRP sample (274 and 357 MPa). Finally, the yield and tensile strength values of the Al2C1 sample were 427 and 653 MPa, respectively, 55 % and 83 % greater than those of the sample made of CFRP polymer.

ACKNOWLEDGEMENTS

We would like to express our gratitude to all those who contributed to this research. The experimental studies were jointly done by A. H. Sayadi Kelemi and K. Kolahgar Azari. The project was under the supervision of H. Omidvar and A. Alizadeh, who provided vital comments and led the overall path of the project. The paper was written by A. H. Sayadi, who also did the requested revisions by the journal committee. This project was a collaboration between Sharif University of Technology, Amirkabir University of Technology, and Malek Ashtar University of Technology. We also extend our appreciation to the funding sources that made this research possible, as well as the editing services for their meticulous work in refining our manuscript, and to the administrative staff for their support throughout the project. Without the direct involvement of these individuals and organizations, this research would not have been possible.

REFERENCES

1. Packham, D. E., "The adhesion of polymers to metals: the Role of Surface Topography", In Mittal, K. L. (ed.), *Adhesion Aspects of Polymeric Coatings*, Boston, Springer, (1983), 19-44.

- https://link.springer.com/chapter/10.1007/978-1-4613-3658-7_2
2. Sinmazçelik, T., Avcu, E., Bora, M. Ö., Çoban, O., "A review: Fibre metal laminates, background, bonding types and applied test methods", *Materials & Design*, Vol. 32, No. 7, (2011), 3671-3685. <https://doi.org/10.1016/j.matdes.2011.03.011>
 3. Alderliesten, R., Rans, C., Benedictus, R., "The applicability of magnesium based fibre metal laminates in aerospace structures", *Composites Science and Technology*, Vol. 68, No. 14, (2008), 2983-2993. <https://doi.org/10.1016/j.compscitech.2008.06.017>
 4. Sadighi, M., Alderliesten, R. C., Benedictus, R., "Impact resistance of fiber-metal laminates: A review", *International Journal of Impact Engineering*, Vol. 49, (2012), 77-90. <https://doi.org/10.1016/j.ijimpeng.2012.05.006>
 5. He, W., Wang, L., Liu, H., Wang, C., Yao, L., Li, Q., Sun, G., "On impact behavior of fiber metal laminate (FML) structures: A state-of-the-art review", *Thin-Walled Structures*, Vol. 167, (2021), 108026. <https://doi.org/10.1016/j.tws.2021.108026>
 6. Chai, G. B., Manikandan, P., "Low velocity impact response of fibre-metal laminates - A review", *Composite Structures*, Vol. 107, (2014), 363-381. <https://doi.org/10.1016/j.compstruct.2013.08.003>
 7. Abdullah, M. R., Cantwell, W. J., "The impact resistance of polypropylene-based fibre-metal laminates", *Composites Science and Technology*, Vol. 66, No. 11-12, (2006), 1682-1693. <https://doi.org/10.1016/j.compscitech.2005.11.008>
 8. Sadighi, M., Pärnänen, T., Alderliesten, R. C., Sayeafabi, M., Benedictus, R., "Experimental and numerical investigation of metal type and thickness effects on the impact resistance of fiber metal laminates", *Applied Composite Materials*, Vol. 19, No. 3-4, (2012), 545-559. <https://doi.org/10.1007/s10443-011-9235-6>
 9. Iaccarino, P., Langella, A., Caprino, G., "A simplified model to predict the tensile and shear stress-strain behaviour of fibreglass/aluminium laminates", *Composites Science and Technology*, Vol. 67, No. 9, (2007), 1784-1793. <https://doi.org/10.1016/j.compscitech.2006.11.005>
 10. Dhaliwal, G. S., Newaz, G. M., "Modeling low velocity impact response of carbon fiber reinforced aluminum laminates (CARALL)", *Journal of Dynamic Behavior of Materials*, Vol. 2, No. 2, (2016), 181-193. <https://doi.org/10.1007/s40870-016-0057-3>
 11. Nayak, S. Y., Satish, S. B., Sultan, M. T. H., Kini, C. R., Shenoy, K. R., Samant, R., Sarvade, P. P., Basri, A. A., Mustapha, F., "Influence of fabric orientation and compression factor on the mechanical properties of 3D E-glass reinforced epoxy composites", *Journal of Materials Research and Technology*, Vol. 9, No. 4, (2020), 8517-8527. <https://doi.org/10.1016/j.jmrt.2020.05.111>
 12. Jakubczak, P., Bienias, J., Drożdżel, M., "The collation of impact behaviour of titanium/carbon, aluminum/carbon and conventional carbon fibres laminates", *Thin-Walled Structures*, Vol. 155, (2020), 106952. <https://doi.org/10.1016/j.tws.2020.106952>
 13. Nazari, A., Malekzadeh, K., Naderi, A. A., "Experimental and Numerical Free Vibration Analysis of Hybrid Stiffened Fiber Metal Laminated Circular Cylindrical Shell", *Journal of Solid Mechanics*, Vol. 11, No. 1, (2019), 105-119. <https://doi.org/10.22034/jsm.2019.664223>
 14. Khalili, S. M. R., Daghigh, V., Eslami Farsani, R., "Mechanical behavior of basalt fiber-reinforced and basalt fiber metal laminate composites under tensile and bending loads", *Journal of Reinforced Plastics and Composites*, Vol. 30, No. 8, (2011), 647-659. <https://doi.org/10.1177/0731684411398535>
 15. Patel, K., Potluri, P., Yousaf, Z., Wilkinson, A., "Multi-scale reinforcement of epoxy composites - Use of carbon fibre fabrics coated with an epoxy binder containing MWCNTs for improved interlaminar fracture resistance", *Composites Part B: Engineering*, Vol. 165, (2019), 109-119. <https://doi.org/10.1016/j.compositesb.2018.11.100>
 16. ASTM, *Standard Test Method for Apparent Shear Strength of Single-Lap-Joint Adhesively Bonded Metal Specimens by Tension Loading (Metal-to-Metal)*, ASTM D1002-01, ASTM International, West Conshohocken, PA, USA, (2001). <https://cdn.standards.iteh.ai/samples/3060/82c536f8abe64f3aa72c5592e2110c4a/ASTM-D1002-01.pdf>
 17. Hu, C., Li, T., Yin, H., Hu, L., Tang, J., Ren, K., "Preparation and corrosion protection of three different acids doped polyaniline/epoxy resin composite coatings on carbon steel", *Colloids and Surfaces A: Physicochemical and Engineering Aspects*, Vol. 612, (2021), 126069. <https://doi.org/10.1016/j.colsurfa.2020.126069>
 18. Baucchio, M., *ASM Metals Reference Book*, 3rd Ed., ASM International, Materials Park, OH, USA, (1993). https://www.asminternational.org/asm-metals-reference-book-3rd-edition/results/-/journal_content/56/06118G/PUBLICATION/
 19. Fan, J., Guan, Z. W., Cantwell, W. J., "Numerical modelling of perforation failure in fibre metal laminates subjected to low velocity impact loading", *Composite Structures*, Vol. 93, No. 9, (2011), 2430-2436. <https://doi.org/10.1016/j.compstruct.2011.04.008>



Materials and Energy Research Center

MERC

Contents lists available at [ACERP](#)

Advanced Ceramics Progress

Journal Homepage: www.acerp.ir

Advanced Ceramics Progress

Original Research Article

Characterization and Magnetic Properties of CoFe₂O₄ Nanoparticles Synthesized under Gas Atmosphere: Effect of Ferrofluid Concentration on Hyperthermia Properties

Kamran Heydaryan ^a, Mohammad Almasi Kashi ^{a, b, *}^a PhD, Institute of Nanoscience and Nanotechnology, University of Kashan, Kashan 87317, Iran^b Professor, Department of Physics, University of Kashan, Kashan 87317, Iran* Corresponding Author Email: almac@kashanu.ac.ir (M. Almasi Kashi)URL: https://www.acerp.ir/article_176464.html

ARTICLE INFO

ABSTRACT

Article History:

Received 16 June 2023
 Received in revised form 19 July 2023
 Accepted 30 July 2023

Keywords:

Magnetic Nanoparticles
 CoFe₂O₄
 Superparamagnetic
 Specific Absorption Rate
 Magnetic Hyperthermia
 Gas Atmosphere

Magnetic hyperthermia (MH) is a promising cancer treatment approach that utilizes magnetic nanoparticles with unique properties such as higher penetration depth and precise thermal control that make them effective for cancer treatment. In addition, the sensitivity of cancer cells to heat and role of magnetic nanoparticles proved to be very effective in combined treatments. Here, CoFe₂O₄ nanoparticles are synthesized using a co-precipitation method under gas atmosphere during the synthesis process. The characteristics and properties of the synthesized nanoparticles are investigated using XRD, FESEM, and vibrating sample magnetometer (VSM) analyses. The XRD results confirm the formation of cobalt nanoparticles. The FESEM investigations reveal that nanoparticles have uniform surface morphology and spherical shape. The VSM results show that the CoFe₂O₄ nanoparticles possess superparamagnetic properties as confirmed by FORC analysis. Under the gas atmosphere, saturation magnetization (M_s) and coercivity (H_c) of the CoFe₂O₄ nanoparticles are obtained as 41.5 emu/g and 34.1 Oe, respectively, while these values in the nanoparticles synthesized without the gas atmosphere are calculated as M_s = 33.8 emu/g and H_c = 42.3 Oe. The MH of the CoFe₂O₄ nanoparticles is measured by preparing concentrations of 1, 3, and 5 mg/ml of the nanoparticles under the magnetic field of 400 Oe at the frequency of 400 kHz. The results show that the highest MH is achieved at the concentration of 3 mg/ml, and the specific loss power (SLP) value is measured as 190.3 W/g. Overall, these findings confirm that the co-precipitation method is an effective approach to the synthesis of biocompatible CoFe₂O₄ nanoparticles which is in line with the results from MTT analysis, having desirable properties for various applications, especially for MH.

<https://doi.org/10.30501/acp.2023.402618.1126>

1. INTRODUCTION

Hyperthermia can be classified into several types based on its heat source. Magnetic hyperthermia (MH) is a promising cancer treatment approach that uses magnetic nanoparticles as the sources of heat generation in tumor

tissues [1,2]. It offers several advantages over other treatment modalities that are listed in the following: higher penetration depth of alternating magnetic fields than other mechanisms (e.g., light or ultrasound) that allows access to deeper tissues, use of nanoparticles in a wide range of concentrations and their retention in the

Please cite this article as: Heydaryan, K., Almasi Kashi, M., "Characterization and Magnetic Properties of CoFe₂O₄ Nanoparticles Synthesized under Gas Atmosphere: Effect of Ferrofluid Concentration on Hyperthermia Properties", *Advanced Ceramics Progress*, Vol. 9, No. 2, (2023), 45-52. <https://doi.org/10.30501/acp.2023.402618.1126>

2423-7485/© 2023 The Author(s). Published by MERC.

This is an open access article under the CC BY license (<https://creativecommons.org/licenses/by/4.0/>).

tumor site for repeated treatment sessions, size-dependent magnetic properties that facilitate control and tuning of the heating level, precise control of the nanoparticle size, morphology, and surface modification for different purposes including biocompatibility, ability to provide chemical groups for attaching biological molecules, and minimization of blood protein adsorption. Application of magnetic nanoparticles for hyperthermia cancer therapy is highly promising due to their excellent temperature homogeneity [3-7]. Additionally, they can be simultaneously used in combinatorial therapies. One of these approaches is targeted drug delivery combined with hyperthermia in which the drugs are attached to the surface of nanoparticles as the carriers and delivered to the target tissue [8,9]. A variety of cancer imaging techniques and nano-platforms have been recently used for cancer diagnosis in order to monitor treatment [10,11].

In recent years, different methods have been developed for cancer treatment. These methods are classified into two categories: a) traditional methods such as surgery, chemotherapy, and radiation therapy, and b) advanced methods such as gene therapy, hormone therapy, photodynamic therapy, and hyperthermia therapy (or thermal therapy) [12-14]. In medical science, hyperthermia therapy is referred to as a cancer treatment method in which cancerous tissues are exposed to a temperature increase above the physiological body temperature (37 °C) up to about 6-8 °C. One of the prominent features of the cancer cells, compared to the healthy ones, is their sensitivity and vulnerability to heat, and a temperature increase of more than 6 °C can completely destroy them [15-18]. The sensitivity of the cancer cells to heat results from lack of oxygen caused by poor blood flow in the tumor area. Healthy cells can organize blood flow and dissipate excess heat through the vascular network around them in the convection and diffusion phenomenon while the cancer cells have less ability to expand the vascular network. As a result, blood flow decreases and the tissue becomes overheated (more than 42 °C). In addition, the survival of the tumor cells significantly decreases in the range of 41-47 °C while the healthy cells are hardly affected by this temperature increase [15,16,19].

Due to their small size or high surface area, nanomaterials, especially those with sizes ranging from 1 to 100 nanometers, are characterized by unique optical, electrical, catalytic, thermal, and magnetic properties [20-28]. Magnetic nanoparticles have been used in a wide range of applications because they can be easily separated under an external magnetic field and designed for various purposes such as the advanced material synthesis, magnetic enhancement imaging, and controlled heat imaging [29-31]. Generally, magnetic nanoparticles are composed of magnetic elements such as iron, cobalt, nickel, and their chemical compounds. Among various types of the magnetic nanoparticles, ferrite nanoparticles with superparamagnetic properties

have been frequently referred to as the efficient magnetic nanomaterials that are suitable for various applications [6,31-33]. Ferrite nanoparticles have interesting properties such as non-toxicity, biocompatibility, chemical stability, and high magnetic reversibility [34-37]. Cobalt ferrite nanoparticles have a high potential for targeted drug delivery and MRI and for this reason, they have received considerable attention in recent decades. Owing to their attractive magnetic properties, cobalt ferrite nanoparticles have high potential in MH therapy [31,38-40].

Magnetic nanoparticles can be synthesized by physical and chemical methods among which, the co-precipitation method is one of the cost-effective and simple methods. As a disadvantage, some materials in the synthesis through this method do not have uniform quality. One of the ways to control uniformity and proper morphology in the synthesis based on co-precipitation method is to use argon and hydrogen atmosphere that removes excessive oxygen and impurities during the synthesis [41-44]. However, the significant role of the MH properties of cobalt ferrite nanoparticles synthesized by a co-precipitation method under the gas atmosphere has been still neglected.

In this study, the prepared sample was first converted into a stable nanoparticle suspension with a specific concentration. Then, the sample was placed in a MH measurement device where an alternating magnetic field with a specific intensity and frequency was applied, and the temperature increase of the nanoparticle suspension was measured and recorded for one minute. The value of specific loss power (SLP), which indicates the amount of the MH of the nanoparticles in the presence of the magnetic field, was calculated using Equation (1) In this equation, c represents the specific heat capacity of the solvent, m_{MNP_s} the mass of the magnetic nanoparticles, m_f the mass of the fluid, and $\Delta T/\Delta t$ the initial slope of the temperature-time curve [45].

$$SLP = c \frac{m_f}{m_{MNP_s}} \frac{\Delta T}{\Delta t} \quad (1)$$

2. MATERIALS AND METHODS

2.1. Synthesis of CoFe₂O₄ Nanoparticles

For the synthesis of CoFe₂O₄, 10 ml of 0.5 M FeCl₃.6H₂O and 6 ml of 0.4 M CoCl₂.6H₂O were mixed in a three-necked flask and placed on a temperature-controlled heater mantel. The mixture was then heated to 85 °C under the gas atmosphere (85 % argon + 15 % hydrogen) [46,47]. During the heating process, the pH of the medium reached about 12 by adding NaOH solution drop by drop. The solution was stirred for 60 min at 85 °C and then, the obtained precipitate was cooled down to room

temperature. Finally, the precipitate was washed five times with ethanol and deionized water using a centrifuge. The schematic of the synthesis steps is shown in Figure 1.

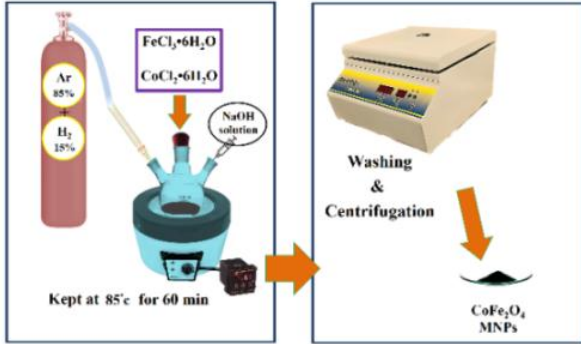


Figure 1. Schematic representation of the preparation process of CoFe_2O_4 nanoparticles using a co-precipitation method under gas atmosphere

2.2. Characterizations

A Field-Emission Scanning Electron Microscope (FESEM, TESCAN, Czech) was used to investigate the morphology of CoFe_2O_4 synthesized with different surfactants. Then, X-Ray Diffraction (XRD; Philips, X'Pert Pro, $\lambda = 0.154 \text{ nm}$) analysis was done to study the crystal structure of the CoFe_2O_4 . The magnetic properties were then investigated at room temperature by measuring the hysteresis curves (applied magnetic field: $\pm 10000 \text{ Oe}$) and doing FORC analysis using a vibrating sample magnetometer (VSM, MDK Co.) equipped with FORC software.

MH value of the CoFe_2O_4 was evaluated by measuring their heating efficiency using an alternating magnetic field with the intensity of 400 Oe at the frequency of 400 kHz . For this purpose, a hyperthermia device (Magnetic DaneshPajoh Kashan Co.) was used. The SLP value of the prepared ferrofluids (containing CoFe_2O_4 nanoparticles with concentrations of 1, 3, and 5 mg/ml in deionized water) was calculated through Equation (1).

3. RESULTS AND DISCUSSION

3.1. XRD Results

The XRD pattern of the synthesized CoFe_2O_4 is shown in Figure 2. In general, the XRD peaks at $2\theta = 18.2^\circ, 29.9^\circ, 35.4^\circ, 36.8^\circ, 42.9^\circ, 53.2^\circ, 56.6^\circ, 62.4^\circ,$ and 73.6° , respectively, can be indexed to (111), (220), (311), (222), (400), (442), (511), (440), and (533) reflections of face-centered cubic CoFe_2O_4 crystal structure (JCPDS card no. 00-002-1045). The absence of other peaks is indicative of the high purity of the synthesized sample. The average crystallite size (d_{cs}) was estimated along the preferential orientation using Scherrer equation [48]:

$$d_{cs} = \frac{K\lambda}{\beta \cos \theta} \quad (2)$$

where K is the shape factor ($K = 0.9$), λ the X-ray wavelength, β (in terms of radian) the full width at half maximum, and θ the diffraction angle. Accordingly, the value of d_{cs} of CoFe_2O_4 was obtained as $d 21.6 \text{ nm}$ [49-54].

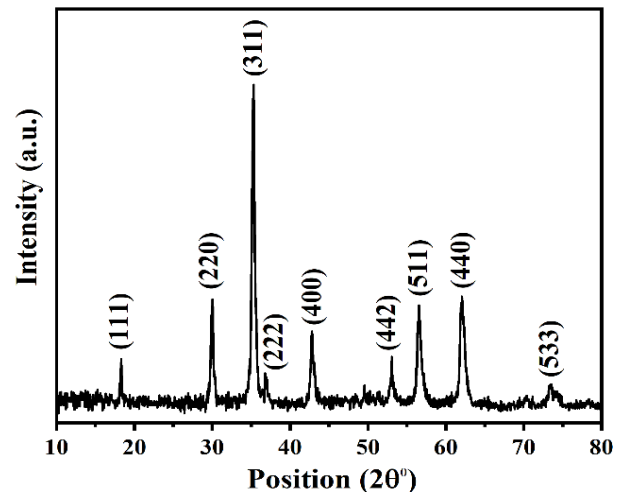


Figure 2. XRD pattern of CoFe_2O_4

3.2. FESEM Results

Figure 3 demonstrates the FESEM image of the CoFe_2O_4 nanoparticles. The synthesized cobalt ferrite nanoparticles have spherical morphology and suitable uniformity, one of the effective factors on the magnetic heat enhancement of magnetic nanoparticles. As observed in the inset of Figure 3, the size distribution of the CoFe_2O_4 nanoparticles was obtained using FESEM images and Digimizer software. The size of the CoFe_2O_4 nanoparticles is in the range of 10 to 38 nm with the average size of 24 nm , indicating the formation of superparamagnetic nanoparticles.

3.3. Hysteresis Curve and FORC Results

The room temperature hysteresis curve of the synthesized CoFe_2O_4 nanoparticles is illustrated in Figure 4. To study the magnetic properties of cobalt ferrite nanoparticles synthesized under gas atmosphere (S1) and without gas atmosphere (S2), a magnetic field in the range of -10 kOe to $+10 \text{ kOe}$ was applied to the samples in order to obtain the magnetic parameters. The saturation magnetization (M_S) and coercivity (H_C) values of the samples S1 and S2 are found to be 41.5 emu/g and 34.1 Oe and 33.8 emu/g and 42.3 Oe , respectively. It is inferred that the gas atmosphere probably prevents the formation of oxide impurities in the cobalt ferrite nanoparticles, thus enhancing M_S value up to about 22% (from 33.8 to 41.5 emu/g). These nanoparticles are considered as superparamagnetic materials due to their

low coercivity. In addition to generating magnetic heat, this property of nanoparticles can also be used to increase the image contrast in the MRI since these nanoparticles do not have any harmful effects on the human body. Figure 4 shows the hysteresis curve of CoFe_2O_4 nanoparticles, which shows the superparamagnetic nature of cobalt ferrite nanoparticles due to its very narrow width (close to zero).

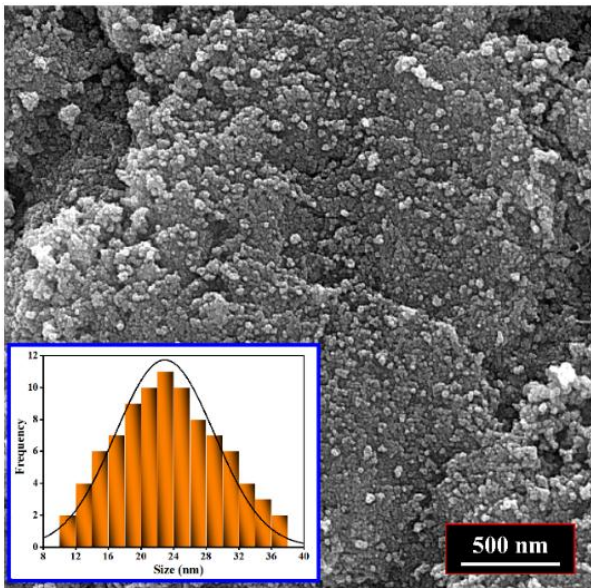


Figure 3. FESEM image of CoFe_2O_4 . The inset represents the corresponding size distribution

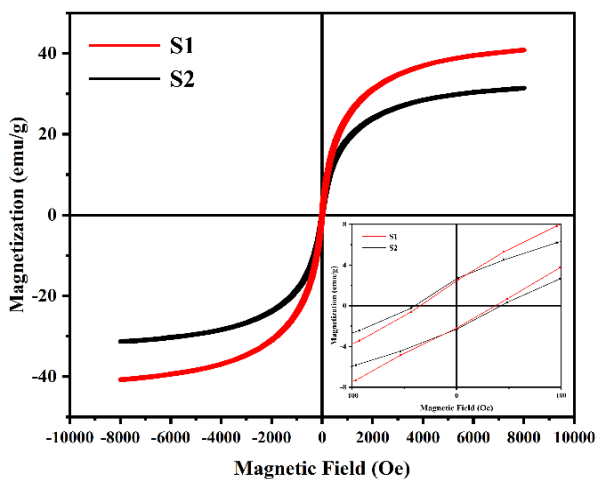


Figure 4. Hysteresis curves of the CoFe_2O_4 nanoparticles synthesized under gas atmosphere (S1) and without gas atmosphere (S2). The inset shows the details of the curves.

The FORC analysis was carried out by initially intensifying the magnetic field (H) applied to the sample up to its saturation field, followed by decreasing it by a

reverse field (H_r). During this process, magnetization $M(H, H_r)$ was measured. Accordingly, sets of FORCs were plotted. The magnetic field ranged from -750 to $+750$ Oe, having a reversal step of 30 Oe. The FORC diagram depicted in Figure 5 shows a coercive field distribution ranging between 0 and 110 Oe. This may also indicate the relatively high contribution of the superparamagnetic CoFe_2O_4 nanoparticles due to their small average diameter. In the FORC diagram, the extent of the coercive field and magnetostatic interactions can be extracted, showing the uniformity and distribution of the nanoparticle size. The mild coercive field distribution around the origin of the graph ($H_c^{\text{FORC}} < 110$ Oe) is attributed to the quasi-superparamagnetic behavior of the nanoparticles [55].

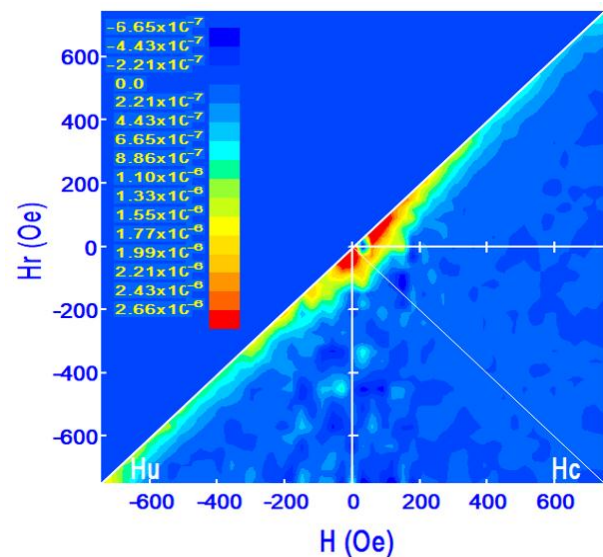


Figure 5. FORC diagram of CoFe_2O_4 nanoparticles

3.4. MH Measurements and MTT Results

In the measurements of the MH which ultimately leads to the calculation of SLP, ferrofluids containing cobalt ferrite nanoparticles with the concentrations of 1, 3, and 5 mg/ml were prepared in aqueous medium. An ultrasonic bath was then used to disperse nanoparticles in water, and the solutions were placed in the bath for 30 min. The hyperthermia properties of the nanoparticles were measured using a MH machine (MDK, Iran). The ferrofluids of the samples were subjected to an alternating magnetic field with the frequency of 400 kHz and field intensity of 400 Oe in the device. Figure 6a shows the ΔT with respect to the time of nanoparticles in a period of 5 min. The SLP values were calculated using Equation 1 by considering the temperature increase value measured in a one-minute period.

Figure 6b shows the amounts of the SLP of the CoFe_2O_4 nanoparticles with the concentrations of 1, 3, and 5 mg/ml, and the highest amount equals 190.3 W/g at the concentration of 3 mg/ml. A comparison of the heat

dissipation power of the samples with different concentrations shows that the decrease in concentration (from 5 to 3 mg/ml) causes an increase in the heat produced by the ferrofluid.

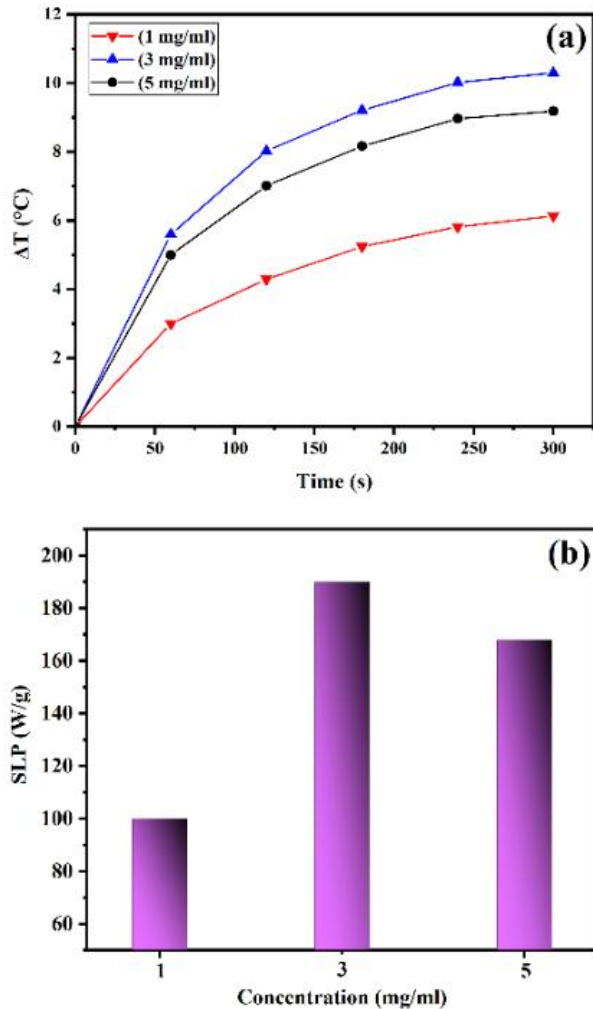


Figure 6. (a) Variation of ΔT with respect to time for ferrofluids of CoFe₂O₄ nanoparticles and (b) different concentrations of ferrofluids (1, 3, and 5 mg/ml)

As the concentration decreases, the amount of nanoparticles dissolved in the solution decreases. Meanwhile, the solution becomes less viscous, and the distance between the nanoparticles increases. This, in turn, lessens the interaction between the nanoparticles, thus making them have less obstacles against their physical rotation in the fluid. As a result, they can convert more amount of the absorbed electromagnetic energy into heat due to their higher and faster rotation movements that eventually increases the SLP. It should be noted that changing the concentration can affect the Brownian relaxation mechanism, which is related to the rotation of nanoparticles. In fact, the Néel mechanism is related to the rotation of the moments inside the

nanoparticles, hence independent of the surrounding environment of the nanoparticles. Finally, at the concentration of 3 mg/ml, the effect of Néel and Brownian mechanisms reaches its optimal state, and the effect of these two mechanisms leads to the highest SLP at this concentration. Other effective factors that determine the SLP value are the characteristics of the measuring device such as the frequency and intensity of the field [56,57].

Figure 7 illustrates the MTT assay results obtained from the CoFe₂O₄ nanoparticles after 24, 48, and 72 h. According to findings, the cell viability of the L929 cells remains high (> 85 %) in the presence of these nanoparticles. Overall, it can be concluded that CoFe₂O₄ nanoparticles with high SLPs do not have a significant cytotoxic effect on the L929 cells, hence suitable for MH therapy.

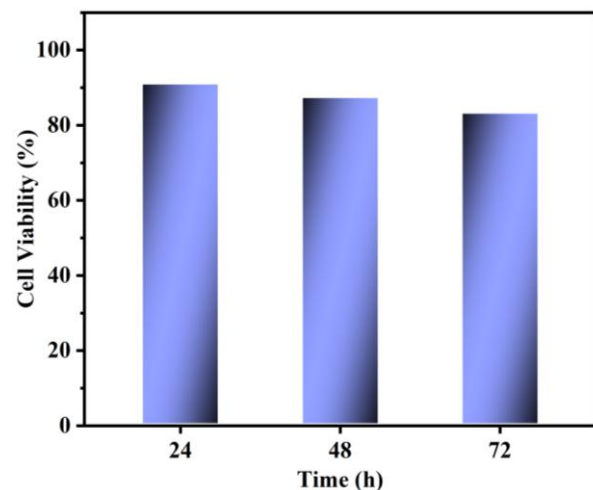


Figure 7. MTT assay results of CoFe₂O₄ nanoparticles for different times

4. CONCLUSION

In conclusion, CoFe₂O₄ nanoparticles were synthesized in this study based on a co-precipitation method under gas atmosphere (85 % argon + 15 % hydrogen). The formation of cobalt nanoparticles was confirmed based on the XRD results. The FESEM investigations showed that the surface morphology of the CoFe₂O₄ nanoparticles was uniform. In addition, according to the FESEM images, the nanoparticles under study had spherical morphology. The results of the hysteresis curve showed that CoFe₂O₄ nanoparticles were superparamagnetic in nature. The gas atmosphere played a constructive role in enhancing the magnetic properties by increasing the M_s value up to about 22 %. Further, the FORC analysis confirmed the superparamagnetic contribution of the nanoparticles. Investigations of the

magnetic heat enhancement at the concentrations of 1, 3, and 5 mg/ml in aqueous medium confirmed that the suitable concentration for the highest SLP was 3 mg/ml for biocompatible cobalt ferrite nanoparticles. The synthesized nanoparticles have a high potential for drug delivery and MRI in future works.

ACKNOWLEDGEMENT

The authors gratefully acknowledge University of Kashan for providing the financial support of this work by Grant No. 159023/89.

REFERENCES

- Zhang, J. Z., Tang, H., Chen, X. Z., Su, Q., Xi, W. S., Liu, Y. Y., Liu, Y., Cao, A., Wang, H., "In vivo fate of Ag₂Te quantum dot and comparison with other NIR-II silver chalcogenide quantum dots", *Journal of Nanoparticle Research*, Vol. 22, No. 9, (2020), 287. <https://doi.org/10.1007/s11051-020-04992-7>
- Ferreira, I. N., Isikawa, M. M., Nunes, L. H. S., Micheletto, M. C., Guidelli, E. J., "Magnetic nanoparticles covered with polycyclic aromatic hydrocarbons as singlet oxygen carriers for combining photodynamic therapy and magnetic hyperthermia", *Journal of Photochemistry and Photobiology A: Chemistry*, Vol. 444, (2023), 114902. <https://doi.org/10.1016/j.jphotochem.2023.114902>
- Myrovali, E., Papadopoulos, K., Charalampous, G., Kesapidou, P., Vourlias, G., Kehagias, T., Angelakeris, M., Wiedwald, U., "Toward the Separation of Different Heating Mechanisms in Magnetic Particle Hyperthermia", *ACS Omega*, Vol. 8, No. 14, (2023), 12955-12967. <https://doi.org/10.1021/acsomega.2c05962>
- Rossi, L. M., Quach, A. D., Rosenzweig, Z., "Glucose oxidase-magnetite nanoparticle bioconjugate for glucose sensing", *Analytical and Bioanalytical Chemistry*, Vol. 380, (2004), 606-613. <https://doi.org/10.1007/s00216-004-2770-3>
- Zheng, Y., He, J., Li, B., Wu, T., Dai, W., Li, Y., "Research on DC protection strategy in multi-terminal hybrid HVDC system", *Engineering*, Vol. 7, No. 8, (2021), 1064-1075. <https://doi.org/10.1016/j.eng.2021.05.002>
- Laurent, S., Forge, D., Port, M., Roch, A., Robic, C., Vander Elst, L., Muller, R. N., "Magnetic iron oxide nanoparticles: synthesis, stabilization, vectorization, physicochemical characterizations, and biological applications", *Chemical Reviews*, Vol. 108, No. 6, (2008), 2064-2110. <https://doi.org/10.1021/cr068445e>
- Heydaryan, K., Mohammadalizadeh, M., Montazer, A. H., Kashi, M. A., "Reaction time-induced improvement in hyperthermia properties of cobalt ferrite nanoparticles with different sizes", *Materials Chemistry and Physics*, Vol. 303, (2023), 127773. <https://doi.org/10.1016/j.matchemphys.2023.127773>
- Esmaili, A., Hemami, R., Ghaffari, Y., Abdollahi, S., "A review on evaluation of natural polymers with the approach of drug delivery system using herbal plant microcapsules", *Journal of Simulation and Analysis of Novel Technologies in Mechanical Engineering*, Vol. 14, No. 2, (2022), 65-77. https://journals.iaui.ir/article_693977_aed449699e5f9b7545209fa6f0af9527.pdf
- Dobson, J., "Magnetic nanoparticles for drug delivery", *Drug Development Research*, Vol. 67, No. 1, (2006), 55-60. <https://doi.org/10.1002/ddr.20067>
- Thorat, N. D., *Advances in Image-Guided Cancer Nanomedicine*, IOP Publishing Ltd, Bristol, UK, (2022). <https://doi.org/10.1088/978-0-7503-3675-8>
- Jadhav, S. A., Somvanshi, S. B., Gawali, S. S., Zakade, K., Jadhav, K. M., "Rare earth-doped mixed Ni-Cu-Zn ferrites as an effective photocatalytic agent for active degradation of Rhodamine B dye", *Journal of Rare Earths*, (2023). <https://doi.org/10.1016/j.jre.2023.03.004>
- Ullah, A., Ullah, N., Nawaz, T., Aziz, T., "Molecular mechanisms of Sanguinarine in cancer prevention and treatment", *Anti-Cancer Agents in Medicinal Chemistry (Formerly Current Medicinal Chemistry-Anti-Cancer Agents)*, Vol. 23, No. 7, (2023), 765-778. <https://doi.org/10.2174/1871520622666220831124321>
- Zhang, J., Wang, S., Zhou, Z., Lei, C., Yu, H., Zeng, C., Xia, X., Qiao, G., Shi, Q., "Unpleasant symptoms of immunotherapy for people with lung cancer: A mixed-method study", *International Journal of Nursing Studies*, Vol. 139, (2023), 104430. <https://doi.org/10.1016/j.ijnurstu.2022.104430>
- Naik, M. M., Vinuth, M., Kumar, V. U., Hemakumar, K. H., Preethi, G., Kumar, M. P., Nagaraju, G., "A facile green synthesis of nickel ferrite nanoparticles using Tamarindus Indica seeds for magnetic and photocatalytic studies", *Nanotechnology for Environmental Engineering*, Vol. 8, No. 1, (2023), 143-151. <https://doi.org/10.1007/s41204-022-00257-x>
- Hishiki, A., Sato, M., Hashimoto, H., "Structure of HIRAN domain of human HLTf bound to duplex DNA provides structural basis for DNA unwinding to initiate replication fork regression", *The journal of biochemistry*, Vol. 167, No. 6, (2020), 597-602. <https://doi.org/10.1093/jb/mvaa008>
- Ahmed, K., Tabuchi, Y., Kondo, T., "Hyperthermia: an effective strategy to induce apoptosis in cancer cells", *Apoptosis*, Vol. 20, (2015), 1411-1419. <https://doi.org/10.1007/s10495-015-1168-3>
- Putri, C. D., Hadi, A. F., Anggraeni, D., Riski, A., "Projection pursuit regression and principal component regression on statistical downscaling using artificial neural network for rainfall prediction in Jember", In *Journal of Physics: Conference Series*, May 2021, IOP Publishing, Vol. 1872, No. 1, (2021), 012023. <https://doi.org/10.1088/1742-6596/1872/1/012023>
- Koroulakis, A., Rice, S. R., DeCesaris, C., Knight, N., Nichols, E. M., "Perceptions and patterns in academic publishing: a survey of United States residents in radiation oncology", *Advances in Radiation Oncology*, Vol. 5, No. 2, (2020), 146-151. <https://doi.org/10.1016/j.adro.2019.09.001>
- Dunne, M., Dou, Y. N., Drake, D. M., Spence, T., Gontijo, S. M., Wells, P. G., Allen, C., "Hyperthermia-mediated drug delivery induces biological effects at the tumor and molecular levels that improve cisplatin efficacy in triple negative breast cancer", *Journal of Controlled Release*, Vol. 282, (2018), 35-45. <https://doi.org/10.1016/j.jconrel.2018.04.029>
- Giannone, G., Santi, M., Ermini, M. L., Cassano, D., Voliani, V., "A cost-effective approach for non-persistent gold nano-architectures production", *Nanomaterials*, Vol. 10, No. 8, (2020), 1600. <https://doi.org/10.3390/nano10081600>
- Kaur, P., Thakur, M., Tondan, D., Bamrah, G. K., Misra, S., Kumar, P., Pandohee, J., Kulshrestha, S., "Nanomaterial conjugated lignocellulosic waste: cost-effective production of sustainable bioenergy using enzymes", *3 Biotech*, Vol. 11, No. 11, (2021), 480. <https://doi.org/10.1007/s13205-021-03002-4>
- Tulinski, M., Jurczyk, M., "Nanomaterials synthesis methods", *Metrology and Standardization of Nanotechnology, Protocols and Industrial Innovations*, (2017), 75-98. <https://doi.org/10.1002/9783527800308.ch4>
- Manivasagan, P., Ashokkumar, S., Manohar, A., Joe, A., Han, H. W., Seo, S. H., Thambi, T., Duong, H. S., Kaushik, N. K., Kim, K. H., Choi, E. H., Jang, E. S., "Biocompatible Calcium Ion-Doped Magnesium Ferrite Nanoparticles as a New Family of Photothermal Therapeutic Materials for Cancer Treatment", *Pharmaceutics*, Vol. 15, No. 5, (2023), 1555. <https://doi.org/10.3390/pharmaceutics15051555>
- Manohar, A., Vijayakanth, V., Vattikuti, S. P., Kim, K. H.,

- “Structural, BET and EPR properties of mixed zinc-manganese spinel ferrites nanoparticles for energy storage applications”, *Ceramics International*, Vol. 49, No. 12, (2023), 19717-19727. <https://doi.org/10.1016/j.ceramint.2023.03.089>
25. Manohar, A., Krishnamoorthi, C. J. M. C., “Low Curie-transition temperature and superparamagnetic nature of Fe₃O₄ nanoparticles prepared by colloidal nanocrystal synthesis”, *Materials Chemistry and Physics*, Vol. 192, (2017), 235-243. <https://doi.org/10.1016/j.matchemphys.2017.01.039>
 26. Manohar, A., Krishnamoorthi, C., “Structural, optical, dielectric and magnetic properties of CaFe₂O₄ nanocrystals prepared by solvothermal reflux method”, *Journal of Alloys and Compounds*, Vol. 722, (2017), 818-827. <https://doi.org/10.1016/j.jallcom.2017.06.145>
 27. Manohar, A., Vijayakanth, V., Vattikuti, S. P., Kim, K. H., “A mini-review on AFe₂O₄ (A= Zn, Mg, Mn, Co, Cu, and Ni) nanoparticles: Photocatalytic, magnetic hyperthermia and cytotoxicity study”, *Materials Chemistry and Physics*, Vol. 286, (2022), 126117. <https://doi.org/10.1016/j.matchemphys.2022.126117>
 28. Manohar, A., Vijayakanth, V., Manivasagan, P., Jang, E. S., Hari, B., Gu, M., Kim, K. H., “Investigation on the physico-chemical properties, hyperthermia and cytotoxicity study of magnesium doped manganese ferrite nanoparticles”, *Materials Chemistry and Physics*, Vol. 287, (2022), 126295. <https://doi.org/10.1016/j.matchemphys.2022.126295>
 29. Sperling, R. A., Parak, W. J., “Surface modification, functionalization and bioconjugation of colloidal inorganic nanoparticles”, *Philosophical Transactions of the Royal Society A: Mathematical, Physical and Engineering Sciences*, Vol. 368, No. 1915, (2010), 1333-1383. <https://doi.org/10.1098/rsta.2009.0273>
 30. Derakhti, S., Safiabad-Tali, S. H., Amoabediny, G., Sheikhpour, M., “Attachment and detachment strategies in microcarrier-based cell culture technology: A comprehensive review”, *Materials Science and Engineering: C*, Vol. 103, (2019), 109782. <https://doi.org/10.1016/j.msec.2019.109782>
 31. Chikawa, J. I., Bandou, M., Tabuchi, K., Tani, K., Saji, H., Takasaki, Y., “Hair growth at a solid-liquid interface as a protein crystal without cell division”, *Progress in Crystal Growth and Characterization of Materials*, Vol. 65, No. 3, (2019), 100452. <https://doi.org/10.1016/j.pcrysgrow.2019.04.002>
 32. Reeves, S. M., Lawal, A., “Characterization and surface impact of paracetamol granules formed by binder dropping”, *Journal of Drug Delivery Science and Technology*, Vol. 61, (2021), 102153. <https://doi.org/10.1016/j.jddst.2020.102153>
 33. Faraji, M., Yamini, Y., Rezaee, M., “Magnetic nanoparticles: synthesis, stabilization, functionalization, characterization, and applications”, *Journal of the Iranian Chemical Society*, Vol. 7, (2010), 1-37. <https://doi.org/10.1007/BF03245856>
 34. Akhtar, S., Slimani, Y., Almessiere, M. A., Baykal, A., Polat, E. G., Caliskan, S., “Influence of Tm and Tb co-substitution on structural and magnetic features of CoFe₂O₄ nanospinel ferrites”, *Nano-Structures & Nano-Objects*, Vol. 33, (2023), 100944. <https://doi.org/10.1016/j.nanoso.2023.100944>
 35. Liandi, A. R., Cahyana, A. H., Kusumah, A. J. F., Lupitasari, A., Alfariza, D. N., Nuraini, R., Sari, R. W., Kusumasari, F. C., “Recent trends of spinel ferrites (MFe₂O₄: Mn, Co, Ni, Cu, Zn) applications as an environmentally friendly catalyst in multicomponent reactions: A review”, *Case Studies in Chemical and Environmental Engineering*, (2023), 100303. <https://doi.org/10.1016/j.csee.2023.100303>
 36. Du, W., Zheng, Y., Liu, X., Cheng, J., Reddy, R. C. K., Zeb, A., Lin, X., Luo, Y., “Oxygen-enriched vacancy spinel MFe₂O₄/carbon (M= Ni, Mn, Co) derived from metal-organic frameworks toward boosting lithium storage”, *Chemical Engineering Journal*, Vol. 451, (2023), 138626. <https://doi.org/10.1016/j.cej.2022.138626>
 37. Salokhe, A., Koli, A., Jadhav, V., Mane-Gavade, S., Supale, A., Dhabbe, R., Yu, X.-Y., Sabale, S., “Magneto-structural and induction heating properties of MFe₂O₄ (M= Co, Mn, Zn) MNPs for magnetic particle hyperthermia application”, *SN Applied Sciences*, Vol. 2, No. 12, (2020), 2017. <https://doi.org/10.1007/s42452-020-03865-x>
 38. Manthiram, A., Fu, Y., Chung, S. H., Zu, C., Su, Y. S., “Rechargeable lithium-sulfur batteries”, *Chemical Reviews*, Vol. 114, No. 23, (2014), 11751-11787. <https://doi.org/10.1021/cr500062v>
 39. Manohar, A., Vijayakanth, V., Vattikuti, S. P., Kim, K. H., “Electrochemical investigation on nickel-doped spinel magnesium ferrite nanoparticles for supercapacitor applications”, *Materials Chemistry and Physics*, Vol. 301, (2023), 127601. <https://doi.org/10.1016/j.matchemphys.2023.127601>
 40. Manohar, A., Vijayakanth, V., Vattikuti, S. P., Kim, K. H., “Electrochemical energy storage and photoelectrochemical performance of Ni_{1-x}Zn_xFe₂O₄ nanoparticles”, *Materials Science in Semiconductor Processing*, Vol. 157, (2023), 107338. <https://doi.org/10.1016/j.mssp.2023.107338>
 41. Sartori, K., Cotin, G., Bouillet, C., Halté, V., Bégin-Colin, S., Choueikani, F., Pichon, B. P., “Strong interfacial coupling through exchange interactions in soft/hard core-shell nanoparticles as a function of cationic distribution”, *Nanoscale*, Vol. 11, No. 27, (2019), 12946-12958. <https://doi.org/10.1039/C9NR02323B>
 42. Wang, C., Peng, S., Lacroix, L. M., Sun, S., “Synthesis of high magnetic moment CoFe nanoparticles via interfacial diffusion in core/shell structured Co/Fe nanoparticles”, *Nano Research*, Vol. 2, (2009), 380-385. <https://doi.org/10.1007/s12274-009-9037-4>
 43. Lee, K., Lee, S., Ahn, B., “Understanding high anisotropic magnetism by ultrathin shell layer formation for magnetically hard-soft core-shell nanostructures”, *Chemistry of Materials*, Vol. 31, No. 3, (2019), 728-736. <https://doi.org/10.1021/acs.chemmater.8b03591>
 44. Smith, M., McKeague, M., DeRosa, M. C., “Synthesis, transfer, and characterization of core-shell gold-coated magnetic nanoparticles”, *MethodsX*, Vol. 6, (2019), 333-354. <https://doi.org/10.1016/j.mex.2019.02.006>
 45. Tatarchuk, T., Shyichuk, A., Sojka, Z., Gryboś, J., Naushad, M., Kotsyubynsky, V., Kowalska, M., Kwiatkowska-Marks, S., Danyliuk, N., “Green synthesis, structure, cations distribution and bonding characteristics of superparamagnetic cobalt-zinc ferrites nanoparticles for Pb (II) adsorption and magnetic hyperthermia applications”, *Journal of Molecular Liquids*, Vol. 328, (2021), 115375. <https://doi.org/10.1016/j.molliq.2021.115375>
 46. Ferjaoui, Z., Jamal Al Dine, E., Kulmukhamedova, A., Bezdetnaya, L., Soon Chang, C., Schneider, R., Mutelet, F., Mertz, D., Bégin-Colin, S., Quilès, F., “Doxorubicin-loaded thermoresponsive superparamagnetic nanocarriers for controlled drug delivery and magnetic hyperthermia applications”, *ACS Applied Materials & Interfaces*, Vol. 11, No. 34, (2019), 30610-30620. <https://doi.org/10.1021/acsami.9b10444>
 47. Hufschmid, R., Arami, H., Ferguson, R. M., Gonzales, M., Teeman, E., Brush, L. N., Browning, N. D., Krishnan, K. M., “Synthesis of phase-pure and monodisperse iron oxide nanoparticles by thermal decomposition”, *Nanoscale*, Vol. 7, No. 25, (2015), 11142-11154. <https://doi.org/10.1039/C5NR01651G>
 48. Phadatare, M. R., Meshram, J. V., Gurav, K. V., Kim, J. H., Pawar, S. H., “Enhancement of specific absorption rate by exchange coupling of the core-shell structure of magnetic nanoparticles for magnetic hyperthermia”, *Journal of Physics D: Applied Physics*, Vol. 49, No. 9, (2016), 095004. <https://doi.org/10.1088/0022-3727/49/9/095004>
 49. Permien, S., Indris, S., Schürmann, U., Kienle, L., Zander, S., Doyle, S., Bensch, W., “What happens structurally and electronically during the Li conversion reaction of CoFe₂O₄ nanoparticles: an operando XAS and XRD investigation”,

- Chemistry of Materials*, Vol. 28, No. 2, (2016), 434-444. <https://doi.org/10.1021/acs.chemmater.5b01754>
50. Bhosale, A. B., Somvanshi, S. B., Murumkar, V. D., Jadhav, K. M., "Influential incorporation of RE metal ion (Dy^{3+}) in yttrium iron garnet (YIG) nanoparticles: Magnetic, electrical and dielectric behaviour", *Ceramics International*, Vol. 46, No. 10, (2020), 15372-15378. <https://doi.org/10.1016/j.ceramint.2020.03.081>
51. Somvanshi, S. B., Jadhav, S. A., Khedkar, M. V., Kharat, P. B., More, S. D., Jadhav, K. M., "Structural, thermal, spectral, optical and surface analysis of rare earth metal ion (Gd^{3+}) doped mixed Zn-Mg nano-spinel ferrites", *Ceramics International*, Vol. 46, No. 9, (2020), 13170-13179. <https://doi.org/10.1016/j.ceramint.2020.02.091>
52. Bharati, V. A., Somvanshi, S. B., Humbe, A. V., Murumkar, V. D., Sondur, V. V., Jadhav, K. M., "Influence of trivalent Al-Cr co-substitution on the structural, morphological and Mössbauer properties of nickel ferrite nanoparticles", *Journal of Alloys and Compounds*, Vol. 821, (2020), 153501. <https://doi.org/10.1016/j.jallcom.2019.153501>
53. Manohar, A., Krishnamoorthi, C., "Photocatalytic study and superparamagnetic nature of Zn-doped $MgFe_2O_4$ colloidal size nanocrystals prepared by solvothermal reflux method", *Journal of Photochemistry and Photobiology B: Biology*, Vol. 173, (2017), 456-465. <https://doi.org/10.1016/j.jphotobiol.2017.06.025>
54. Manohar, A., Vijayakanth, V., Vattikuti, S. P., Kim, K. H., "Synthesis and characterization of Mg^{2+} substituted $MnFe_2O_4$ nanoparticles for supercapacitor applications", *Ceramics International*, Vol. 48, No. 20, (2022), 30695-30703. <https://doi.org/10.1016/j.ceramint.2022.07.018>
55. Salati, A., Ramazani, A., Kashi, M. A., "Tuning hyperthermia properties of FeNiCo ternary alloy nanoparticles by morphological and magnetic characteristics", *Journal of Magnetism and Magnetic Materials*, Vol. 498, (2020), 166172. <https://doi.org/10.1016/j.jmmm.2019.166172>
56. Kötz, R., Weitschies, W., Trahms, L., Semmler, W., "Investigation of Brownian and Néel relaxation in magnetic fluids", *Journal of Magnetism and Magnetic Materials*, Vol. 201, No. 1-3, (1999), 102-104. [https://doi.org/10.1016/S0304-8853\(99\)00065-7](https://doi.org/10.1016/S0304-8853(99)00065-7)
57. Paul, P. S., "Design and Implementation of an Alternating Current Susceptometer for Measuring Brownian Relaxation Time of Magnetic Nanoparticles Suspended in a Liquid Medium", (2017). https://ir.library.oregonstate.edu/concern/graduate_projects/rr172296x

AIMS AND SCOPE

Advanced Ceramics Progress (ACERP) as an ISC international journal is devoted to elucidating the fundamental aspects of chemistry and physics occurring at a wide range of oxide and nonoxide ceramics and composite materials and their processing, microstructure, properties, and applications. The journal provides a unique venue for publishing new exciting research, focusing on dynamic growth areas in this field.

INSTRUCTIONS FOR AUTHORS

Submission of manuscript represents that it has neither been published nor submitted for publication elsewhere and is result of research carried out by author(s).

Authors are required to include a list describing all the symbols and abbreviations in the manuscript. Use of the international system of measurement units is mandatory.

- On-line submission of manuscripts results in faster publication process and is recommended. Instructions are given in the ACERP web site: www.acerp.ir
- References should be numbered in brackets and appear in sequence through the text. List of references should be given at the end of the manuscript.
- Figures' captions are to be indicated under the illustrations. They should sufficiently explain the figures.
- Illustrations should appear in their appropriate places in the text.
- Tables and diagrams should be submitted in a form suitable for reproduction.
- Photographs and figures should be of high quality saved as jpg files (resolution > 600 dpi).
- Tables, illustrations, figures and diagrams will be normally printed in single column width (8 cm). Exceptionally large ones may be printed across two columns (17 cm).

PAGE CHARGES AND REPRINTS

ACERP subscribers do not need to make any payment for publication and reprints.

AUTHORS CHECKLIST

- Author(s), bio-data including academic degree, affiliation(s), ORCID(s), and e-mail addresses.
- Manuscript including title, abstract, key words, illustrations, tables with tables' captions, figures with figures' captions, acknowledgement, and list of references.
- MS Word files of the manuscript in the ACERP template and all figures (resolution > 600 dpi).
- Similarity check of the manuscript, copyright forms, and conflict of interest forms

Advanced Ceramics Progress,
P.O. Box 31787-316, Meshkin Dasht, Alborz, I. R. Iran
Materials and Energy Research Center, Imam Khomeini Blvd, Meshkin Dasht, Alborz, I. R. of Iran
P.O. Box 14155-4777, Tehran, I. R. Iran
No. 5, Ahuramazda St., Alvand Ave., Argentine Sq., Tehran, I. R. of Iran

Advanced Ceramics Progress

Volume 9, Number 2, Spring 2023

CONTENTS

Ali Shanaghi Ali Reza Souri Wrya Forghani	Comparative Study of Anodized Titanium Surfaces: The Effect of Low Voltage on the Morphology, Performance, and Corrosion Resistance of the Double Layer	1-7
Mohammad Reza Akbarpour Solmaz Moniri Javadhesari	Characterization of Flowability and Compaction Behavior of Biomedical Ti-Cu Intermetallic Alloy Synthesized by Mechanical Alloying Method	8-15
Leila Rezazadeh Susan Hasheminia Zahra Khakpour	The Effect of Temperature and Al as an Additive on the Synthesis, Structure, Densification, and Conductivity of Garnet-Type $\text{Li}_7\text{La}_3\text{Zr}_2\text{O}_{12}$	16-23
Sana Seifollahpour Afshin Ashofteh Amir Hossein Shahdadi Mahmoud Mosavi Mashhadi	Nanoindentation-Based Mechanical Properties Evaluation of Nano-Structure and Composite Plasma Spray Formed Ceramic Nozzles	24-35
Kaveh Kolahgar Azari Amir Hossein Sayadi Kelemi Ali Alizadeh Hamid Omidvar	Investigating the Phenomenon of Flutter as well as the Mechanical and Microstructural Properties of Layered Composite of Aluminum Sheet with An Epoxy Matrix Reinforced with Carbon Fibers	36-44
Kamran Heydaryan Mohammad Almasi Kashi	Characterization and magnetic properties of CoFe_2O_4 nanoparticles synthesized under gas atmosphere: Effect of ferrofluid concentration on hyperthermia properties	45-52



Journal Home Page: www.acerp.ir